QATAR UNIVERSITY

COLLEGE OF ENGINEERING

SEMI-ACTIVE VIBRATION ISOLATOR USING MAGNETORHEOLOGICAL

ELASTOMER (MRE)

BY

THAER MAHMOUD IBRAHIM SYAM

A Thesis Submitted to

the College of Engineering

in Partial Fulfillment of the Requirements for the Degree of

Masters of Science in Mechanical Engineering

June 2020

COMMITTEE PAGE

The members of the Committee approve the Thesis of
Thaer Mahmoud Ibrahim Syam defended on 07/05/2020.

_____

Dr. Asan Gani Bin Abdul Muthalif
Thesis Supervisor

_____

Dr. Rahizar Ramli
Committee Member

_____

Dr. Mohammad Roshun Paurobally
Committee Member

_____

Dr. Jamil Renno
Committee Member

Approved:

_____

Khalid Kamal Naji, Dean, College of Engineering

ABSTRACT

SYAM, THAER, M., Masters: June: 2020, Masters of Science in Mechanical Engineering

Title: Semi-Active Vibration Isolator Using Magnetorheological Elastomer (MRE)

Supervisor of Thesis: Asan, G. A., Muthalif.

Smart materials are materials by which their properties are able to be altered due to external stimuli such as temperature, pressure and magnetic field. Magnetorheological Elastomer (MRE) is a type of smart composite material consisting of a polymer matrix embedded with ferromagnetic particles. In the presence of an external magnetic field, its mechanical properties such as stiffness change due to the interaction between the magnetic particles. It has been used in many applications such as vibration dampers and isolators. Unwanted vibration in machines can cause severe damage and machine breakdown. Vibration in rotary machines can cause severe damage and machine breakdown. Vibration isolation has been in interest of many researchers for many decades. In this work, semi-active vibration isolator using MRE is proposed for a potential used in drilling system in order to isolate the torsional vibration.

This research focuses on studying MRE computationally and experimentally. Analytical simulation study was done by utilizing different MRE models from the literature on a base motion isolation (base excitation) system as a preliminary study in order to understand the characteristics of MRE. Results showed that as the magnetic field increases, the stiffness of MRE increases by a shifting in the natural frequency of the system from the transmissibility curve, so that vibration is reduced. In addition, a numerical modeling of MRE using COMSOL Multiphysics software was done to

study the effect of the magnetic field on its stiffness in axial and torsional modes. The MRE consisted of a cylindrical silicon rubber embedded with 12 iron particles. An increase of 28.75% and 20.12% of the stiffness was obtained in axial and torsional modes, respectively. The transmissibility analysis revealed that as the magnetic field increases, the linear and torsional stiffness increases as well which cause a shifting in the transmissibility curves to the right indicating that the natural frequency of the system is increased.

Furthermore, MRE was fabricated with a 35% volume fraction (VF) consisted of a silicon rubber and iron particles. MRE was used in torsional vibration isolation on the proposed drilling system. It was fitted with a coupler and attached on the shaft (drill string) in order to study its efficiency in vibration isolation under a magnetic field. Two tests were conducted on the drilling application used in this research, the first test was a hammer impact test by which the system was excited by an input and the response was obtained. The torsional transfer function (TTF) analysis showed that the natural frequency of the system has shifted from 13.9 Hz to 17.5 Hz by the influence of the magnetic field around the MRE. Finally in this work, another test was done during the continuous rotation of the drilling prototype; results showed that the amplitude of rotation is attenuated by the presence of the magnetic field.

ACKNOWLEDGMENTS

TABLE OF CONTENTS

LIST OF TABLES

LIST OF FIGURES

Chapter 1: Introduction

In this chapter, an introduction and justifications are given about the selected thesis topic, starting from introducing the magnetorheological elastomers (MRE) and its applications. In addition, different methods in vibration isolation are discussed and vibration in drilling process which the proposed system to test. Then, the problem statement and its significance are given. Finally, the research aim and objectives are mentioned and the chapter ends with the thesis content.

1.1 Smart Materials

Smart materials are materials that respond to external stimuli such as temperature, stress, moisture and magnetic field. They can be called responsive materials. The exposure of these materials to the external stimuli can cause changes in their properties. Hence, they have been on the market for many years and they are used in many end-use applications such as construction, medical, transportation and vibrations [1]. There are different types of smart materials which can be used in different applications such as [1]:-

- Piezoelectric materials: materials which produce a voltage when applies a mechanical stress to these materials.

- Shape memory alloy: are metal alloys that once strained, revert back to their original shape upon an increase in temperature above a critical transformation temperature.

- pH sensitive polymers: are materials which will respond to the changes in the pH of the surrounding medium by varying their dimensions.

- Magnetostrictive materials: are type of smart materials which are able to alter their properties by an external magnetic field.

1.2 Magnetorheological Elastomer (MRE)

Magnetostrictive materials are type of smart materials which are able to alter their properties by an external magnetic field. Magneto-rheological elastomer (MRE) is a type of smart composite material that consists of a non-magnetizable polymer matrix embedded with micro/nano-sized ferromagnetic particles. These materials are able to alter their mechanical properties such as elasticity and stiffness by the exposure of an external magnetic field [2,3]. This property makes them attractive to many engineering applications such as dampers, tuning dampers, sensors, and magneto-rheological elastic polishing bodies [4-7]. The polymer matrix is mixed with the magnetic particles and then it is vulcanized at a high temperature where the particles can move inside the polymer matrix; called curing, this curing can be with or without the magnetic field. During curing process, anisotropic MREs are materials where the magnetic particles are arranged uniformly after applying the magnetic field during curing process. On the other hand, isotropic MREs contain these particles in a random distribution when no magnetic field is applied. Figure 1 shows the curing process of MREs [8].
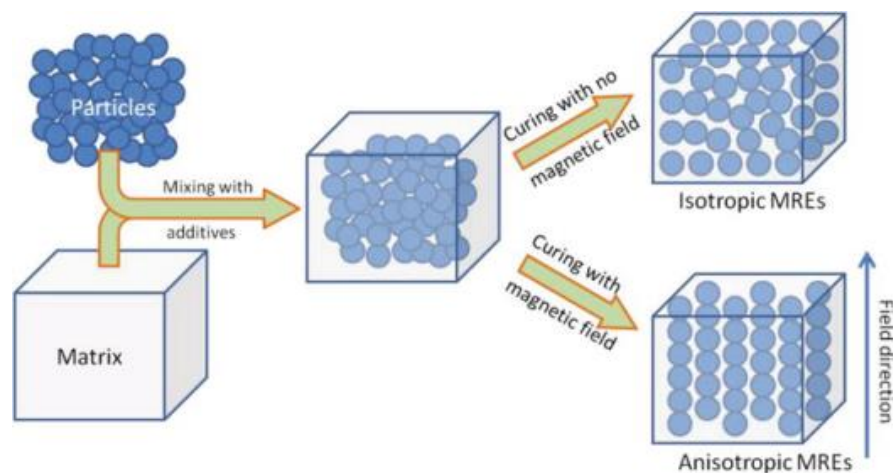
Figure 1. Preparation of MRE [8].

The internal magnetic particles which form like a chain in the direction of the magnetic field are the main factor in determining the mechanical properties of these elastomers [9]. The better arrangement of particles by controlling the magnetic field, the better mechanical properties obtained of MRE [10]. For the polymer elastic matrix, there are lots of polymeric rubbers such as natural rubber, silicone rubber, and poly dimethylsiloxane (PDMS) [11-13]. In addition, the magnetic particles are mostly made up of carbonyl iron powder invented by BASF [14].

1.3 Vibration Isolation

Vibration phenomenon can be simply defined as repetitive motions or oscillations that happen when the structure is displaced from its origin or equilibrium position. Vibration is found in any machining process and in everywhere in the daily life. When the phone rings, the mobile phone vibrates, when the Air Conditioning is on, it vibrates. Therefore, this phenomenon is very important to be studied. Vibrations can be desired in some purposes such as violin and guitar in the musical tools and instruments. In addition, it can be desired in some machining devices to serve functional purposes such as compactors, sieves and hoppers. However, vibration is undesired in most of the cases as it's the cause of noise, damage and many other inconveniences. Therefore, if this vibration is not controlled or isolated, it could lead to machinery breakdown and structural failure. In vibration, the amplitude and frequency of any dynamic system can be affected by two major aspects; the internal dynamics of the system and the external excitation force. In general, vibration isolation can be categorized into three main types as shown in Figure 2.
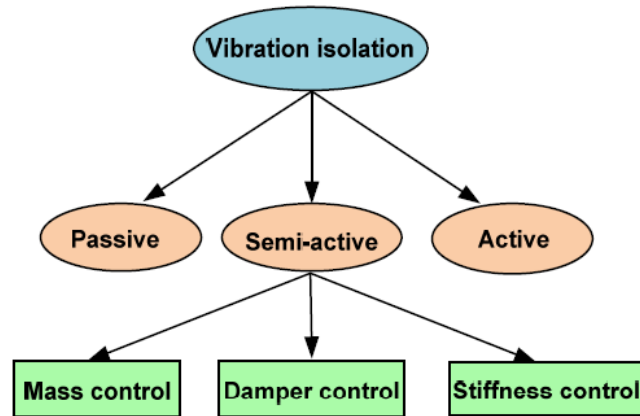
Figure 2. Overview of vibration isolation approaches [15].

Vibration can be isolated in three different methods; passive, semi-active and active. Passive vibration isolation happens initially during the design phase and it a simple method. This method uses passive mechanical components and structures such as springs and rubber pads and dampers. This type of vibration isolation does not require any external power supply or a hardware device. The adaptation of this ystem is not possible once implemented. On the other hand, active vibration isolations requires a power supply, it is methodology works as a feedback system which consists of a controller, actuator and a sensor. This system is adaptable and it has better performance in controlling vibration. One issue with active vibration isolation method is that system can destabilize due to the energy which can be added. Finally, the semi-active vibration isolation which combines the advantages and best features of both passive and active vibration isolation approaches, it offers the reliability of passive isolation and the versatility of active isolation. In addition, it consumes less power than active isolation and it can be controlled unlike the passive isolation. The mass, stiffness and damping can be variables in the semi-active vibration isolation. The mass is unable to change in a short period of time as its imparctical. Therefore, variable stiffness and variable damping is to be considered. Utilizing MRE in

vibration isolation is a type of semi-active vibration isolation methods due to its ability to change its stiffness when exposed to an external magnetic field. This will be further explained in the next chapter.

1.4 Vibrations in Drilling Process and the Proposed System

In this research, the semi-active vibration isolation utilizing MRE is proposed to be used on a drilling process prototype. Drilling which can be simply defined as a cutting process that utilizes a drill bit to make a circular hole in solid materials. Drilling process is used to serve in variety of tasks other than boring holes in the solid structures, such as spot facing, counter sinking, tapping and reaming. Most of the time, the drill bit is a rotary cutting tool which is placed and pressed against the work-piece and it rotates at very high revolutions per minute. This will force the drill bit to act as a cutting edge on the work-piece which will cut off and remove the material (chips) from the hole as it is drilled. This can be explained in Figure 3.
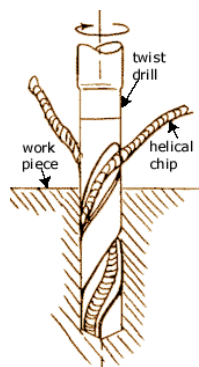
Figure 3. Drilling process [16].

In some applications, the drill string is required to be long, such as boring holes in the earth's crust to extract natural resources such as water, natural gas and minerals. Such long structures are prone to be subjected to massive and severe vibrations. Therefore, the complexity of the dynamic behavior of drill strings is significant. Hence, this vibration needs to be controlled and isolated to avoid

undesired machine damage or failure. During drilling process and due to cutting

forces, the drill string is subjected to three main modes of vibrations; longitudinal,

torsional and lateral as shown in Figure 4. The overall performance of the drill string

is affected by these modes of vibration.
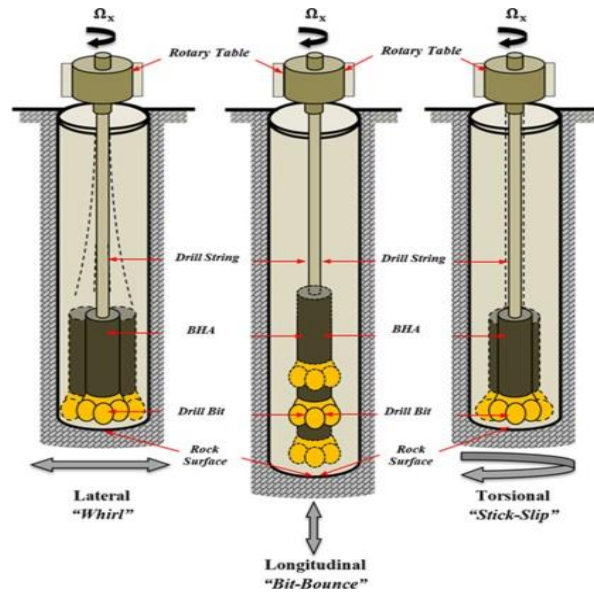
Figure 4. Modes of vibration during drilling process [17].

Each of the three modes of vibration can be risky and has its own destructive

nature. In longitudinal mode the vibration motion is parallel to its axis. "Bit-Bounce"

is the phenomena that cause this mode; this creates instability during drilling which

affects the contact of the drill bit with the work-piece. This can cause damage to the

drill bit cutting structures such as seals and bearings [18]. Secondly, torsional mode is

associated with phenomena called "stick-slip" which causes irregularities during

rotation. This can cause severe damages such as bit wear, fatigue, shock loading, and

lead to equipment failure. Lastly, lateral mode of vibration is side-to-side motion

which causes bending in the drill string. The eccentric rotation of the drill string

around an axis other than its geometrical center is called "whirl". This mode of

vibration is very severe and it leads to the failure of the drill string due to the excessive stresses. However, since the drilling process usually to make holes, it requires the drill bit to rotate and a longitudinal load to force the drill bit to penetrate the work-piece, and since the vibration in rotary machines in general are undesired, this study is interested in the torsional vibration mode isolation. The proposed system that will be used is a test rig designed and manufactured representing a drilling process.

1.5 Problem Statement and its Significance

Vibration isolation utilizing MRE has been studied in decades for several applications. However, the vibration which is produced during the working of rotary machines such as shafts and gears can severely cause structural failures or breakdowns. Since there are enormous developments happening in various sectors world widely such as Oil & Gas, industrial, buildings, power, rail transport and Infrastructure. These projects require sophisticated technologies. Oil & Gas industry is the main source of energy and economy in the GCC countries. The extraction of natural gas from underground requires very advanced drilling machines and operations onshore and offshore. Therefore, there is a massive need to perform research in the vibration isolation for such process. This can achieve by developing a semi-active vibration isolator using MRE. This is to be applied on a drilling test rig which can lead to a significant enhancement in such technology such as better life time of machines. In addition, the usage of smart materials such as MRE in vibration isolation can improve the economy in the energy sector by improving the efficiency of machines. Hence, different studies on MRE including analytical and numerical analyses are necessary in order to understand its characteristics and the potential application of such technology on vibration isolation on a drilling system.

1.6 Research Objectives

The aim of this research is to study the behavior and characteristics of the MRE and to investigate its efficiency in torsional vibration isolation on a drilling process application. This can be achieved by the following objectives:-

- To study different mathematical and analytical models for MRE semi-active vibration isolator using MATLAB.

- To perform a numerical simulation of the MRE using a finite element analysis FEA Multi-physics software.

- To design an experimental setup and to investigate the efficiency of MRE semi-active torsional vibration isolator for drilling application.

1.7 Research Methodology

Firstly, enough knowledge of the subject must be achieved and one of the main tasks of identifying a problem is the literature review. Reporting and summarizing other researches in this area will explore the knowledge and will give a chance for improvements. It was done by collecting all related research articles/papers and summary a literature review. Secondly, an analytical study was done on MRE by modeling different MRE models which were found in the literature on a base motion isolation system (base excitation) similar to the proposed drilling experimental setup. This was done by expressing these models mathematically. Then, by using MATLAB (Simulink), these MRE models were simulated as the input damping force on the base excitation system by creating block diagrams on SIMULINK environment that can show the behavior of MRE in isolating vibration at different magnetic fields. This analysis was done in order to compare between different MRE models which were proposed previously. In addition, to simulate and study the mechanical properties of these MRE models such stiffness and damping under a magnetic field. After that, the

Finite Element Analysis (FEA) was done using COMSOL multi-physics software by which MRE was modeled and some studies were done to obtain the characteristics of MRE in vibration isolation in linear and torsional modes. The two mentioned studies were done in order to understand the characteristics and behavior of MRE and to investigate its properties such as damping and stiffness. After the previous two analyses, a prototype for the drilling process was developed and a fabrication of MRE was made. Finally, the performance and efficiency of the MRE on a rotary shaft as in drilling system was tested and analyzed. Figure 5 shows the research flowchart.
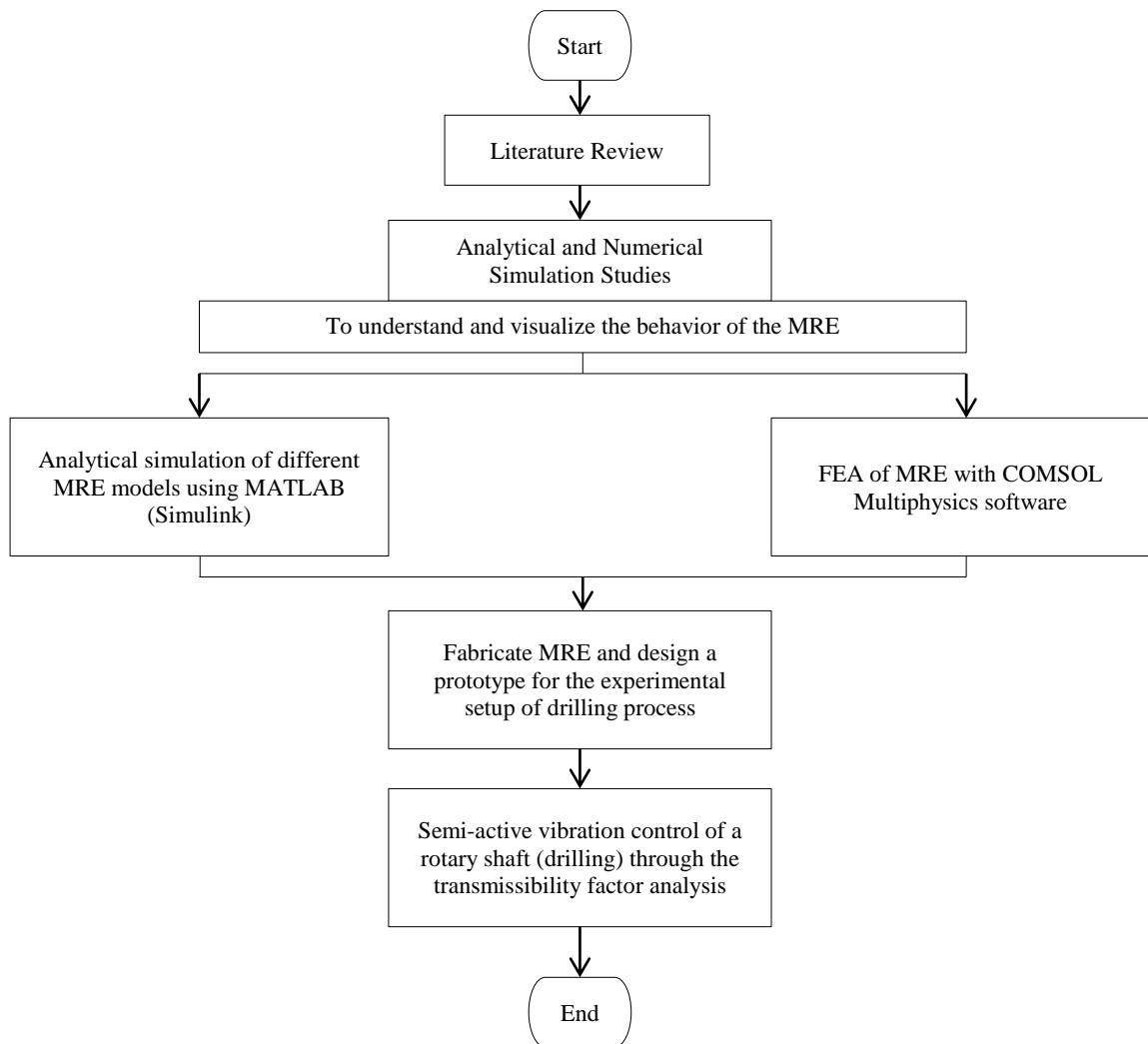
Figure 5. Research methodology flowchart.

1.8 Organization of the Thesis

Chapter 1: Introduction: This chapter introduces the research overview as it reviews MRE, vibration isolation and vibration in drilling process. It also includes the problem statement and its significance, research objectives, research methodology, as well as outlining the organization of the thesis.

Chapter 2: Literature review: This chapter reviews MRE properties and characteristics as well as its applications in vibration isolation. In addition, different mathematical models of MRE are reviewed. It reviews different FEA simulations that studied MRE and analyzed its behavior. Lastly, it includes different strategies used in vibration isolation during drilling process since it's the proposed application where MRE is used in this research.

Chapter 3: Analytical and numerical simulation studies on MRE: This chapter shows different simulation studies about different models of MRE which was developed previously. It starts with analytical simulation of these models of MRE using MATLAB (Simulink) software for mass spring damper base excitation system and compares them. Secondly, a FEA simulation of MRE to analyze its properties under external magnetic field is shown in this chapter.

Chapter 4: Experimental Developments and Prototype Setup to Test MRE and Experimental Results: This chapter is about fabricating and curing MRE samples. After that, it will explain a proposed application where MRE can be used on to study its efficiency. It will show a test rig for drilling process in order to study the behavior of MRE in semi-active vibration isolation. It will also include two tests in order study the efficiency of MRE on the proposed drilling application.

Chapter 5: Conclusions and future works: It will summarize the main findings and conclusions in this thesis and will highlight some recommendation for future works.

Chapter 2: Literature Review

This chapter will further review basic concepts introduced in the 1st chapter. It includes different MRE mathematical models. Also, a review of articles that expressed MRE numerically using the finite element analysis (FEA) will be shown. Lastly, applications of vibration isolation using MRE, and vibration isolation in drilling process as proposed in this research, as well as other systems. The relevant literatures reported in these areas are reviewed to build the knowledge regarding MRE, semi active vibration isolation in mechanical vibration and drilling process system.

2.1 Mechanical Vibration

In general, mechanical vibration occurs when a particle or a body of certain mechanical system displaced from a position of equilibrium. Actually, this motion is in form of oscillations which result from the input excitation to the system. A system can undergo free vibration when it oscillates without applying any external forces. Mechanical system can be classified as undamped system when there is no energy dissipative element during the motion so that the amplitude of oscillation remains constant with time. However; in real life the amplitude of vibration decreases with time because every system has its own damping besides surrounding medium damping such as air so that the mechanical system become damped system [19]. Most of vibrations are not preferred in machines and mechanical system since they introduce some undesirable stresses, wear, energy losses and fatigue therefore, the target of all vibration control system is to either eliminate or reduce the undesirable effects of vibration.

2.1.1 Mechanical vibration control and transmissibility factor

As briefly introduced in Section 1.3 gaining control over a system with

vibration is a necessity for better accuracy, quieter operations, and comfort level and in some situations; it is cheaper than replacing an older system with the newer one. Vibration isolation over a system is accomplished by one of the following elements, passive, active and semi-active vibration isolation. However, sometimes a combination of these systems can be used. All of these approaches are shown in Figure 6.

(a)	(b)	(c)
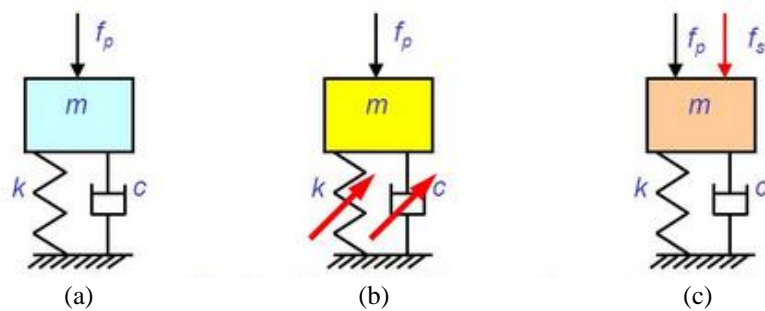
Figure 6. Different vibration isolation approaches [20]; (a) passive, (b) semi-active and (c) active.

Where f_p is the primary force, and f_s is the secondary force. The passive vibration isolation system as shown in Figure 6 (a) consists of one or more devices attached or embedded in a structure. Passive vibration isolation is widely used in industry due to it simple design, low cost, and ease of manufacturing. It can be designed for a system's durability. If more or less stiffness is required it can be as simple as changing the type of material being used or changing the size of the elements [21]. However, passive mounts are rarely able to attenuate all of the input vibrations in a system [22]. The active control system control actuators that apply forces to the structure in a prescribed manner and has a large external power source and the range of force is wider and can achieve better performance as in Figure 6 (c). The drawback of this kind of system is that its high cost, high power consumption

[22,23]. Semi-active vibration isolation which shown in Figure 6 (b) is a type of active vibration isolation systems by which the external energy demanding are lower than the active isolation system. Semi-active devices cannot remove or add energy to the system's structure [24]. However, Semi-active devices can control real time parameters such as spring stiffness, k and coefficient of damping, c [24]. Thus change can assist in reducing the vibration. The controllable change of state has desirable features such as fast response time. Semi-active devices can utilize the motion of the structure to improve the forces for control, so it is more stable. The advantages of this system are it has low costs for initiation, small amount of power consumption, can be controlled easily, easy to install and it's simple. The disadvantages are the limited force range and the efficiency is not as well as active systems.
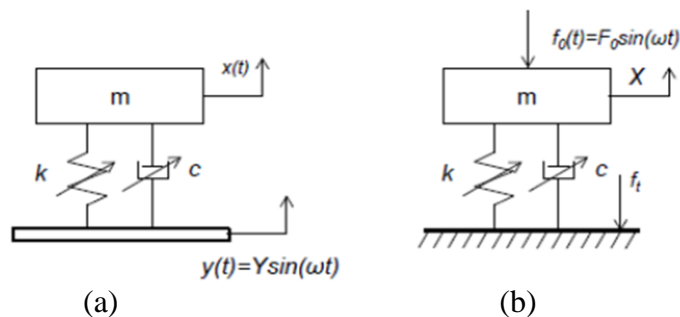
Figure 7. Principles of vibration isolation systems [27]: (a) base motion isolation and (b) force isolation.

The main goal in vibration control is to eliminate and reduce the vibrations in mechanical systems which also mean that vibration should be isolated from the systems. Basically, there are two types of isolation in each system force isolation (transmissibility) and motion isolation (transmissibility) which can be identified from system with either rotational or linear motion [25]. This is shown in Figure 7. Vibration forces can be directly transmitted to the system of interest from input source so that if the system is isolated by means of flexible and dissipative elements such as

13

springs and dampers the unwanted forces are filtered out. However, vibration motions that applied to moving parts of mechanical system can be also absorbed through isolators [26].

Motion transmissibility is the ratio of amplitude response to the system's part motion whereas the force transmissibility is the ratio of the maximum force transmitted to the system, F_t, due to spring and damper reactions to the spring force, F, at the same excitation frequency range, f, [28] as shown in the figure below:-
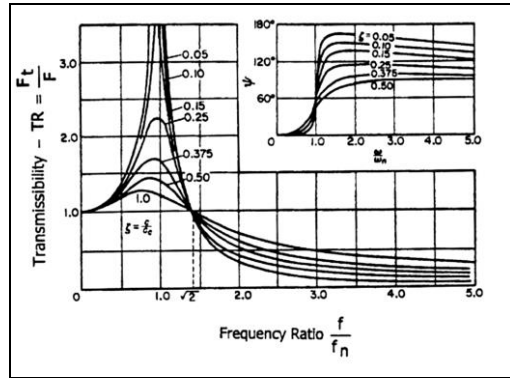
Figure 8. Transmissibility graph [26].

Both motion and force transmissibility is function of frequency ratio denoted by $r = f/f_n$ or $r = \omega/\omega_n$ and damping ratio $\zeta = c/c_c$, where $\omega = 2\pi f$ (rad/s) f_n is the system natural frequency (Hz), f is the frequency of oscillation (Hz), c is the damping coefficient (Ns/m) and c_c is the critical damping coefficient (Ns/m).

The transmissibility factor should be below 1 in order to achieve efficient vibration isolation; this means that the force or motion loads transmitted is less than the input load. The desired regime to be achieved for significant vibration isolation is reduction zone ($r = \omega/\omega_n \gg \sqrt{2}$) [29]. The zone which is less than the frequency ratio is called the amplification zone where the vibration reduction is inefficient. The vibration isolator using MRE must be optimized and adjusted to enhance the

properties of vibration reduction system and for it for different excitation frequencies.

2.2 Magnetorheological Materials

Magneto-rheological phenomenon was discovered in 1948 by Jacob Rainbow [30]. Magneto rheological materials belong to a class of smart materials can be gel, fluid or even a solid material such as rubber or elastomer. It mainly deals with application of magnetic field and the changes that it causes the viscosity/elasticity of the material along with effect in particles orientation [31]. They are used in various applications such transportation, medical, and dampers [32].

2.2.1 Magnetorheological fluids (MRF)

Magneto rheological fluid damper is a kind of smart material which mainly consists of small size ferromagnetic particles suspended in a matrix of some kind of viscous fluid such as silicon and mineral oil. Before applying magnetic field these particles are randomly scattered among the fluid and once applying it particles are arranged in chains therefore this will change the viscosity and the shear properties of MRF [33]. It is used in so many applications such as controlled damper, brake and clutch besides vibration absorber for mechanical structure. There are some limitations of using MRF which represent actually in ferromagnetic particles which settle down in respect with the absence of magnetic field so that each time after using MRF there is a need for container to keep these particles frequently [34].

2.2.2 Magnetorheological elastomers (MRE)

As introduced in Chapter 1, MRE is a class of composite materials by which the ferromagnetic particles are embedded in a polymer matrix. In the presence of a magnetic field, the magnetizable particles are arranged like a chain towards the direction of the field similar to MRF as indicated in Figure 9. In the absence of the magnetic field, the particles are returned back to its original orientation. Therefore,

varying the magnetic field will affect the stiffness properties of the composite [35].
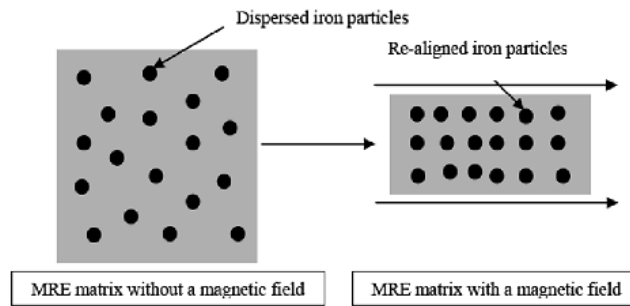
Figure 9. Schematic diagram of MRE [36].

Unlike MRF, MRE overcomes the problem associated with particles which settle down when there is no any applied magnetic field since these particles are fitted into a form of solid rubber matrix [32,33]. Some of MRF applications are same with those of MRE especially in noise and vibration control, but MRF is mostly used in automotive bushings and engine mounts [35]. Both are complementary since magnetic field controls the shear modulus of MRE while it controls the yield strength of MRF [35]. Figure 10 shows the Scanning Electron Micrograph (SEM) of the ferromagnetic particles in a silicon polymer matrix. Figure 10 (a) shows the randomly distributed particles in the absence of a magnetic field. Whereas Figure 10 (b) shows how the particles are arranged like chains in the presence of the magnetic field.

(a)   (b)
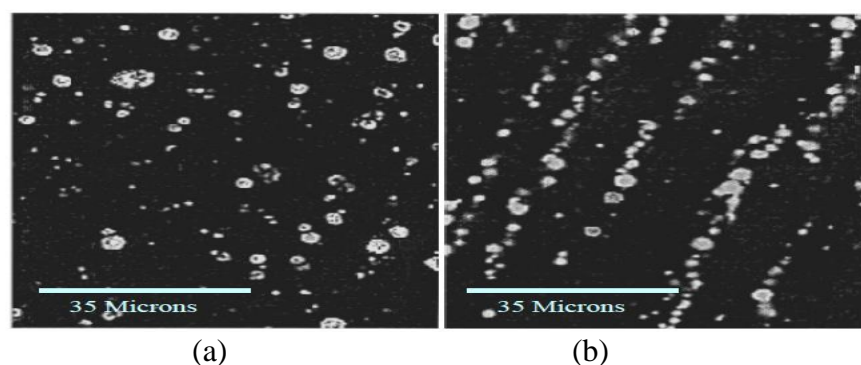
Figure 10. SEM images of particles in an elastomer; (a) randomly dispersed particles, (b) particles aligned by applied magnetic field [37].

2.2.2.1 Properties and characteristics of MRE

As the magnetic field is applied, the rheological and mechanical properties of MRE containing the ferromagnetic particles are changed; this phenomenon is called the magneto rheological (MR) effect. Basically, MRE field dependence properties are caused by the field-induced internal dipole magnetic forces between the magnetic particles. Hence, the mechanical behavior of MRE depends on both matrix properties and the formulation of the particles inside the polymer.

In fact, the effects of magnetic field mainly contribute in changing only the overall MRE stiffness. However, the change in the damping characteristics of MRE has not been approved by most researches yet, except few in which they found that as lower frequency excitation applied to MRE, there is a slight increase of the damping ratio with as the magnetic field increases [38]. Moreover, [38] mentioned that this initial rise of the damping ratio results from energy and friction dissipation between ferromagnetic particles which lead to subsiding and type of the polymer matrix significantly influence the damping ratio, natural rubber is the most suitable due to its low damping ration so that it can be used as a vibration absorbers. Therefore, in most cases the effect of electric current and magnetic field on MRE damping ratio is ignored theoretically whereas on the other hand the change in stiffness is usually taken into account. However, a study showed that the damping coefficient decreases slightly with more carbonyl iron particles composition [39].

Many studies have been done to observe the characteristics and behavior of MRE. [37] proved that uniaxial field structured composites containing a magnetic iron particles embedded with an elastomer (MRE) shows a significant and rapid increases in modulus of elasticity than particles with a random distribution as shown in Figure 11, this happens when the applied stress is parallel to the alignment of the particles. In

addition, several parameters in the MRE can affect its behavior and characteristics. These parameters include the particles shape and size, volume fraction, and the distribution in the matrix. [40] done a testing of double lab shear specimens. Fixed strain oscillations are applied to the specimen, the phase and amplitude of the output force are measured, from which modulus and stress were calculated. It was shown that the modulus increases as the magnetic field increases. In addition, the modulus is higher as the volume fraction increases.
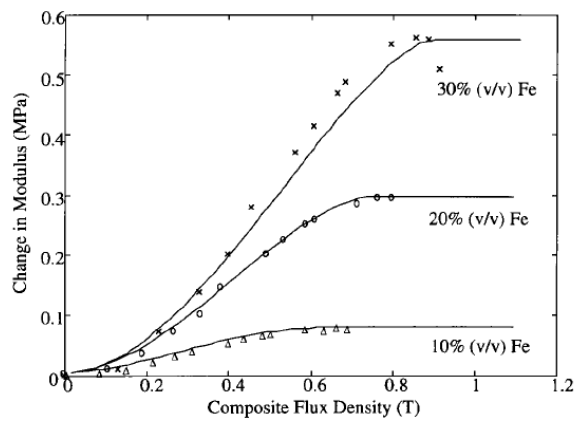
Figure 11. The response of the modulus of elasticity to applied field for 10% (h = 1:29, k = 5), 20% (h = 1:08, k = 12) and 30% (h = 1:0, k = 15) volume fraction of iron particles to the elastomer matrix [37].

Similar study was done to observe the magneto rheological (MR) effect when changing the particles sizes, the particles were varied in diameter while fixing the geometry of the elastomer. It was shown that the modulus of elasticity decreases as the particle size increase. This was stated due to the varying interactions between particles surfaces [41]. [42] conducted a static and compression tests on a cylindrical MRE with both diameter and height of 20 mm. The elastomeric polymer was made of HB 6013 isocyanate while the particles were carbonyl iron with size of 6-9 μm. It was concluded that the effect of the magnetic field is higher than changing the frequency

18

of the excitation force which can be referred to the minor range of its variation. [43] studied the field-stiffening effect of MRE in both shear and axial deformation. The magnetic field was applied to the direction of the particles chain and it is found that the magnetic interaction between particles is the main factor affecting the stiffness. [44] done an experimental investigation on the static properties of MRE, results showed that the stiffness of the MRE has a direct proportionality with the current applied, hence, magnetic field. As shown in Figure 12.
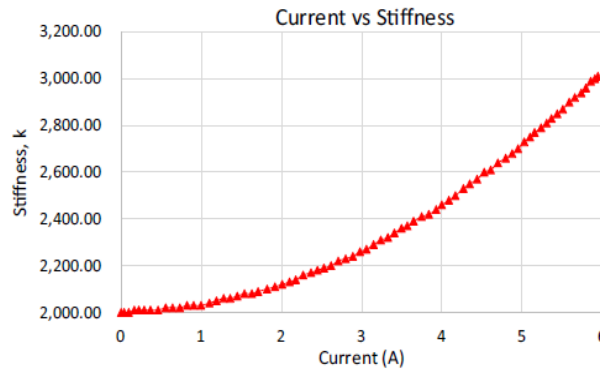
Figure 12. Stiffness (MRE) vs current [44].

2.2.2.2 Mathematical models of MR dampers and their applications

Many phenomenological models have been developed to deal with the elastic behavior of MR dampers described by Hooke's law, and the viscous properties which are described by Newton's law. MR dampers display the characteristics of both elastic and viscous materials [45]. They are called viscous-elastic materials. These models are employing combinations of dashpots and springs to describe the functions of materials. Some of the famous models are reviewed and their usage in different applications. Table 1 shows the schematic representations and mathematical models of these models.

One of the most used model to describe the viscous-elastic behavior of MR

damper is Bingham model. It assumes the material to be rigid before yielding. This model is sufficient to provide a rough approximation of force with respect to velocity. It is not suitable to be utilized in dynamic applications due to limited description of the material's properties at small deformations [46]. The schematic representation is shown in Figure 14. This model has been used widely in different applications for vibration isolation. For example, [47] have used Bingham model to control cable vibrations. Numerical simulations results in the effectiveness of this model to suppress vibrations in their mathematical model. In addition, [48] studied the behavior of this model using squeeze test numerically and compared it to the experimental results, results showed a great agreement. In addition, parameters identification was done to create a relationship between these parameters and current (magnetic field).

[49] developed a model that shows the hysteretic behavior of MR damper. This model resembles characteristics and behavior of the damper. Therefore, it is more efficient than Bingham model. However, this model does not have the ability to fully describe the behavior of non-linear force with respect to the velocity response at yield region. This model is presented schematically in Figure 15. [50] used Bouc-wen model as a semi-active suspension system and compared it to a passive suspension system, a quarter car model with two degrees of freedom body suspension wheels. This was simulated using MATLAB (Simulink). Results showed that using Bouc-Wen model as a semi-active damper improved. [51] concluded that the Bouc-Wen model is able to show the non-linear behavior of mild steel damper.

Similar to Bouc-Wen model, [49] adopted a 14-parameter model as shown in Figure 16; the modified Bouc-Wen model. This model considers the high non-linear behavior of MR damper as it enhances the accuracy of determining MR damper behavior. There is a limitation in this model due to the difficulty in approximating the

high number of model parameters. This is because it is assumed that the relationship between these coefficients and applied current is linear. However, [52] applied a method called non-linear least squares fitting in order to get more accurate estimations of those parameters. This method was also used to estimate the parameters of different other model such as Bingham model, simple Bouc-Wen model, and hyperbolic tangent function model. [53] introduced a novel method in estimating heart motion by applying this model to respiratory signals from a body. It is suggested that this model can be used as a robust unified framework to model hysteresis visualization in respiratory heart motion due to its accurate estimation of the MR damper behavior.

Dahl model is one of the models developed to describe the behavior of MR dampers [54]. This model can be considered as a special case of the simple Bouc-Wen model with some differences in its parameters. The advantage of this model is that it reconstructs Coulomb forces to avoid the estimation of excessive coefficients [55]. In addition, the force-displacement response is well predicted. The model can be shown in Figure 17. [56] studied the dynamic analysis of spatial linkages using Dahl model. In addition, [57] used this model for a grab crane dynamic analysis, it was shown that this model is useful in the process of design.

In 2014, [58] proposed a new model consisting of three parameters by which a dashpot element and a hysteresis component are connected in series. This model is presented in Figure 18. [59] applied this model to predict its parameters using improved particle swarm optimization. Results showed that the force-displacement/velocity responses are predicted well in small and large displacement.

[60] proposed a new model that utilizes a hyperbolic sine function to represent the hysteresis in order to describe the stiffness and damping characteristics. This model was proposed and its parameters were identified using the modified artificial

fish swarm algorithm [61], results of this model showed a satisfactory agreement with the experimental outcomes

[62-63] developed a model as an extension and development of Dahl model in order to characterize MR materials friction dynamics. This model is a combination of spring element, a viscous dashpot and LuGre friction component. The formulation of this model is represented in Figure 19. This model was used on an industrial pneumatic cylinder and was validated with experimental results [63]. Results showed that LuGre model shows an intermediate trade-off between accuracy and complexity.

[64] has simulated different models of MR dampers in an application in order to compare between them. [64] presented and simulated numerically several models on the quarter-car suspension system in a vehicle. In addition, this study includes the passive vibration isolation approach. Simulations were run for four different excitation frequencies to mimic the roughness of the suspension system. Their results showed that Bingham and Bouc-Wen models behaved better than other models as shown in Figure 13.
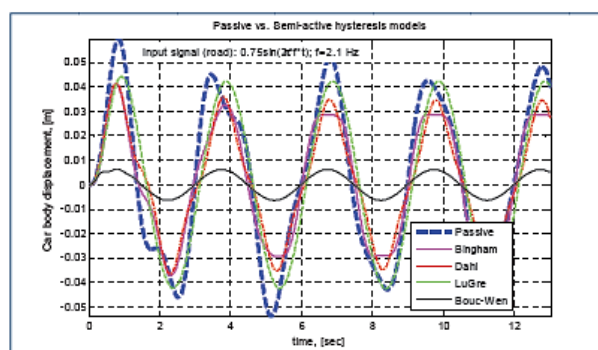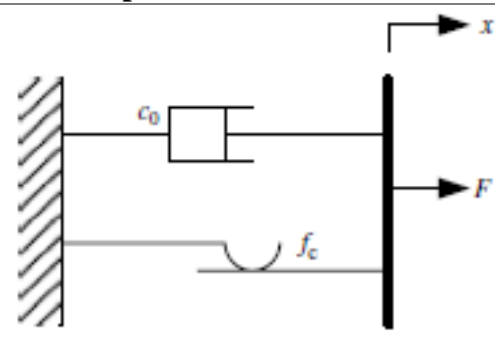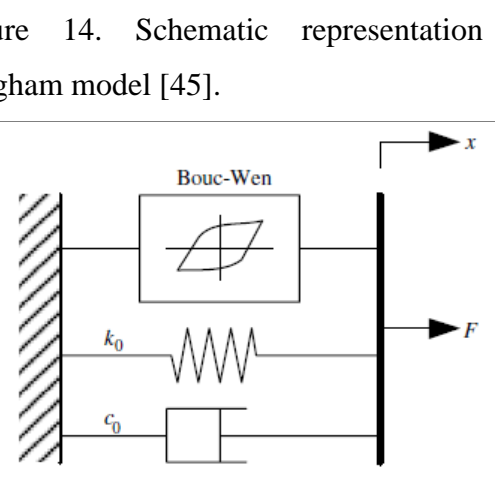
Figure 13. Passive vs. MR damper models suspension on sinusoidal wave: 0.075sin(2πft), f = 2.1 Hz [64].

Table 1. Summary of different MRE models.

Schematic representation of models	Mathematical expression by the damping force, F
  Figure 14. Schematic representation of Bingham model [45].	$F = f_c sgn(\dot{x}) + c_0 + f_0$ (1) where f_c is the friction force due to yield stress is, c_0 is the damping coefficient, f_0 is the stored force due to the accumulator.
  Figure 15. Schematic representation of simple Bouc-Wen model [49].	$F = \alpha z + c_0 \dot{x} + k_0 (x - x_0)$ (2) $\dot{z} = -\gamma |\dot{x}| z(|z|^{n-1}) - \beta \dot{x} |x|^n + A\dot{x}$ (3) where α is the scaling Bouc-Wen model parameter related to yield stress of MR damper, x_0 is the initial displacement due to effect of accumulator. c_0 and k_0 are the damping coefficient and spring stiffness, respectively. z is the deformation of the model due to hysteretic effect represented by Eq. (3), γ, β, A and n are Bouc-wen model parameters to control the hysteretic loop.

Schematic representation of models	Mathematical expression by the damping force, F
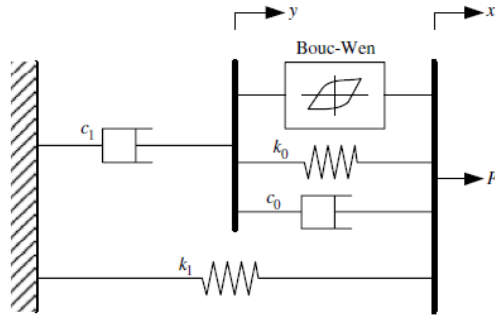
Figure 16. Schematic representation of the modified Bouc-Wen model [49].

$$F = c_1\dot{y} + k_1(x - x_0) \tag{4}$$

$$\dot{y} = \frac{1}{c_0 + c_1}[\alpha z + c_0\dot{x} + k_0(x - y)] \tag{5}$$

$$\dot{z} = -\gamma|\dot{x} - \dot{y}||z|^{n-1}z - \beta(\dot{x} - \dot{y})|z|^n + A(\dot{x} - \dot{y}) \tag{6}$$

where k_1 is the stiffness of the accumulator, x_0 is the initial displacement of spring k_1 due to accumulator effect, y is the internal displacement of the damper, c_1 and c_0 are the viscous damping coefficients at low and high velocities, respectively. z is an evolutionary variable. γ, β, n and A are modified Bouc-wen model parameters for controlling the hysteretic loop similar to the previous model.
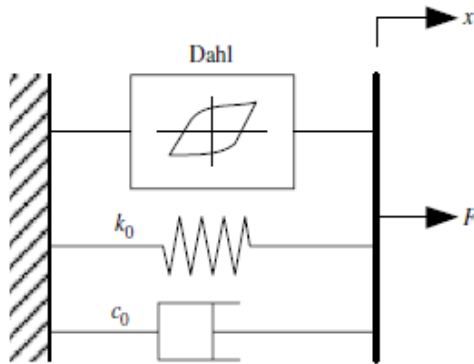
Figure 17. Schematic representation of Dahl

$$F = k_0 x + c_0\dot{x} + \delta z - f_0 \tag{7}$$

$$\dot{z} = \rho(\dot{x} - |\dot{x}|z) \tag{8}$$

where k_0 is the stiffness of the spring, c_0 is the damping coefficient, z is the intermediate variable and ρ is the coefficient of stiffness.

Schematic representation of models	Mathematical expression by the damping force, F

model [54].

Figure 18. Schematic representation of strain-

stiffening model [58].
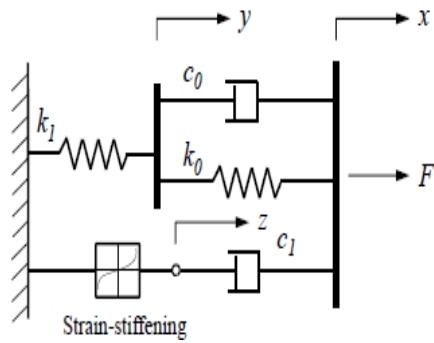
$$F = k_1 y + \alpha z^3 \qquad (9)$$
$$k_1 y = k_0(x - y) + c_0(\dot{x} - \dot{y}) \qquad (10)$$
$$\alpha z^3 = c_1(\dot{x} - \dot{z}) \qquad (11)$$
$$\dot{z} = -\frac{\alpha}{c_1} z^3 + \dot{x} \qquad (12)$$

where k_0 and k_1 ate the stiffness of two springs, c_0 and c_1 are the damping coefficients of the strain-stiffening MRE base isolator, α is a scaling factor, and z and y are an evolutionary variables.

Figure 19. Schematic representation of

$$F = c_0 x + k_0 \dot{x} + \alpha z + F_0 \qquad (13)$$
$$z = sinh(\beta x) \qquad (14)$$

where F_0 is the offset of the isolator force, β is the scale factor of the displacement of the isolator, α is a factor to scale the hysteresis, and c_0 and k_0 are the damping coefficient and spring stiffness, respectively.

Schematic representation of models	**Mathematical expression by the damping force, F**

Hysteresis model [60].
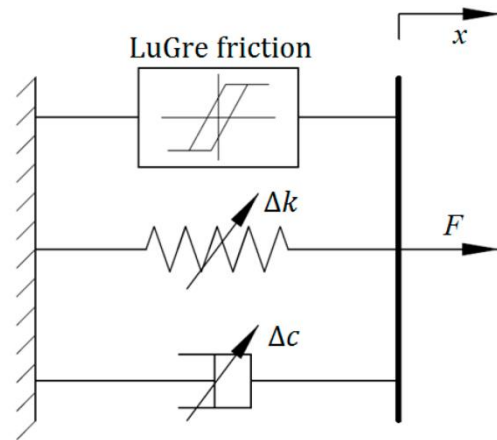
$$F = \frac{\beta}{\alpha}y + c_0\dot{x} + k_0 x + \frac{\varepsilon}{\alpha}\dot{y} + f_0 \tag{15}$$

$$\dot{y} = \alpha\dot{x} - \alpha|\dot{x}|y \tag{16}$$

where β, α, and ε are scale LuGre model parameters for controlling the loop, y is an evolutionary variable, f_0, c_0 and k_0 are the initial force, damping coefficient and spring stiffness, respectively.

Figure 20. Schematic representation of LuGre fiction model [61].

2.2.2.3 MRE in vibration isolation

MRE have been used as vibration isolators in many different applications. Researchers from various disciplines utilized MRE as a damper to isolate vibrations by which a specific part of the structure is needed to avoid vibrations. MRE isolator can be used for protecting buildings from disastrous vibration due to earthquake. [65] has developed a semi-active MRE base isolation system for different benchmark. It was produced with inverse model of general regression neural network (GRNN). It was concluded that it has the ability to speed up the calculation time and training methodology. [66] used MRE to suppress flexural wave on a beam solely on simulation basis. Amount of damping depend on thickness of MRE layer and increasing thickness also result in small or negligible damping. Design of a working prototype of MRE based variable stiffness and damping isolator (VSDI) and real time tested on a 1:16 scaled 3-storey building using Lyapunov-based control strategy. The on and controlled states found to reduce the maximum acceleration and displacement of the building more as compared to the passive state (with controller off).

[67] developed and designed a prototype of MRE using the variable stiffness and damping isolator (VSDI) model applied on a (1:16) scaled three-story building. This analysis was done using Lyapunoy-based control method. Results showed that the maximum acceleration and displacement is reduced using MRE more than using passive vibration isolation strategy. MRE is used in the vibration isolation of a small-scale wind turbine aluminum blade SH3055 (Bergey Wind Power Co. Inc., USA). For turbine blade with controller on, the gain reduction for 1st mode was 15.83dB and 2nd mode was 13.07dB [68].

[69] designed a tunable automotive bushing for vibration isolation on translational and rotational wheels motion using MRE as shown in Figure 21. Steel is

used to make the two concentric hollow cylinders (bushing). Deformation testing was conducting using sinusoidal signal at 2 Hz, results showed that an increase of 25% of the stiffness and damping is obtained in both axial and radial directions. This increase is related to an applied current up to 5 A. [70] achieved a tunable stiffness and damping using four layers of MRE and three coils for magnetic field generation. [71,72] proposed a novel MRE isolator to control vibration in vehicles, stiffness and damping are increased with magnetic field in both compression and shear modes. [73] used MRE for base isolation of a civil structure, four MRE samples were trapezoidal in geometry with 12mm thick are used in the system. Four coils with 800 turns are used in top and bottom to produce magnetic field as shown in Figure 22. Force-displacement response was plotted and a 57% increase within the loops is found for different current.
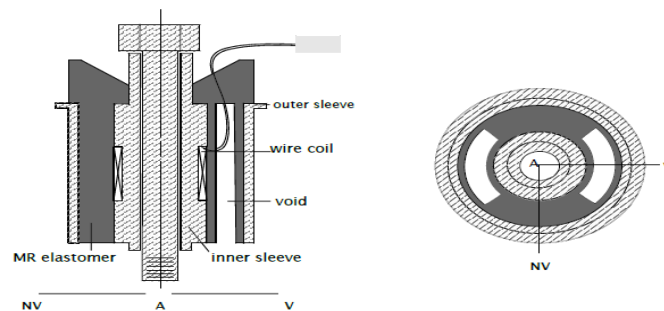
Figure 21. Section view of MRE; NV stands for non-voided direction, V is the voided direction, and A is the axis of rotation of the bushing [69].
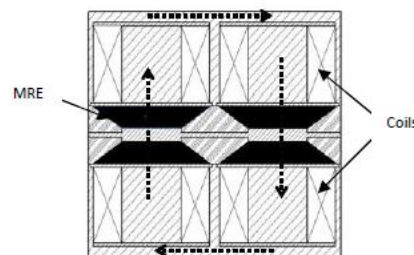
Figure 22. Variable stiffness and damping isolator developed by [73].

[74] used MRE as a semi-active vibration isolator to suppress torsional mode of vibration. The volume fraction of the iron particles is 40% within the elastomer. The setup consists of a power supply, an amplifier, a dynamic signal analyzer (DSA), an inertial shaker, accelerometer and solenoid for magnetic field generation as shown in Figure 23. The frequency range was 0 Hz – 400 Hz and the applied current was up to 6A. Results showed that a shift of 3.9 Hz of the natural frequency achieved. In addition, the damping ratio of the system was slightly decreased with magnetic field. [75] developed the mathematical and experimental setup for dynamic tuning of torsional vibration; it is found that the stiffness of MRE increases with the magnetic field. In addition, the transmissibility curve (θ_2/θ_1) was plotted with respect to the excitation frequency, a shift in the curve was observed as the magnetic field increases.
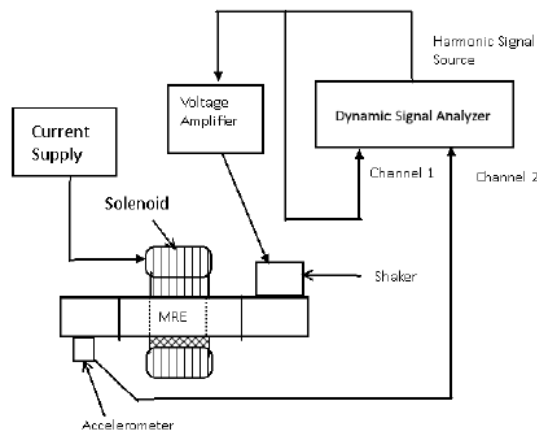
Figure 23. Schematic of semi-active torsional vibration isolater using MRE [74].

2.2.2.4 Numerical modeling of MRE

Many articles have presented a numerical models and studies on MRE. The finite element method (FEA) is one of the most widely used methods for solving problems of mathematical and engineering models. Some of the typical problems include the traditional fields of heat transfer, structural analysis, fluid flow,

29

and electromagnetic potential and mass transport. The FEA is a numerical method for solving partial differential equations (PDEs) in 2D or 3D [76] . FEA has been applied in some studies to simulate the MRE. FEA results showed an innovative magnetic design which is able to provide sufficient and uniform magnetic field to all 25 MRE layers for base isolator presented in [77], it is found that the magnetic field in MRE materials deteriorates when the deformation of the device increases. According to the 2D model of [78], in a microscopic view, the anisotropic MRE unit cell contract under the presence of a magnetic field which results in increased stiffness of the material. This situation is verified in a 3D RVE model by [79]. [80] has simulated magneto-rheological elastomer (MRE) composite beams made of Barium hexaferrite (BaM) and Iron (Fe) powders combined with a highly-compliant matrix material using COMSOL Multiphysics and developed models capable of predicting the actuation behavior of hard- and soft-magnetic MREs.
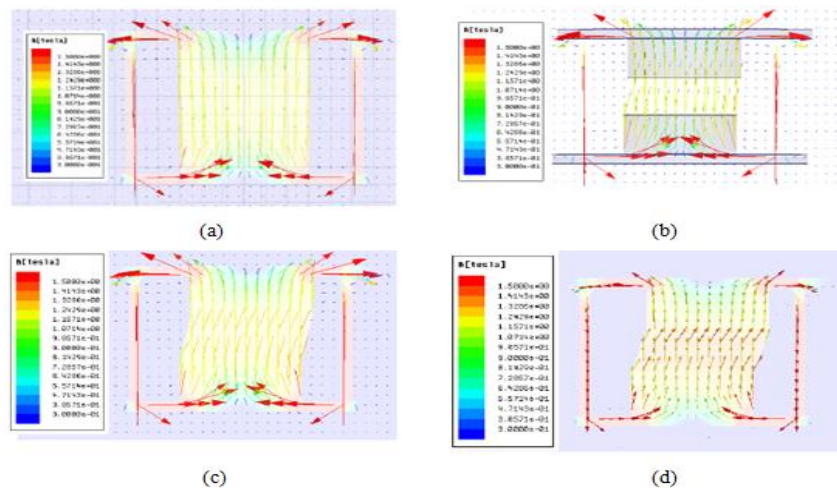
Figure 24. Magnetic flux density of MRE base isolator [82]; (a) no deformation, (b) 5mm, (c) 10mm, and (d) 15mm.

[81] has showed a numerical implementation of a model for rate-dependent magneto-active polymer to get the response of a large deformation magneto-

mechanics. [82] simulated 2D MRE base isolator using ANSYS software to visualize the horizontal deformations of MRE (0mm, 5mm, 10mm and 15mm). It is found that when the deformation increases, the magnetic field decreases along the MRE. These results are shown in Figure 24.

2.3 Vibration Isolation in Drilling Process

Finally in this review, since the application that is used in this research is drilling, it is worth it to collect and report articles which discussed vibration isolation in drilling process. Using MRE, [83] done an experiment to control lateral vibrations of drill on center lathe, results showed that 22% of lateral vibrations are absorbed under magnetic field. This study is limited because the time domain only was obtained. FEM was used for the analysis of vibration in a drill string [83], this work determined the natural vibration modes and forced harmonic response for drill string so that resonance is avoided. Results showed the range of frequencies that can be excited in order to avoid maximum stress and amplitude. [84] presented a new methodology to isolate vibration in drill strings by proposing a type of periodic drill strings with passive periodic inputs, it was concluded that this type of drill strings can operate in a wider range of frequencies than conventional drill strings. It included both FEA and an experimental verification and results showed agreement. [85] have shown a drill bit mitigation analysis to isolate lateral vibrations. It was concluded that using the physical solutions is the only way to overcome drill bit whirl effect. [86] have investigated some solutions to avoid torsional vibrations using a real time display of the magnitude of vibration in the torsional mode. This work was concerned on observing the results of reducing these vibrations, results concluded that the drilling bit life time and drilling rate are enhanced, a reduction in fishing time and minimizing failures of drill string/BHA failures.

Chapter 3: Analytical and Numerical Simulation Studies on MRE

In this chapter, two different studies are done in order to investigate and understand the behavior of MRE when it's exposed to a magnetic field. This chapter is mainly divided into two parts; the 1st part will be simulations of different MRE models presented in Chapter 2, these models are subjected to a base motion isolation (base excitation) system by which it's the main concept of the proposed application (i.e. drilling process) of this research. This is done using MATLAB (Simulink) software. The analysis starts by identifying different models of MRE and their mathematical models, then to apply them on a base isolation system with different excitation inputs. The second part of this chapter is the FEA and numerical modeling MRE in 3D in order to study its behavior under magnetic field. These analyses were done in order to understand the characteristics of MRE and how its mechanical properties are changed by applying a magnetic field.

3.1 Analytical Simulations of Different MRE Models Using MATLAB

3.1.1 Mathematical model development

The methodology of this study is to use MRE in semi-active vibration isolation by which the parameters can be controlled. The system can be presented as a simple base motion isolation (base excitation) system by which the excitation input to the base is to be isolated on the mass. This model is developed to represent the MRE mathematically. The mathematical model of the system is a description in terms of equations. Newton's and conservation of energy are the physical laws as well as the basics in building the model. This system considers a one degree of freedom base excitation system as shown in Figure 25. The system is excited by an input displacement $y(t)$ applied to the base, and an output displacement $x(t)$ on the mass.
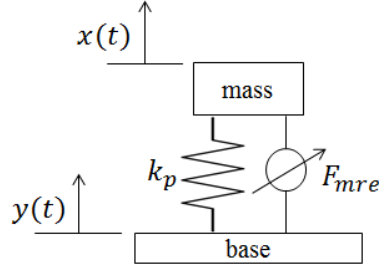
Figure 25. Schematic representation of base isolation model utilizing MRE.

The equation of motion is based on applying a second order differential equations and Newton law and it becomes

$$\sum F = m\,\ddot{x} \tag{17}$$

$$m\,\ddot{x} = -k_p(x - y) - F_{mre} \tag{18}$$

$$m\ddot{x} + k_p x + F_{mre} = k_p y \tag{19}$$

Knowing that the force of the MRE is given by

$$F_{mre} = k_{mre}(x - y) + [c_p + c_{mre}](\dot{x} - \dot{y}) \tag{20}$$

Then, Eq. (19) becomes

$$m\ddot{x} + [c_p + c_{mre}]\dot{x} + [k_p + k_{mre}]x = [c_p + c_{mre}]\dot{y} + [k_p + k_{mre}]y \tag{21}$$

This is the equation of motion presents the dynamics of the system modeled in terms of m, the mass, y, the input displacement, x, the relative output mass displacement, c_p, the passive damping coefficient of MRE when no magnetic field is applied, c_{mre}, the active damping coefficient of MRE when the magnetic field is applied, k_p, the passive stiffness of MRE when no magnetic field is applied, k_{mre}, the active damping coefficient of MRE when the magnetic field is applied. The passive term of the damping coefficient c_p isn't presented in Figure 25 and this is due to the fact that its change under magnetic field is not considerable. However, it's included in the total MRE damping force F_{mre} as in Eq. (20) To simplify the equation, let

$k = k_p + k_{mre}$ and $c = c_p + c_{mre}$, Eq. (21) becomes

$$m\ddot{x} + c\dot{x} + kx = c\dot{y} + ky \tag{22}$$

Deriving system transfer function is a very important step since it reflects the overall system performance and it represents the plant function of the system in case of control system development. Mathematically, in term of analogue system transfer function can be achieved by taking a Laplace transform to the differential equation of motion then the ratio of output displacement to input displacement can be easily found, by considering Laplace transform (a= A(s)) on Eq. (22)

$$ms^2X(s) + csX(s) + kX(s) = csY(s) + kY(s) \tag{23}$$

$$X(s)[ms^2 + cs + k] = Y(s)[cs + k] \tag{24}$$

$$\frac{X(s)}{Y(s)} = \frac{cs + k}{ms^2 + cs + k} \tag{25}$$

In mechanical vibration the concept of displacement transmissibility is very significance. It is the ratio of how much oscillation is transmitted from the source of excitation to the load. The analysis of transmissibility factor is carried out frequency domain in terms of amplitude and phase. Furthermore, it is quite similar to the system transfer function therefore in order to obtain mathematical equation, Eq. (25) should be changed to frequency domain by using the conversion from (s-domain) to ($\omega -$ domain) through substituting ($s = j\omega$), the transmissibility factor is given by

$$\frac{X(j\omega)}{Y(j\omega)} = \frac{c\,j\omega + k}{m(j\omega)^2 + cj\omega + k} \tag{26}$$

By taking the magnitude of Eq. (26), the amplitude of displacement transmissibility can be found through Eq. (27)

$$T = \left|\frac{X(\omega)}{Y(\omega)}\right| = \sqrt{\frac{(c\omega)^2 + k^2}{(c\omega)^2 + (k - m\omega^2)^2}} \tag{27}$$

3.1.2 Analytical simulation methodology

The simulations are based on the mathematical model described in the previous section. The methodology can be explained further in the representation in Figure 26. Five models are selected from the literature to be modeled and simulated on the base excitation system. MRE properties vary under a magnetic field. Each model has its own mathematical representation and equations by which their parameters are a function of magnetic field; this magnetic field is inputted as an electric current. The simulation is done for each model with and without MRE. When the system is without MRE, it means that the effect of stiffness and damping is not related to the current; therefore, the system is considered as free vibration where the oscillation will never end. The current is varied from 0 A to 4 A. Step and sinusoidal excitations is applied to the base, $y(t)$. The mass in this analysis is assumed to be 5 kg. Inputs parameters are shown in Table 2.
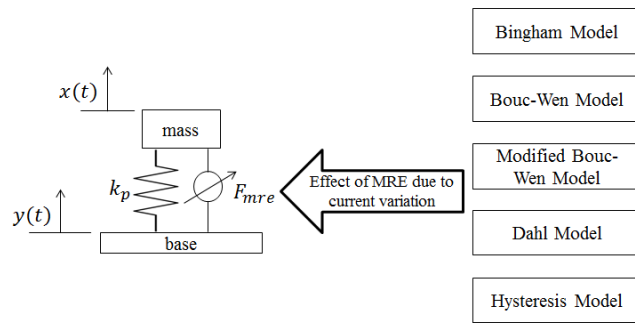
Figure 26. Representation of the analytical simulation study using different MRE models.

Table 2. Excitation Inputs for the Analytical Simulations.

Input	Parameters	Values
Step	Step time	0.5
	Initial value	0
	Final value	1
Sine wave	Amplitude	1 m
	Frequency	10 rad/s

3.1.2.1 Equations and models simulations strategy

From the literature, it is proved that the damping properties of MRE do not change much under a magnetic field whereas the stiffness changes significantly. Therefore, to simplify the model, the passive damping term $c_p(\dot{x} - \dot{y})$ will not be eliminated but will be gathered into the total MRE force, F_{mre}. Hence,

$$F_{mre} = k_{mre}(x - y) + [c_p + c_{mre}](\dot{x} - \dot{y}) \tag{28}$$

By combining Eq. (21), it reduces to

$$m\ddot{x} = -k_p(x - y) - F_{mre} \tag{29}$$

$$\ddot{x} = -\frac{k_p}{m}(x - y) - \frac{F_{mre}}{m} \tag{30}$$

All mathematical models and expressions of these models are reviewed in details in the literature review. However, Table 3 below briefly summarizes the five models that will be studied. In addition, the mechanical properties of these models of MRE are changeable by applying a current. These relationships with their parameters are also presented which were taken from the literature [49-63]. Some of models parameters are constant and others are field-dependent; by which they depend on the magnetic field which related to the current. In addition, these relationships can be linear and non-linear. These relationships and data for parameters are shown in Table 4.

Table 3. Summary of Different MRE Models in terms of their Mathematical Model and Parameters.

MRE Model	Mathematical equations	Parameters explanation
Bingham	$F = f_c sgn(\dot{x}) + c_0 + f_0$	where f_c is the friction force due to yield stress is, c_0 is the damping coefficient, f_0 is the stored force due to the accumulator.
Bouc-Wen	$F = \alpha z + c_0 \dot{x} + k_0(x - x_0)$ $\dot{z} = -\gamma|\dot{x}|z(|z|^{n-1}) - \beta\dot{x}|x|^n + A\dot{x}$	where α is the scaling Bouc-Wen model parameter related to yield stress of MR damper, . x_0 is the initial displacement due to effect of accumulator. c_0 and k_0 are the damping coefficient and spring stiffness, respectively. z is the deformation of the model due to hysteretic effect, γ, β, A and n are Bouc-wen model parameters to control the hysteretic loop.
Modified Bouc-Wen	$F = c_1 \dot{y} + k_1(x - x_0)$ $\dot{y} = \dfrac{1}{c_0 + c_1}[\alpha z + c_0\dot{x} + k_0(x - y)]$ $\dot{z} = -\gamma|\dot{x} - \dot{y}||z|^{n-1}z - \beta(\dot{x} - \dot{y})|z|^n + A(\dot{x} - \dot{y})$	where k_1 is the stiffness of the accumulator, x_0 is the initial displacement of spring k_1 due to accumulator effect, y is the internal displacement of the damper, c_1 and c_0 are the viscous damping coefficients at low and high velocities, respectively. z is an evolutionary variable. γ, β, n and A are modified Bouc-wen model parameters for controlling the hysteretic loop similar to the previous model.
Dahl	$F = k_0 x + c_0 \dot{x} + \delta z - f_0$ $\dot{z} = \rho(\dot{x} - |\dot{x}|z)$	where k_0 is the stiffness of the spring, c_0 is the damping coefficient, z is the intermediate variable and ρ is the coefficient of stiffness.
Hysteresis	$F = c_0 x + k_0 \dot{x} + \alpha z + F_0$ $z = sinh(\beta x)$	where F_0 is the offset of the isolator force, β is the scale factor of the displacement of the isolator, α is a factor to scale the hysteresis, and c_0 and k_0 are the damping coefficient and spring stiffness, respectively.

Table 4. Field-Dependency between Models Parameters and Current [49-63].

MRE Model	Field-dependent parameters equations
Bingham	$c_0 = 147.5i + 13.52\ [N.s/m]$ $f_c = -394.8i + 38.14\ [N]$ $f_0 = 663.56i + 52.19\ [N]$
Bouc-Wen	$k_0 = k_{0_a} + k_{0_b}i\ [N/m]$ $c_0 = c_{0_a} + c_{0_b}i\ [N.s/m]$ $\alpha = \alpha_a + \alpha_b i\ [N/m]$ $A, \beta, \gamma, and\ n$ are constants, where $k_{0_a} = 469\ N/m$, $k_{0_b} = 323.2\ N/m.A$, $c_{0_a} = 2100\ N.s/m$, $c_{0_b} = 350\ N.s/m.A$, $\alpha_a = 14000\ N/m$, , $\alpha_b = 69500\ N/m.Am$, $A = 301$, $\beta = 3630000\ m^{-2}$, $\gamma = 190\ s^{-1}$ and $n = 2$.
Modified Bouc-Wen	$k_0 = k_{0_a} + k_{0_b}i\ [N/m]$ $k_1 = k_{1_a} + k_{1_b}i\ [N/m]$ $c_0 = c_{0_a} + c_{0_b}i\ [N.s/m]$ $c_1 = c_{1_a} + c_{1_b}i\ [N.s/m]$ $\alpha = \alpha_a + \alpha_b i\ [N/m]$ $A, \beta, \gamma, and\ n$ are constants, where $k_{0_a} = 500\ N/m$, $k_{0_b} = 15.9\ N/m.A$, $k_{1_a} = 469\ N/m$, $k_{1_b} = 323.2\ N/m.A$, $c_{0_a} = 2100\ N.s/m$, $c_{0_b} = 350\ N.s/m.A$, $c_{1_a} = 28300\ N.s/m$, $c_{1_b} = 295\ N.s/m.A$, $\alpha_a = 14000\ N/m$, , $\alpha_b = 69500\ N/m.A$, $\beta = 3630000\ m^{-2}$, $A = 301$, $\gamma = 190\ s^{-1}$ and $n = 2$.
Dahl	$k_0 = k_{0_a} + k_{0_b}i\ [N/m]$ $c_0 = c_{0_a} + c_{0_b}i\ [N.s/m]$ $\delta = \delta_a + \delta_b i$ ρ is constant, where $\rho = 25\ kg/m^3$, $f_0 = 0.001$, $k_{0_a} = 800\ N/m$, $k_{0_b} = 250\ N/m$, $c_{0_a} = 24.64\ N.s/m$, $c_{0_b} = 40.41\ N.s/m.A$, $\delta_a = 0.031$, and $\delta_b = 1.12$.
Hysteresis	$c_0 = c_{0_a} + c_{0_b}i\ [N.s/m]$ $k_0 = k_{0_a} + k_{0_b}i\ [N/m]$ $\alpha = \alpha_a + \alpha_b i$ β is constant, where, , $c_{0_a} = 315.9\ N.s/m$, $c_{0_b} = 2.74\ N.s/m.A$, $k_{0_a} = 246.7\ N/m$, $k_{0_b} = 31.2\ N/m.A$, $\alpha_a = 17653\ N/m$, $F_0 = 0\ N$, $\alpha_b = 1.553\ N/m.A$, and $\beta = 8570000\ m^{-2}$

The combination of the base isolation system and the damping force by these models is done by combining Eqs. (1)-(8),(13)(14)), and Eq. (30). For example, the

mathematical expression for this methodology can be given as follows, reconsidering Eq. (1) for Bingham model mathematical expression

$$F = f_c sgn(\dot{x}) + c_0 + f_0$$

From Eq. (30), equation for base motion isolation system is

$$\ddot{x} = -\frac{k_{p_{Bingham}}}{m}(x - y) - \frac{F_{mre}}{m}$$

By combining Eq. (1) and Eq. (30), and considering the relative motion between the mass output motion $x(t)$, and base input excitation $y(t)$, by which $x = (x - y)$ and $\dot{x} = (\dot{x} - \dot{y})$, Bingham model damping force becomes

$$F_{BinghamMR} = f_c sgn(\dot{x} - \dot{y}) + c_0 + f_0 \tag{31}$$

The combination of Bingham model damping force and the base isolation system becomes

$$\ddot{x} = -\frac{k_{p_{Bignham}}}{m}(x - y) - \frac{1}{m}(f_c sgn(\dot{x} - \dot{y}) + c_0 + f_0) \tag{32}$$

The equation in this form is preferable since it's a second order differential equation to build the block diagram on Simulink. All models followed the same procedure to be built on Simulink. Block diagrams and combination of equations of these five models are shown in Figures (28-32). In parallel, the block diagrams are related also to some MATLAB codes developed in order to be simulated. Firstly, the MATLAB code is run for each model which is consists of the field-dependent parameters equations as shown previously in Table 4. Then, the models will be automatically opened and simulated using 'open' and 'sim' commands in MATLAB. The simulations are done twice for a step input and sinusoidal input with the parameters shown previously in Table 2. A manual switch is used to connect each input once at a time. Time domains for both inputs are taken as the output of these simulations. All MATLAB codes are shown in Appendix A. Finally, the system with

and without MRE are shown in a scope and extracted. All of the five MRE models are summed up as sub-systems so that simulations are done in at the same time. This methodology can be shown in Figure 27.
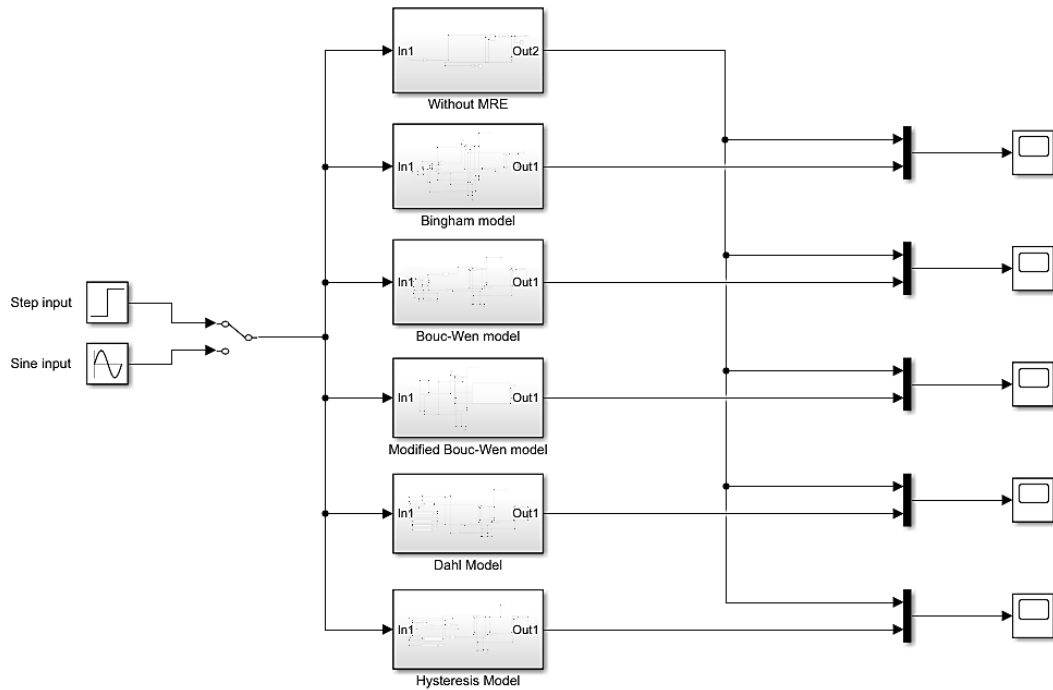
Figure 27. Simulink simulation as a subsystems for different MRE models.

Bingham model Simulink block diagram and combined equations

$$F_{BinghamMR} = f_c sgn(\dot{x} - \dot{y}) + c_0 + f_0 \tag{33}$$

$$\ddot{x} = -\frac{k_{p Bingham}}{m}(x - y) - \frac{1}{m}(f_c sgn(\dot{x} - \dot{y}) + c_0 + f_0) \tag{34}$$
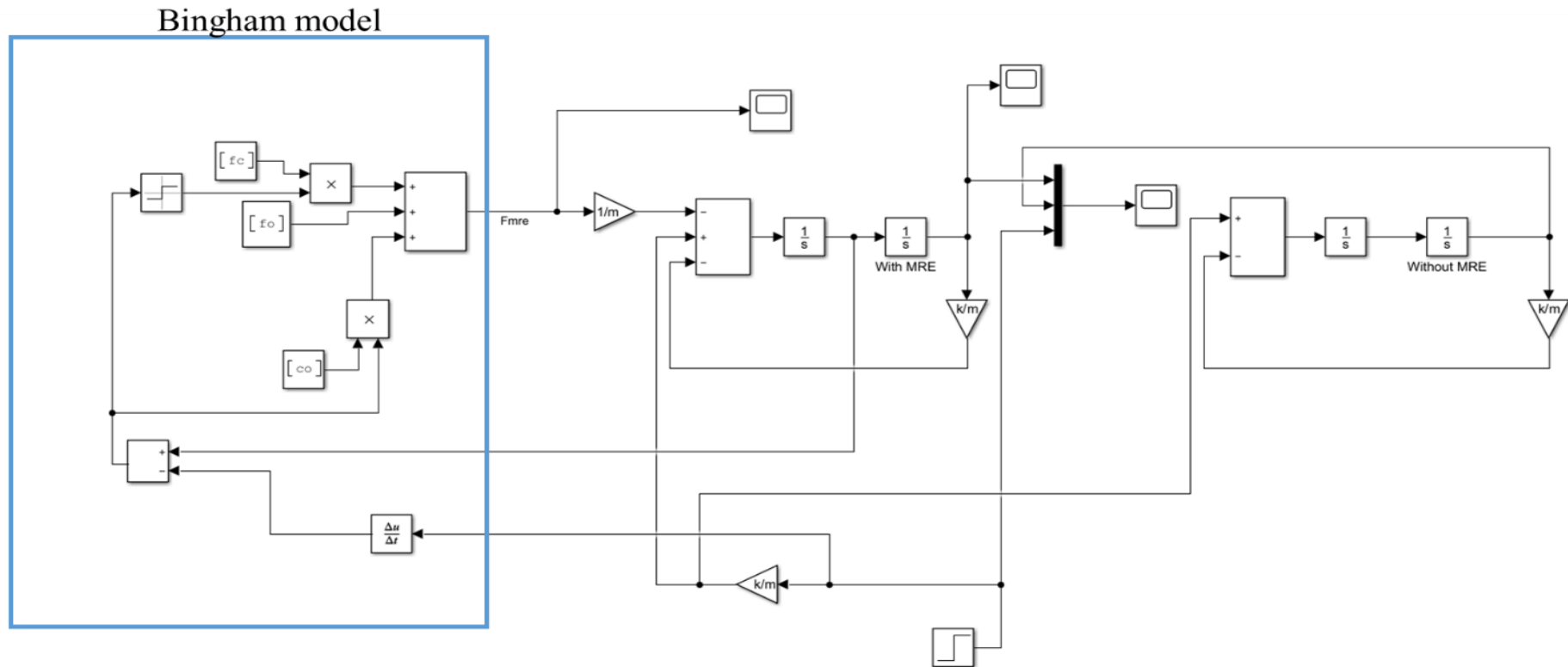
Figure 28. Simulink block diagram for Bignham MRE model on base isolation.

Bouc-Wen model Simulink block diagram and combined equations

$$F_{BoucWenMR} = \alpha z + c_0(\dot{x} - \dot{y}) + k_0[(x - y) - x_0] \tag{35}$$

$$\dot{z} = -\gamma|\dot{x} - \dot{y}|z(|z|^{n-1}) - \beta(\dot{x} - \dot{y})|x - y|^n + A(\dot{x} - \dot{y})) \tag{36}$$

$$\ddot{x} = -\frac{k_{p_{BW}}}{m}(x - y) - \frac{1}{m}(\alpha z + c_0(\dot{x} - \dot{y}) + k_0[(x - y) - x_0]) \tag{37}$$
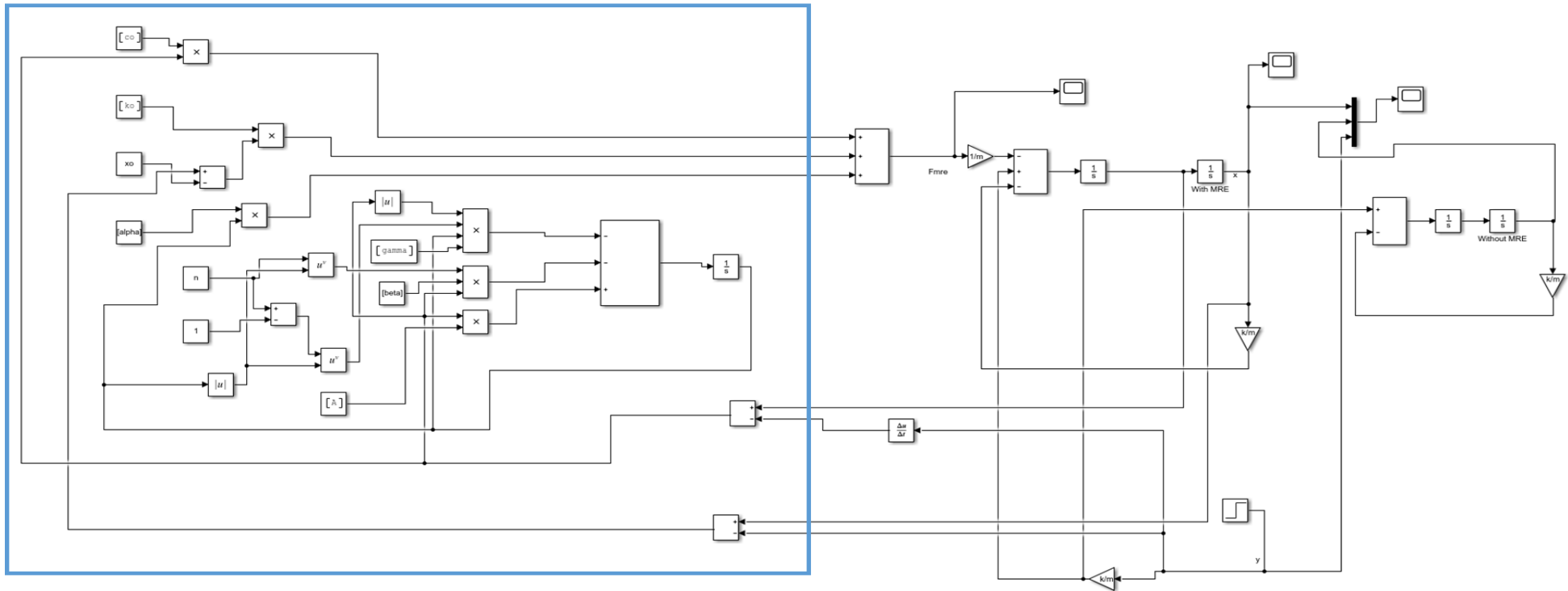
Figure 29. Simulink block diagram for Bouc-Wen MRE model on base isolation.

Modeified Bouc-Wen model Simulink block diagram and combined equation

$$F_{MBoucWenMR} = c_1(\frac{1}{c_0 + c_1}[\alpha z + c_0(\dot{x} - \dot{y}) + k_0\{(x - y) - \boldsymbol{y}\}]) + k_1((x - y) - x_0) \tag{38}$$

$$\dot{z} = -\gamma|(\dot{x} - \dot{y}) - \boldsymbol{\dot{y}}||z|^{n-1}z - \beta((\dot{x} - \dot{y}) - \boldsymbol{\dot{y}})|z|^n + A((\dot{x} - \dot{y}) - \boldsymbol{\dot{y}}) \tag{39}$$

$$\ddot{x} = -\frac{k_{p_{MBW}}}{m}(x - y) - \frac{1}{m}(c_1(\frac{1}{c_0 + c_1}[\alpha z + c_0(\dot{x} - \dot{y}) + k_0\{(x - y) - \boldsymbol{y}\}]) + k_1((x - y) - x_0)) \tag{40}$$
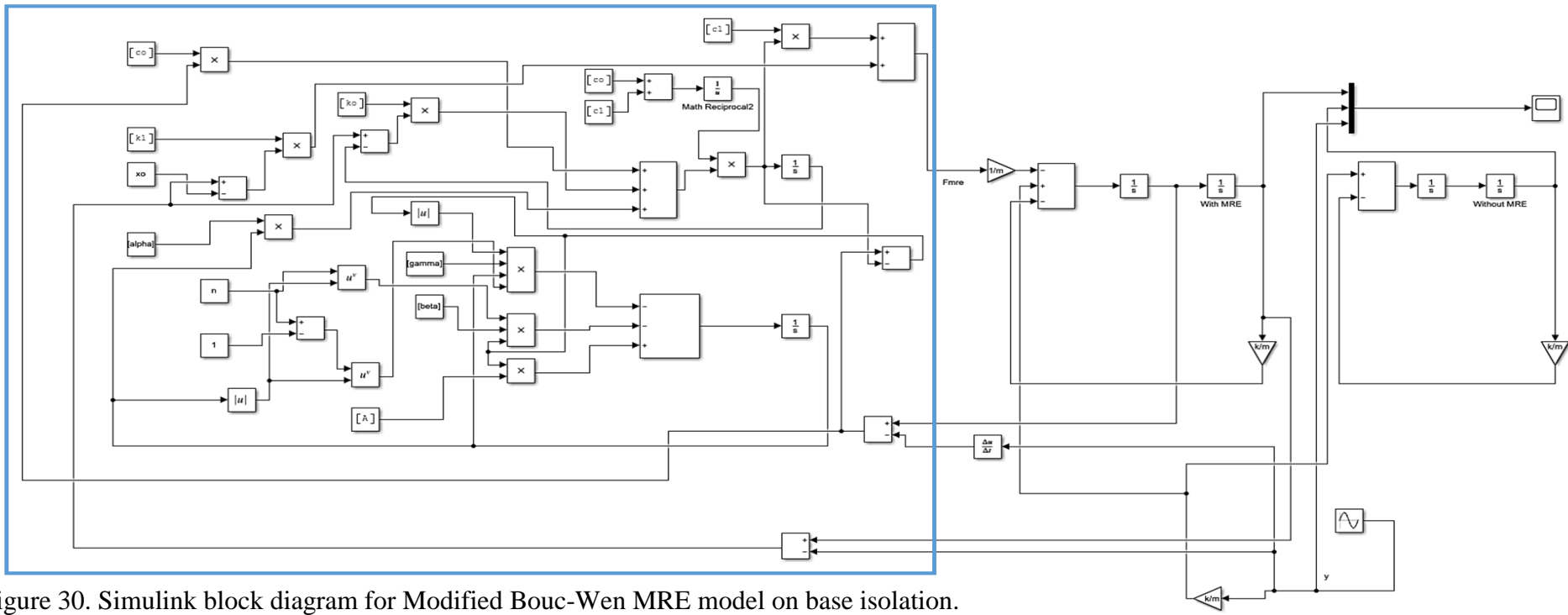
Figure 30. Simulink block diagram for Modified Bouc-Wen MRE model on base isolation.

Dahl model Simulink block diagram and combined equation

$$F_{DahlMR} = k_0(x - y) + c_0(\dot{x} - \dot{y}) + \delta z - f_0 \tag{41}$$
$$\dot{z} = \rho([\dot{x} - \dot{y}] - |\dot{x} - \dot{y}|z) \tag{42}$$
$$\ddot{x} = -\frac{k_{p_{Dahl}}}{m}(x - y) - \frac{1}{m}(k_0(x - y) + c_0(\dot{x} - \dot{y}) + \delta z - f_0) \tag{43}$$
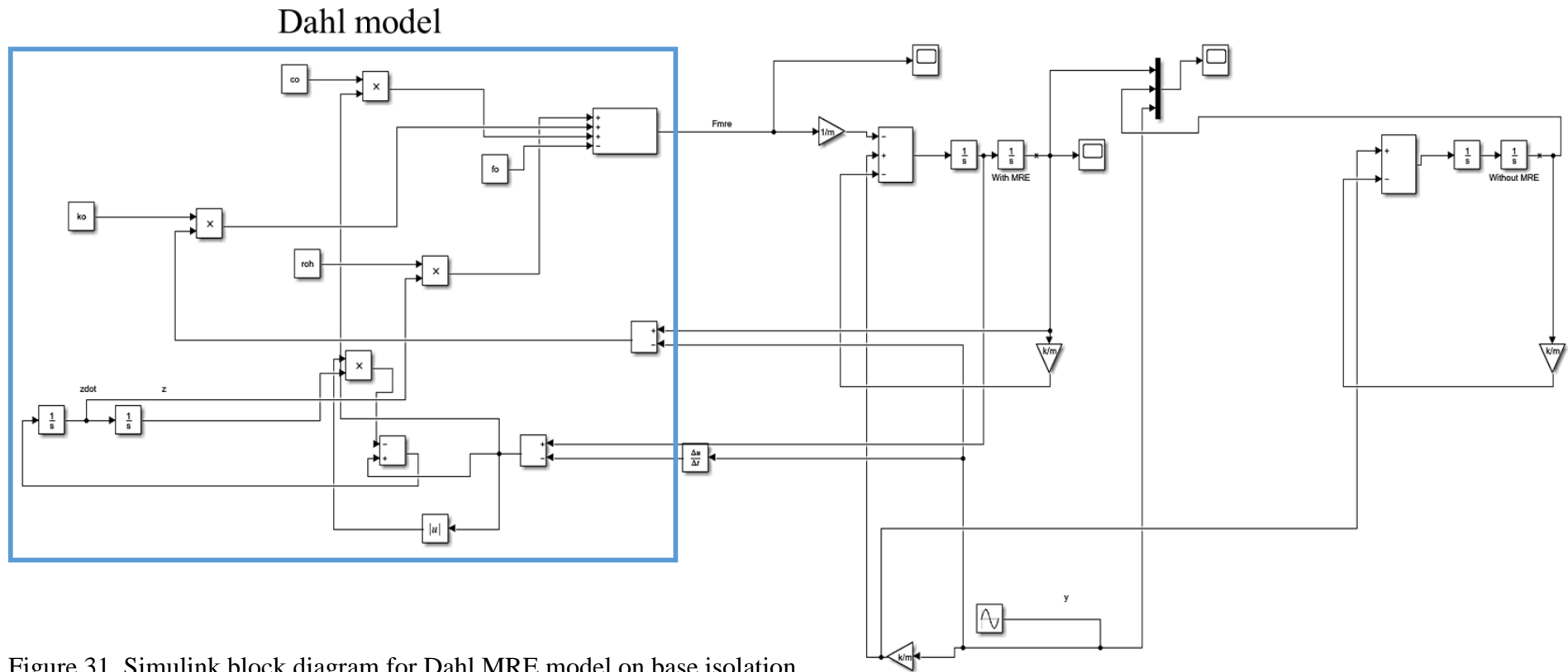
Figure 31. Simulink block diagram for Dahl MRE model on base isolation.

Hysteresis model Simulink block diagram and combined equation

$$F_{HysteresisMR} = c_0(x - y) + k_0(\dot{x} - \dot{y}) + \alpha z + F_0 \tag{44}$$
$$z = sinh(\beta[x - y]) \tag{45}$$
$$\ddot{x} = -\frac{k_{p_{Hysteresis}}}{m}(x - y) - \frac{1}{m}(c_0(x - y) + k_0(\dot{x} - \dot{y}) + \alpha z + F_0) \tag{46}$$
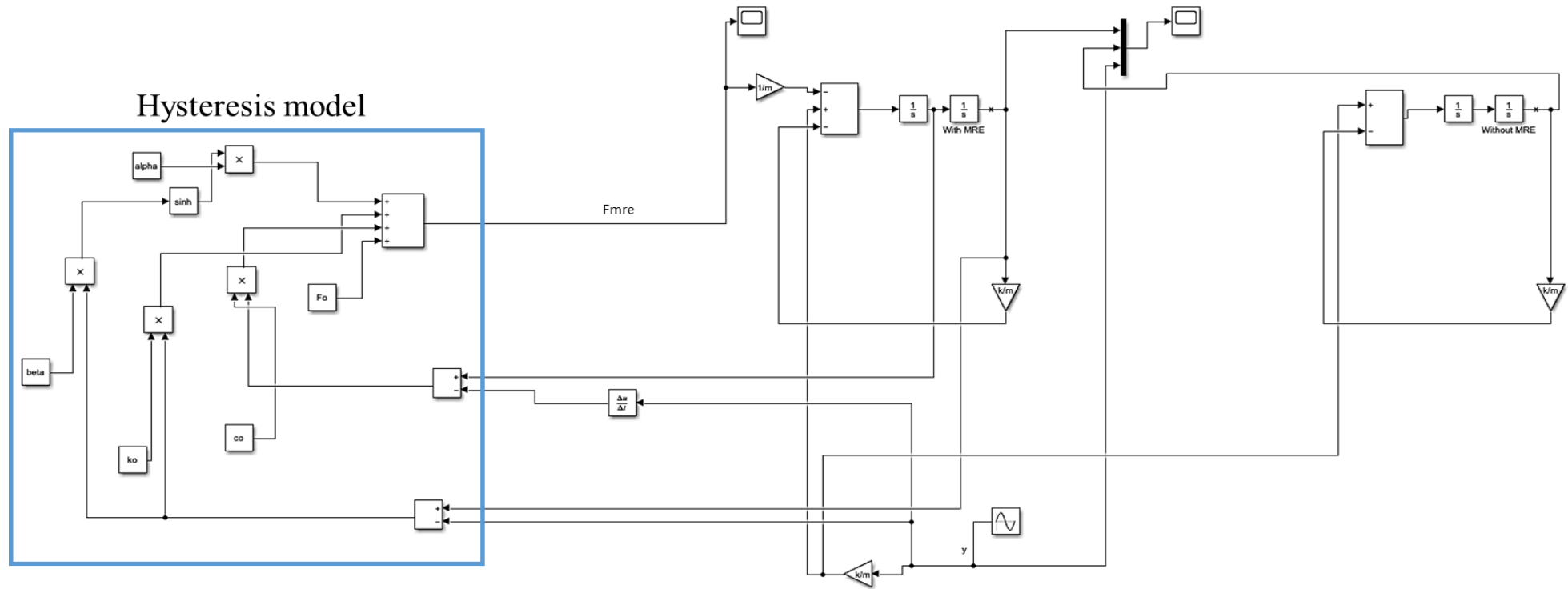
Figure 32. Simulink block diagram for Hysteresis MRE model on base isolation.

3.1.2.2 Simulation study to obtain the Transmissibility curve

The methodology followed to get the transmissibility curves is a completion to time domain methodology and results in the previous section. From the time domain results (amplitude vs time), the values of c, the damping coefficient and k, the stiffness of the MRE are calculated by the following procedure. The time domain of an underdamped second order system is shown in Figure 33.
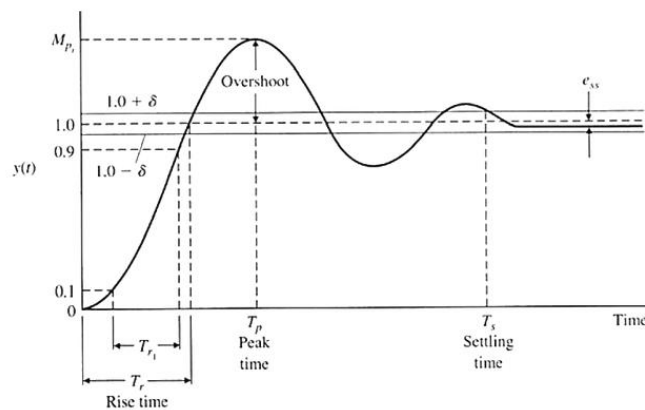
Figure 33. Underdamped second order system [87].

From the figure above, there are some parameters that can be calculated from the time domain response for a step input. Tr, the rise time which is the time needed for the waveform to reach the final value, Tp, peak time which is the time required to achieve the 1st or maximum peak, Ts, the settling time which is the time needed for the transient damped oscillation to stay within $\pm 2\%$ of the steady-state value. $\%PO$, the percent overshoot which is the amount that the waveform exceeds or overshoots the steady-state, or final value at the peak time. From this theory, Tp and $\%PO$ can be found from the time domain plots using MATLAB, c and k values can be calculated, the damping ratio, ζ, can be expressed in terms of $\%PO$ by

$$\zeta = \frac{\left|ln(\frac{PO}{100})\right|}{\sqrt{\pi^2 + [ln\left(\frac{PO}{100}\right)]^2}}$$ (47)

The natural frequency can be expressed in terms of the peak time and the percent overshoot as

$$\omega_n = \frac{\pi}{T_p\sqrt{1 - \zeta^2}}$$ (48)

The stiffness of the MRE is expressed by

$$k_{MRE} = \omega^2 m$$ (49)

It is quite helpful in terms of proceeding with simulation studies where the system performance can be evaluated with different range of ζ. The critical damping in terms of MRE stiffness and the mass is obtained by

$$c_c = \sqrt{4mk_{MRE}}$$ (50)

Finally, the damping coefficient of the MRE can be calculated using

$$c_{mre} = \zeta c_c$$ (51)

All these parameters are calculated based on the peak time and the percent overshoot data that were obtained from MATLAB. The values of the stiffness and damping coefficients are plugged in Eq. (27) Reconsidering Eq. (27)

$$T = \left|\frac{X(\omega)}{Y(\omega)}\right| = \sqrt{\frac{(c\omega)^2 + k^2}{(c\omega)^2 + (k - m\omega^2)^2}}$$

To sum up, the methodology followed in order to find the transmissibility factor of the base isolation system utilizing different MRE models started by studying the mathematical models and building the block diagrams for these models on a base isolation system. Secondly, the relationship between current and models parameters are identified and a parametric sweep of current (0 A − 4 A) is done. After that, the models were simulated and iterated five times for different values of current. Time

domain for two excitation inputs (step and sine wave) are obtained. Calculations were done in order to identify the stiffness and damping coefficient of the MRE. Finally, the transmissibility curves with respect to the frequency are obtained. This whole methodology can be explained schematically by the following flowchart
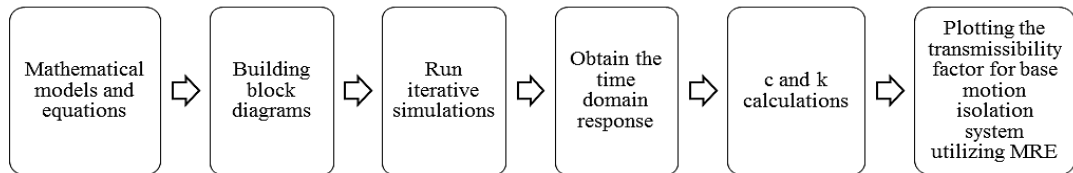
Figure 34. Process representing the analytical simulations methodology.

3.1.3 Analytical simulations results and discussion

The previous sections illustrated the overall methodology including mathematical formulations, block diagrams and transmissibility analysis for five different semi-active MRE models (Bingham, Bouc-Wen, Modified Bouc-Wen, Dahl and hysteresis); all models are simulated to study the influence of the applied current on its damping forces and rheological properties of MRE in terms of stiffness and damping coefficient. In this section, all analytical simulations for different MRE models in base isolation will be presented starting from the displacement-time response followed by the stiffness and damping coefficient calculations for each model. After that, transmissibility curves analysis is shown in order to investigate and observe the behavior of various models of MRE.

3.1.3.1 Time domain response of base isolation for different MRE models

Simulations were run and all values of the parameters of the hysteresis semi-active MRE models were calculated at different values of current. These parameters which are field-dependent are mathematically expressed in the previous section, some of these parameters are linearly related to the current but some of them are not. All of

48

these data are represented in Table 5. MATLAB codes are shown in Appendix A.

Table 5. Parameters Values for each MRE Model for an Applied Current of 0 A - 4 A.

Model	Parameter	Current applied (i)				
		0 A	1 A	2 A	3 A	4 A
Bingham	f_c	13.52	161.02	308.52	456.02	603.52
	f_0	38.14	-356.66	-751.46	-1146.26	-1541.06
	c_0	52.19	715.75	1379.31	2042.87	2706.43
	k_0	469	792.2	1115.4	1438.6	1761.8
BW	c_0	2100	2450	2800	3150	3500
	α	14000	83500	153000	222500	292000
	A	301				
	β	36300				
	γ	190				
	n	2				
MBW	k_0	500	515.9	531.8	547.7	563.6
	k_1	469	792.2	1115.4	1438.6	1761.8
	c_0	2100	2450	2800	3150	3500
	c_1	28300	28595	28890	29185	29480
	α	14000	83500	153000	222500	292000
	A	301				
	β	36300				
	γ	190				
	n	2				
Dahl	k_0	800	3320	5840	8360	10880
	c_0	24.64	65.05	105.46	145.87	186.28
	δ	0.031	1.151	2.271	3.391	4.511
	ρ	25				
	f_0	0.01				
Hysteresis	k_0	246.7	277.9	309.1	340.3	371.5
	c_0	315.9	347.1	378.3	409.5	440.7
	α	17653	17654.55	17656.11	17657.66	17659.21
	β	25				
	F_0	0				

All of these models are simulated and their displacements with respect to time plots are obtained. The input signals that excite the base are a step and sinusoidal wave as shown earlier. From the analytical simulations of these MRE models for semi-active base isolation system, it is vivid that as the current value increases, the damping and stiffness characteristics of MRE are enhanced and vibration is reduced.

Results of displacement with respect to time are shown for each model with the two different excitations to the base. Results shows that controlling the current from 0 A to 4 A significantly influences the behavior of MRE, a current of 0 A means that the damping force of MRE depends on the passive stiffness and damping. Results illustrate the response of the damped vibration system and the free vibration system for two excitation inputs; step and sine wave.

Simulation results for the five semi-active MRE base isolation models for two excitation inputs are shown in Figures (35-45), it can be clearly seen from the step input response that the damping is enhanced and more efficient as the current increases. The mass is stabilized in a shorter time and the magnitude of the displacement is reduced. In addition, it can be concluded that for the sinusoidal responses that the displacement is reduced as the current is higher. From the step responses, when the current applied increases, the increase in the stiffness and damping properties of MRE is clear as the displacement is reduced and the settling time decreases which means that the signal is reaching steady state faster. For example, this can be shown in as a 'zoomed out' snapshot of the step response of Bingham model (Figure 35).
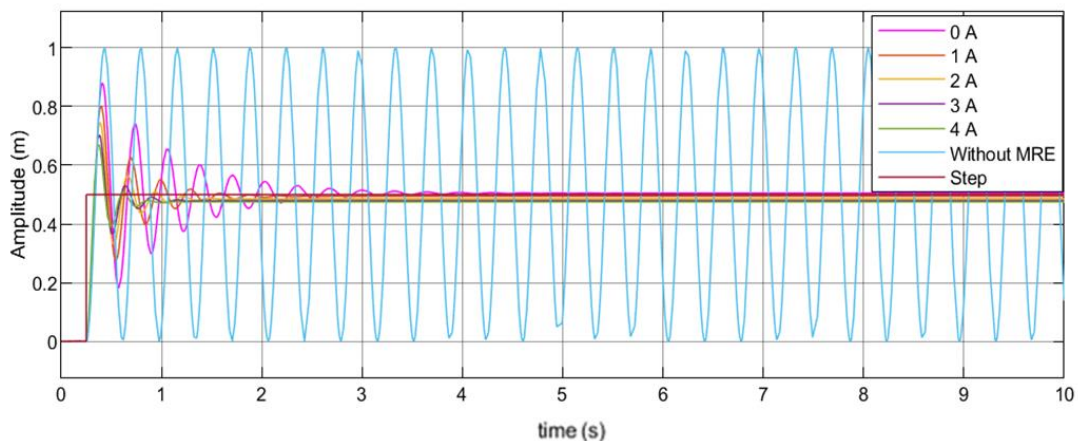
Figure 35. Amplitude vs time for step input (Bingham Model).
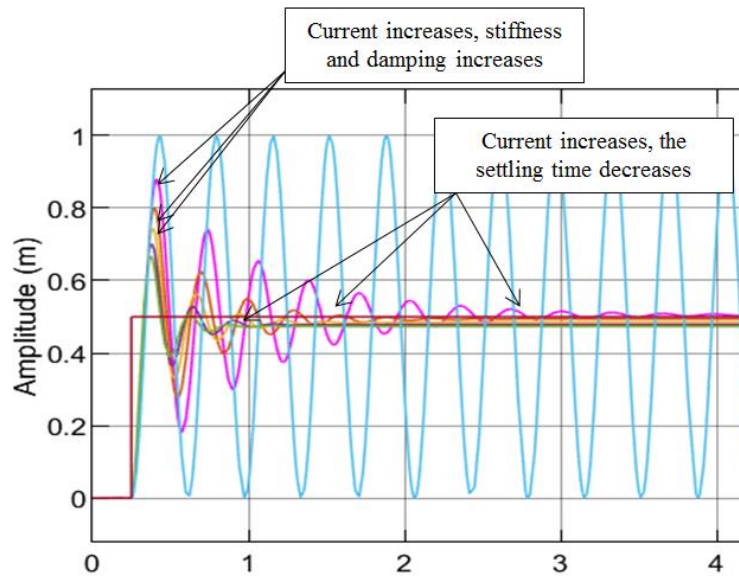
Figure 36. Zoomed out snapshot of Figure 35.
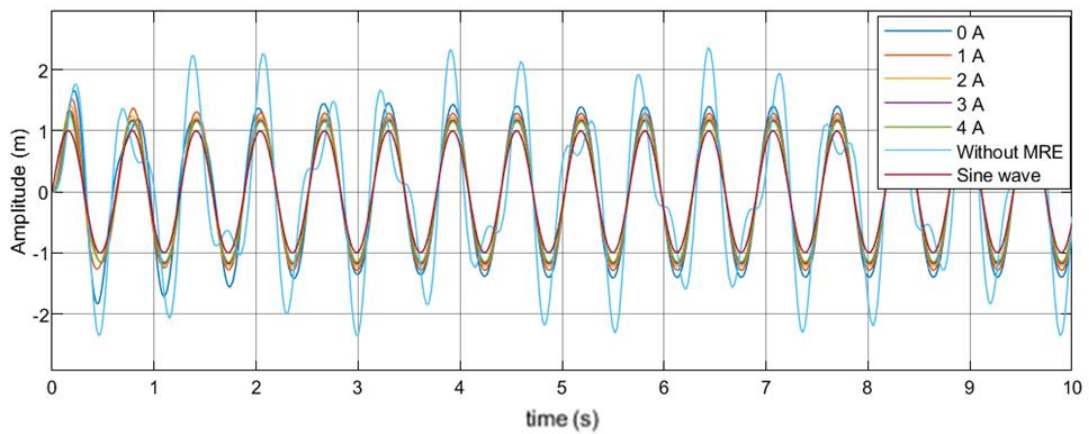
Figure 37. Amplitude vs time for sinusoidal input (Bingham Model).
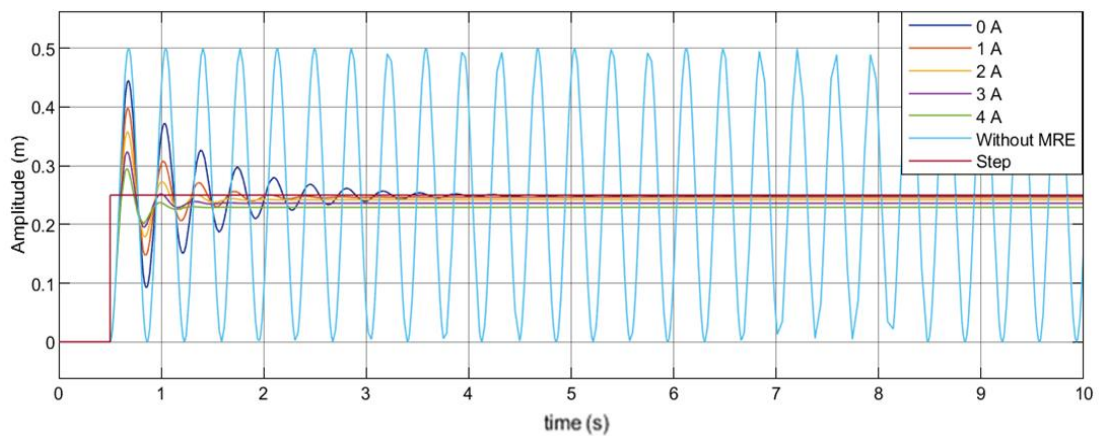
Figure 38. Amplitude vs time for step input (Bouc-Wen Model).

51
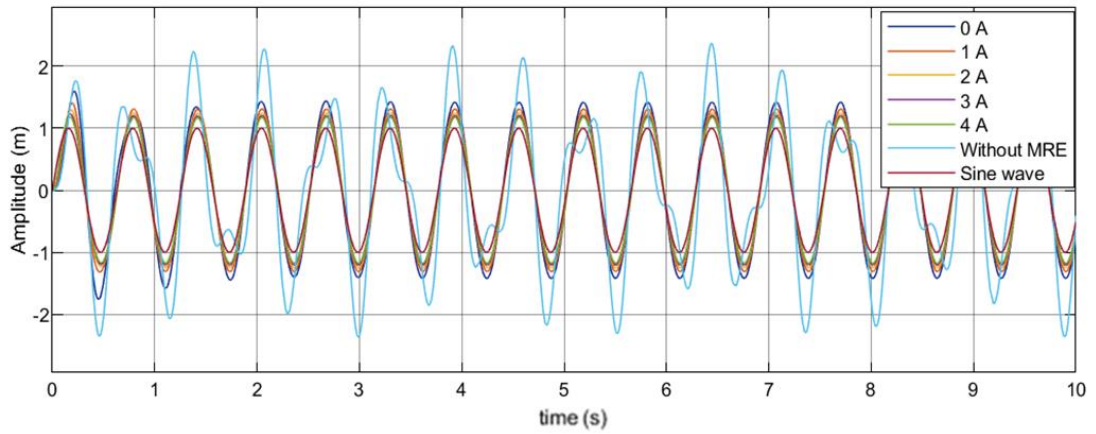
Figure 39. Amplitude vs time for sinusoidal input (Bouc-Wen Model).
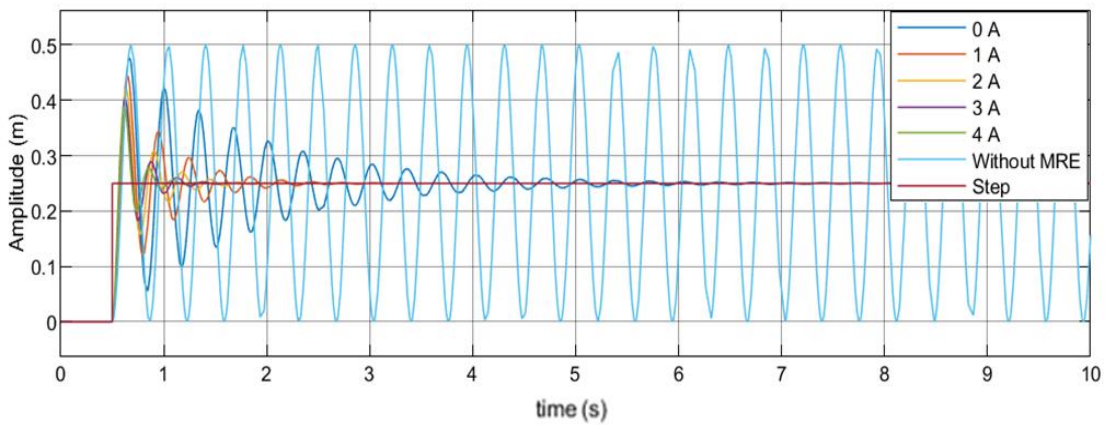
Figure 40. Amplitude vs time for step input (MBW Model).
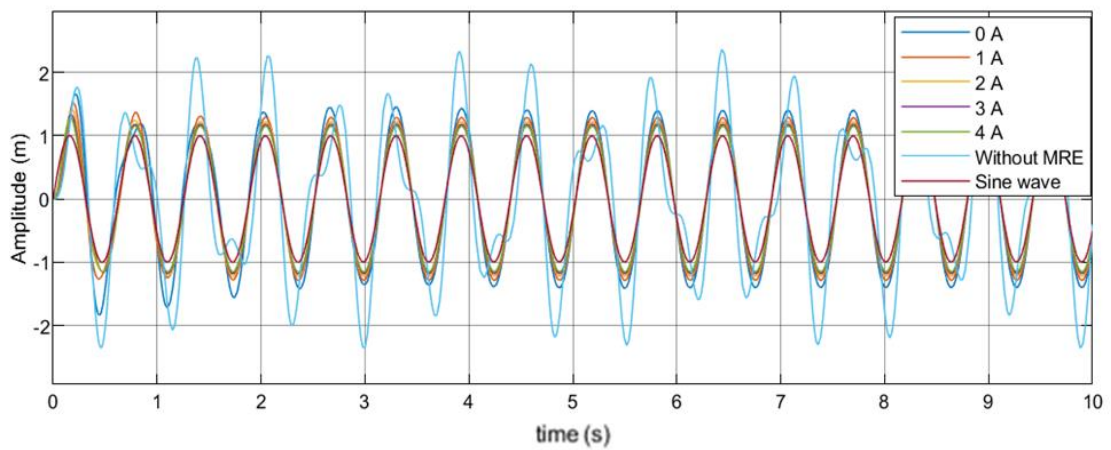
Figure 41. Amplitude vs time for sinusoidal input (MBW Model).
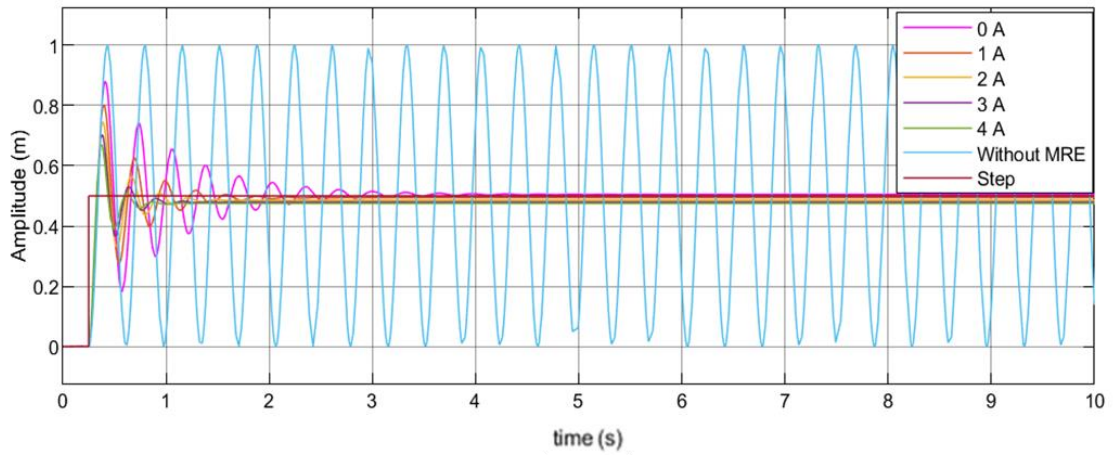
Figure 42. Amplitude vs time for step input (Dahl model).
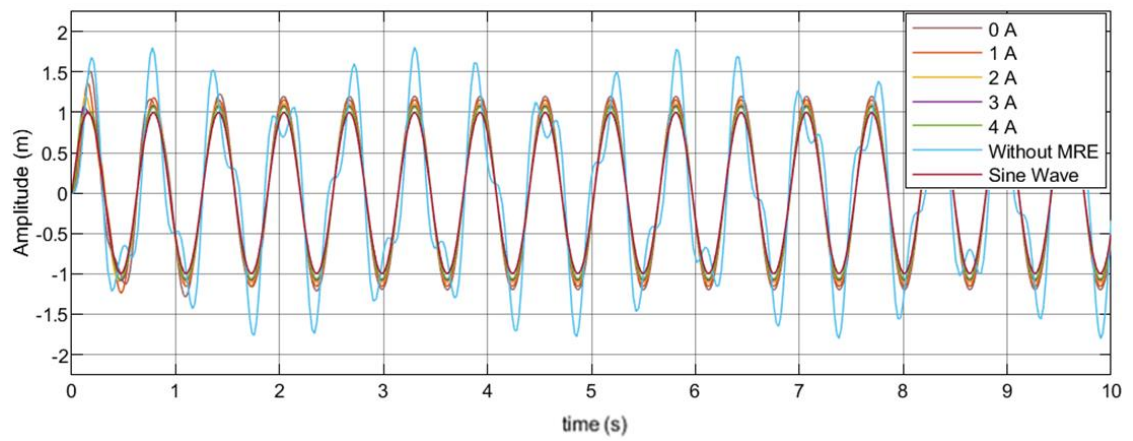
Figure 43. Amplitude vs time for sinusoidal input (Dahl Model).
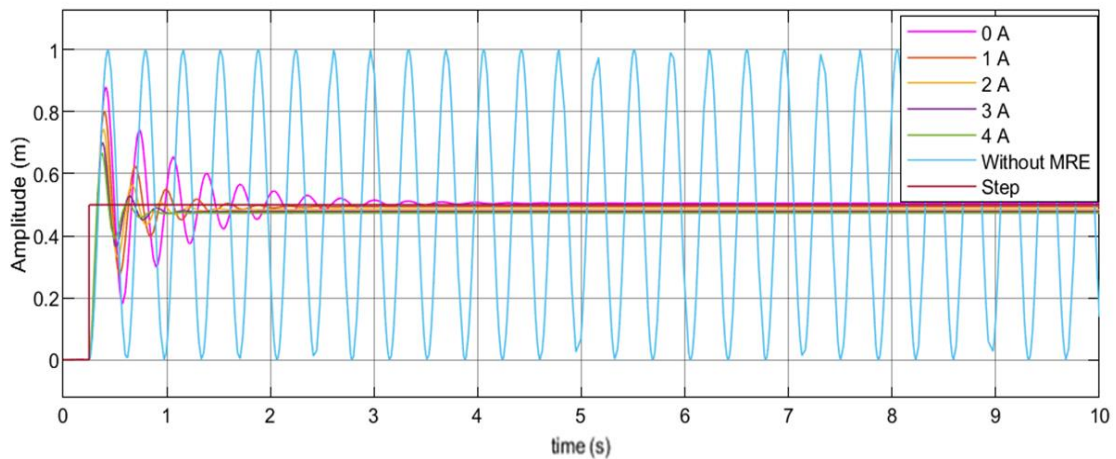
Figure 44. Amplitude vs time for step input (Hysteresis Model).
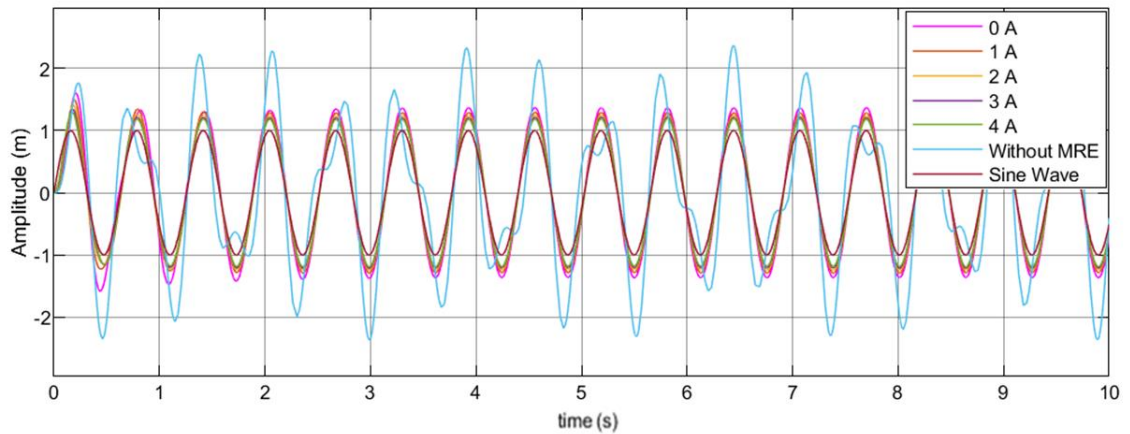
Figure 45. Amplitude vs time for sinusoidal input (Hysteresis Model).

To compare the damping characteristics of all models, Table 6 shows some parameters calculated by MATLAB software using property editor on figures such as $\%PO$, Tp and Ts which were discussed in Section 3.1.2.1.

For Bingham model, the $\%PO$ values are reduced as the current increases. For example, the $\%PO$ values are 44.922% and 39.472% when the applied current values are 0 A and 1 A, respectively. This shows that the displacement amplitude is being reduced. In addition, Tp is reduced in each iteration which means that the time needed to achieve the peak displacement is decreasing; this illustrate that the response tends to shifted and the natural frequency of the system is increasing. This shift in the natural frequency is a sign that the vibration is being reduced with the current. To prove this, the settling time for all iterations was calculated and shown in Table 6. The settling time is reduced from 2.959 s to 1.281 s as the current increases from 0 A to 4 A. This means that the time needed for the oscillation to achieve $\pm 2\%$ steady-state value. Therefore, the vibration is reduced and the steady-state value is achieved in lesser time.

This conclusion is shown clearly for all other four models (BW, MBW, Dahl and hysteresis). Vibration is reduced as the MRE is exposed to more current; more

54

magnetic field. BW model showed a reduction in the %PO from 69.378% to 33.654% as the current increases from 0 A to 4 A. Tp and Ts are reduced as well meaning that the natural frequency is being increased and the vibration reduction is greater. Similarly to MBW, Dahl and Hysteresis semi-active MRE models. The mass of the system is constant which is assumed to be 5 kg. All other models parameters are changeable and depend on the current. In terms of Ts, the lowest time needed for the oscillations to be steady for the passive stiffness and damping (0 A current) is 0.676 s for Dahl model, and it kept decreasing as the current increases. This shows that vibration reduction is superior for this model other than other models. In contrast, the maximum value for Ts for the passive MRE properties is shown in MBW model (4.682 s and kept decreasing). This means that the underdamped oscillation took much time in reaching the steady-state value. This is due to the complexity of MBW model as it includes 14 parameters that control its hysteresis loop.

Table 6 . %PO, Tp and Ts Results for all Models.

Current	Bingham model			BW model			MBW model			Dahl model			Hysteresis model		
	PO	*Tp*	*Ts*	*PO*	*Tp*	*Ts*	*PO*	*Tp*	*Ts*	*PO*	*Tp*	*Ts*	*PO*	*Tp*	*Ts*
[A]	%	[s]	[s]	%	[s]	[s]	%	[s]	[s]	%	[s]	[s]	%	[s]	[s]
0	44.922	0.592	2.959	68.378	0.971	1.091	66.020	0.486	4.682	41.723	0.537	0.676	41.602	0.628	0.791
1	39.472	0.518	2.229	53.489	0.771	0.716	63.941	0.300	2.682	38.224	0.385	0.472	38.150	0.451	0.552
2	34.240	0.479	1.788	44.789	0.732	0.548	63.829	0.245	2.179	34.768	0.319	0.380	34.727	0.373	0.445
3	31.334	0.433	1.493	40.018	0.714	0.426	59.771	0.225	1.748	31.457	0.281	0.325	31.420	0.329	0.380
4	26.663	0.423	1.281	33.654	0.691	0.378	49.297	0.198	1.119	28.309	0.255	0.287	28.284	0.299	0.335

3.1.3.2 Stiffness, damping and transmissibility curves for different MRE models

After obtaining the displacement response in the time domain for the each MRE model for base isolation system, the transmissibility curve can be plotted. The methodology of obtaining the transmissibility curves is discussed in Section 3.1.2.1. Reconsidering the transfer function that relates the output displacement $x(t)$ to the input base excitation $x(t)$ Eq. (27)

$$T = \left|\frac{X(\omega)}{Y(\omega)}\right| = \sqrt{\frac{(c\omega)^2 + k^2}{(c\omega)^2 + (k - m\omega^2)^2}}$$

Stiffness and damping coefficient values are calculated from the step response plots for all MRE models. Knowing that $\%PO$ is related to the damping ratio, ζ and peak time, Tp, is related to the natural frequency, ω_n. Therefore, by following this methodology, results are shown in for each model in Table 7. It can be seen that the stiffness and damping coefficient of MRE are increasing by increasing the applied current. The passive stiffness for each model is different based on its mathematical expressions as well as the field-dependent equations. All MATLAB codes used in these calculations are presented in Appendix A.

Table 7. Results for c and k Calculations.

Current	PO	Tp	ζ	ω_n	k	c_c	c
[A]	%	[s]	[1]	[rad/s]	[N/m]	[1]	[N.s/m]
Bingham model							
0	44.92	0.59	0.25	5.48	150	54.77	13.52
1	39.47	0.52	0.28	6.32	200	63.25	17.945
2	34.24	0.48	0.32	6.93	240	69.28	22.37
3	31.33	0.43	0.35	7.73	299	77.33	26.795
4	26.66	0.42	0.39	8.05	324	80.50	31.22
BW							
0	68.38	0.97	0.75	4.89	119.54	48.90	47
1	53.49	0.77	0.81	6.91	239.08	69.15	67
2	44.79	0.73	0.86	8.47	358.62	84.69	73

Current	*PO*	*Tp*	*ζ*	*ω_n*	*k*	*c_c*	*c*
[A]	%	[s]	[1]	[rad/s]	[N/m]	[1]	[N.s/m]
3	40.02	0.71	0.96	9.78	478.16	97.79	79
4	33.65	0.69	0.97	10.93	597.7	109.33	82
MBW							
0	66.02	0.49	0.13	6.52	212.32	65.16	14.32
1	63.94	0.30	0.14	10.58	559.52	105.78	17.11
2	63.83	0.24	0.14	12.97	841.32	129.72	18.29
3	59.77	0.23	0.16	14.14	1000.3	141.44	20.02
4	49.30	0.20	0.22	16.26	1322.46	162.63	21.32
Dahl							
0	41.72	0.54	0.71	8.32	346	83.19	59.15
1	38.22	0.39	0.72	11.76	692	117.64	84.76
2	34.77	0.32	0.73	14.41	1038	144.08	105.23
3	31.46	0.28	0.74	16.64	1384	166.37	123.16
4	28.31	0.26	0.75	18.60	1730	186.01	139.55
Hysteresis							
0	41.60	0.63	0.71	7.11	252.90	71.12	50.59
1	38.15	0.45	0.72	10.06	505.70	100.57	72.48
2	34.73	0.37	0.73	12.32	758.60	123.17	89.98
3	31.42	0.33	0.74	14.22	1011.40	142.23	105.30
4	28.28	0.30	0.75	15.90	1264.30	159.02	119.31

Stiffness and damping coefficients values are plotted with respect to the applied current using 'subplot' command in MATLAB as shown in Figures (46, 47). It can be clearly seen from Figure 46 that the stiffness of the MRE for all models increases significantly when the current is increased. For example, the stiffness increases from 150 N/m to 200 N/m at an applied current 0 A to 1 A, respectively. This shows a 33.3% increase in the stiffness when the current is applied initially. In contrast, the damping coefficient increases from 13.5 N.s/m to 17.945 N.s/m and an applied current 0 A to 1 A, respectively as shown in Figure 47. This shows a 26.82% increase in the damping coefficient. For BW model, the stiffness increases by 78% when 1 A current is applied, an increase of 42.6% is obtained. The stiffness shows an increase of 63.5%, 78% and 90% for MBW, Dahl and Hysteresis models, respectively whereas the damping coefficient increased by a percent of 19.5%, 42.3% and 43.3%,

respectively. In addition, the range of the stiffness values is more than the range of the damping coefficient values. For example, the minimum and maximum values of stiffness for MBW model are 212.32 N/m and 1322.46 N/m whereas damping coefficient values are 14.32 N.m/s and 21.32 N.m/s, respectively. This can be seen for all other models as well. Therefore, an increase in the stiffness and damping coefficient is noted when the current is increased. However, the change in the stiffness of the MRE compared to significant. This proves the theory mentioned in the literature by which the stiffness of the MRE varies significantly with the magnetic field whereas the damping characteristics do not. Although the change in the damping in these simulations still considerable but when it compared with the stiffness variation, it can be concluded that the MRE stiffness properties varies more significantly than damping. One reason for the considerable change is that the equations relating the model parameters might have some magnetorheological fluids (MRF) characteristics. The damping behavior of MRF is significant with a magnetic field unlike MRE.
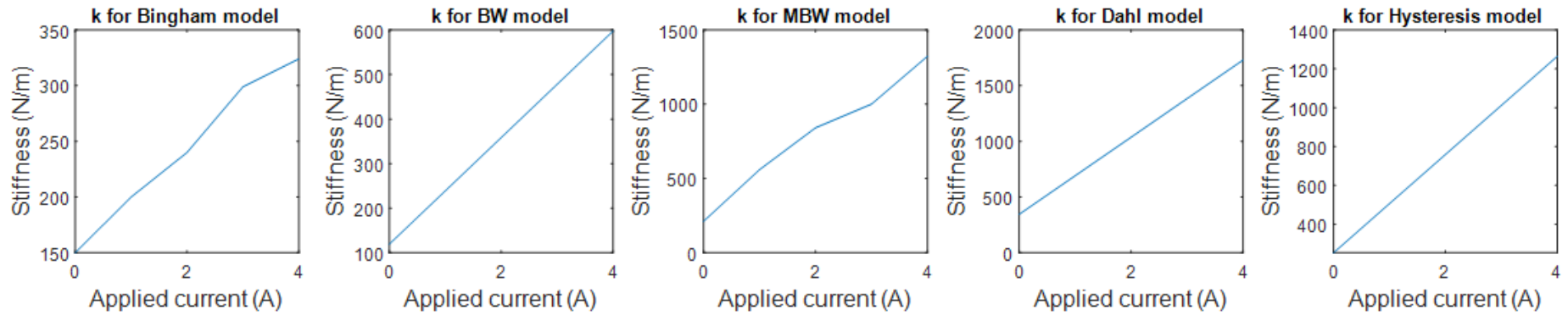
Figure 46. Stiffness values for each MRE model with respect to the applied current.
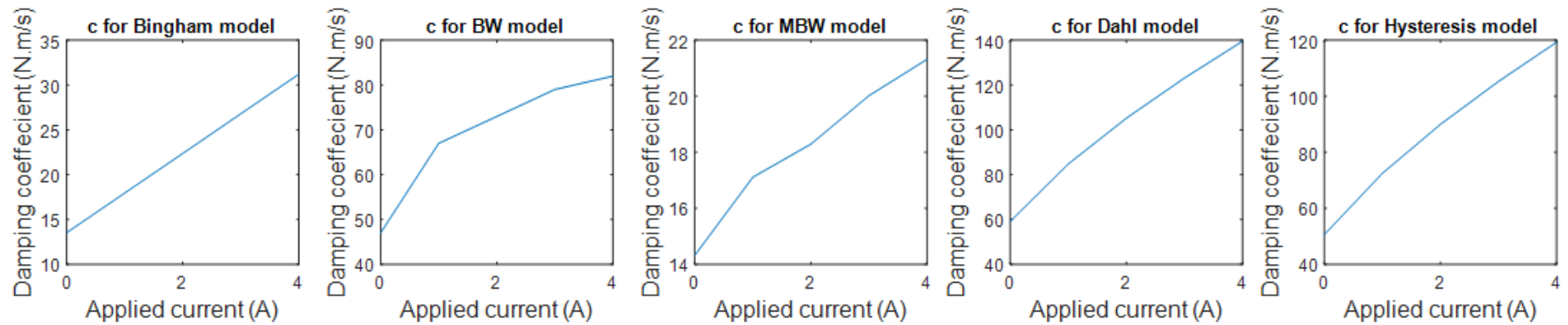
Figure 47. Damping coeffecient values for each MRE model with respect to the applied current.

59

After obtaining c and k values for each MRE model, the transmissibility factor is plotted with respect to the frequency for each model at different current. The range of the frequency for this simulation was set to be 0 H to 100 Hz. It can be clearly seen from Figure 48 that the natural frequency of the system is increased and the transmissibility curve is shifted to the right. This clearly shows that the curve is being shifted towards the reduction region which means that the vibration is isolated. This shift in the transmissibility curve is evidence showing that the stiffness of the MRE is increased when the applied current increases. In addition, the amplitude is being reduced which means that the damping ratio is increased so that the system is damped better so the vibration is isolated faster. However, as concluded earlier that the change in the damping properties is slighter than the change in the stiffness of the MRE. The transmissibility curve for Bingham model is shifted in a small increment as shown in Figure 48 (a). The variation in the stiffness values are minimum, this due to the simplicity of this model as it has only three parameters related to the current. MBW (Figure 48 (c)) and Dahl (Figure 48 (d)) models show more shifting the transmissibility curve as the applied current increases. This due to the more accurate approximation of the field-dependent parameters that control the hysteresis loops.
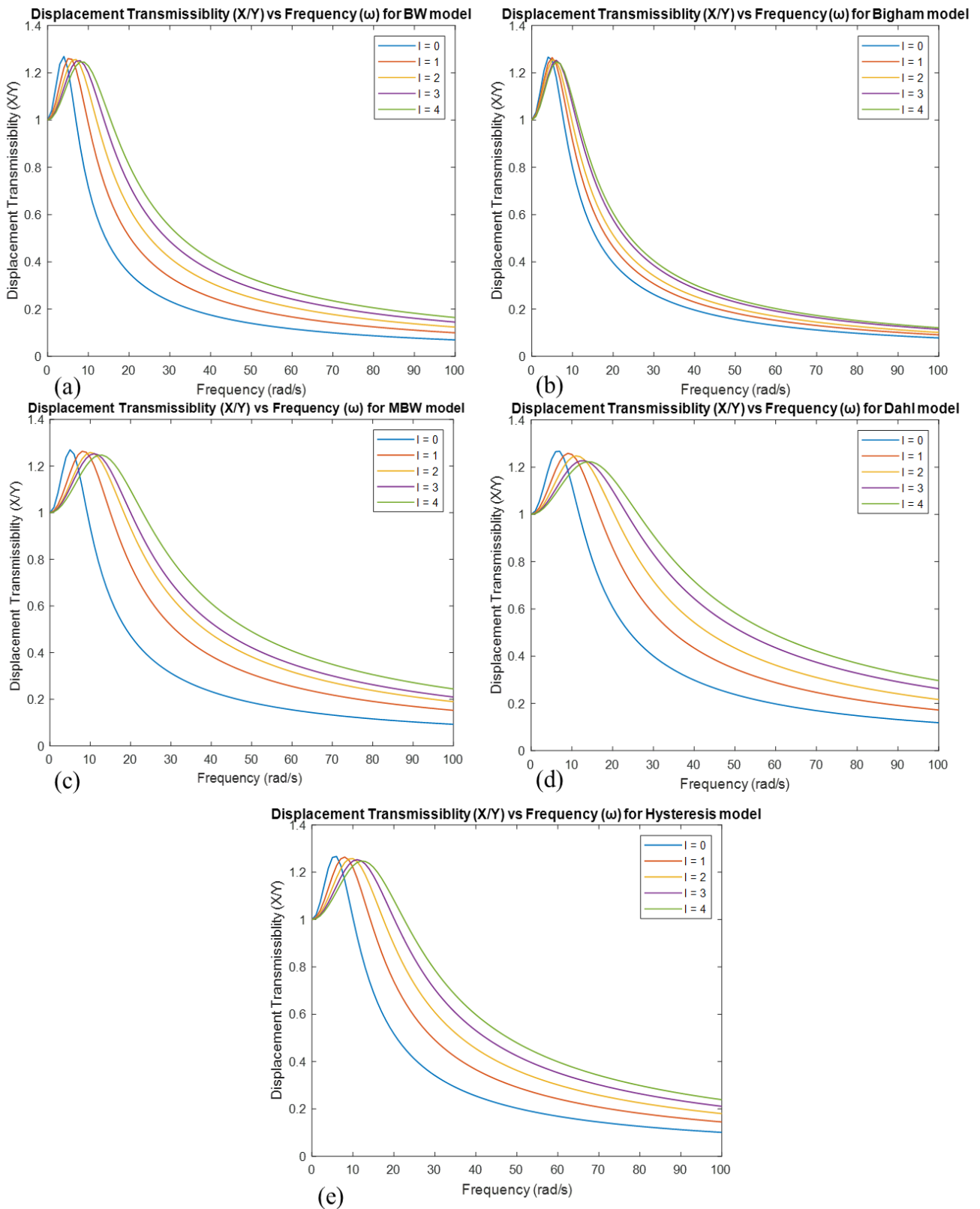
Figure 48. Dsiplacement transmissiblity vs frequency for (a) Bingham model, (b) Bouc-Wem model, (c) Modified Bouc-Wen model, (d) Dahl model, and (e) Hysteresis model.

3.2 Numerical modeling of MRE using COMSOL Multiphysics software

In this section, a 3D numerical modeling and analysis of MRE is done. A magnetic-mechanical coupled physics is done for MRE using COMSOL 5.4 multi-physics finite element analysis (FEA) software. This is to investigate and study the behavior of MRE in 3D using a numerical method. A cylindrical silicon elastomer is embedded with magnetic particles. In addition, the geometry is modeled in the micro-scale in order to visualize the behavior of MRE under magnetic field. The stiffness of MRE in linear (axial) and torsional modes is studied under the influence of the magnetic field. Also, the transmissibility analysis is done in order to observe the field-stiffening characteristics. This study is done by COMSOL Multiphysics software which is cross-platform FEA multiphysics and solver simulation software which allows conventional physics-based user interfaces and coupled systems of partial differential equations (PDEs).

3.2.1 Numerical model of MRE

3D model of MRE is developed and modelled and it is consisting of two main regions: a MRE and the surrounding air region. The MRE model is a cylinder which is a pure silicon rubber and 12 iron particles (spheres) which are distributed in an anisotropic orientation. The cylindrical silicon rubber has a diameter of 20 µm and a height of 30 µm. The iron particles are spheres with 4 µm in diameter for each. The geometry of the modelled MRE and its dimensions are illustrated in Figures (49, 50).
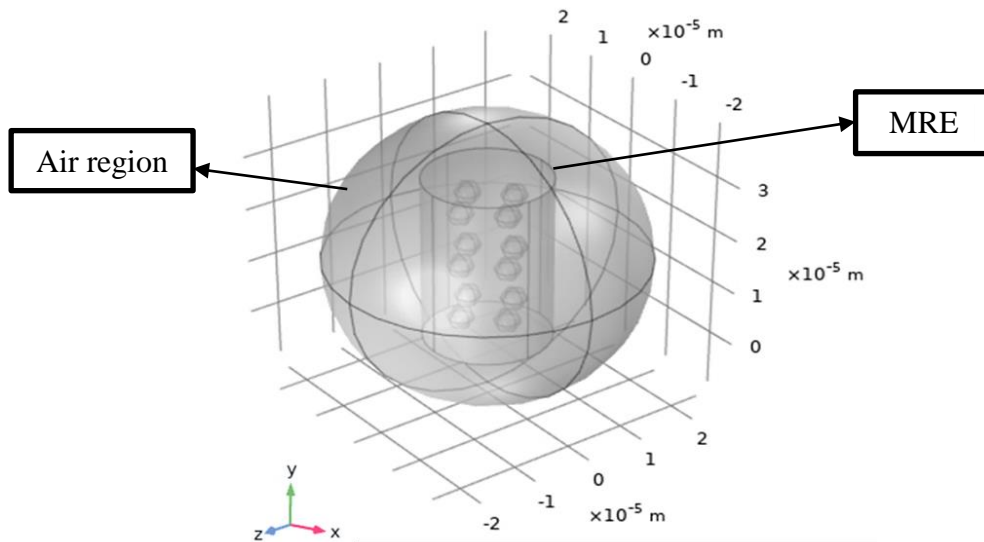
Figure 49. MRE 3D model.
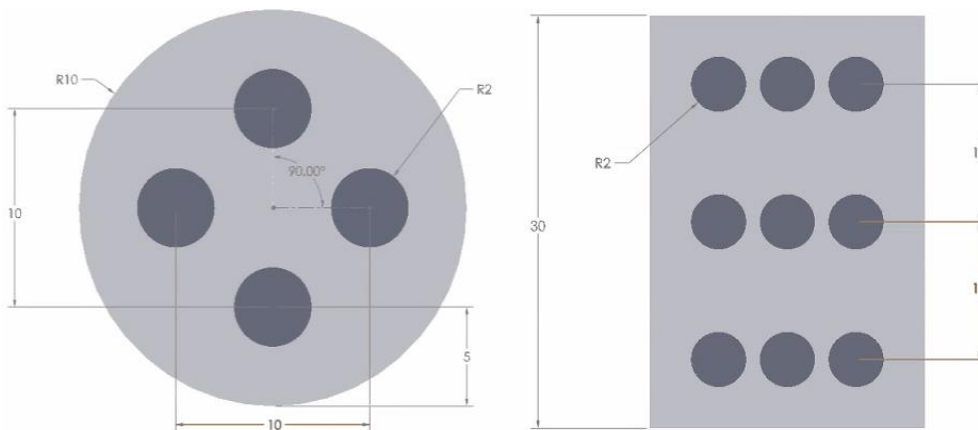
Figure 50. Dimensions of the MRE model used in the simulation study.

The mechanical and magnetic properties of the MRE are chosen from literature studies [80-82]. For the MRE, silicon rubber is imported from COMSOL library to be the polymer matrix and the particles are set to be "iron powder vetroferrit" due to good magnetic behavior and the high permeability. The properties for the MRE for the analysis are obtained where Young's modulus is defined for both the rubber and the magnetic particles. The material properties used for this simulation study are shown in Table 8.

Table 8. Materials Properties of the MRE [80-82].

Silicon	Density ρ [**kg/m³**]	1100
	Relative permeability μ_{Si}	2
	Relative permittivity ε_r	4
	Young's modulus E [MPa]	0.12
	Poisson's ratio v	0.31
	Dynamic viscosity μ [kg/ms]	0.00086
Iron powder vetroferrit	Young's modulus E [MPa]	200000
	Poisson's ratio v	0.33
Air	Relative permeability μ_{air}	1

For the iron magnetic particles, the H-B curve for this material (Iron powder vetroferrit) is obtained from COMSOL materials library [90] and it is shown in Figure 51.
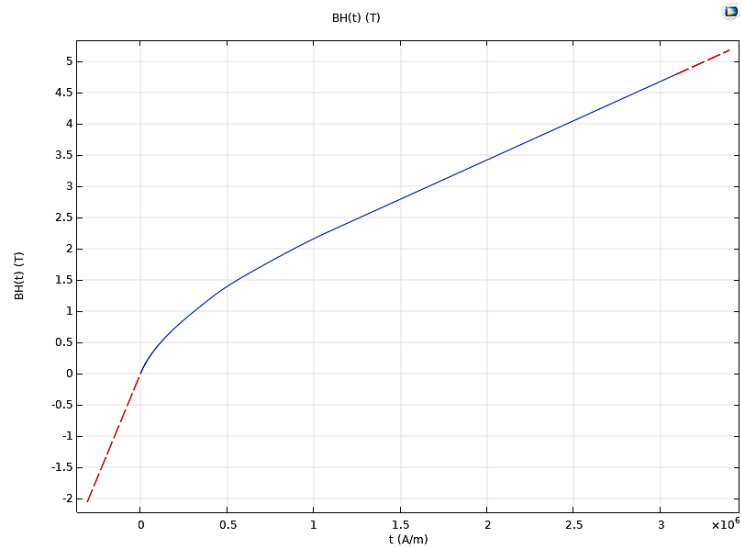
Figure 51. B-H diagram for the iron particles.

Since torque is applied on the MRE to get it is torsional stiffness properties; the shear modulus should be known. An equation for the shear modulus G of a rubber that is filled with particles as follows [91]

$$G = G_0(1 + 2.5\emptyset + 14.1\emptyset^2) \tag{52}$$

where G_0 is the shear modulus of pure silicon rubber ($G_{Si} = 50.9 \ GPa$) [32] and $\emptyset$ is the volume fraction of particles relative to the rubber matrix and it can be expressed in this case by

$$\emptyset = \frac{\frac{4}{3}\pi r^3 n}{\pi R^2 h} \tag{53}$$

Where r is the radius of the particles, n is the number of particles, R is the radius of the rubber cylinder and h is the height of the rubber cylinder. The volume fraction of the model is 37.5% and hence, the shear modulus for MRE is 57.7 GPa.

3.2.2 Governing equations

The continuum-mechanics approach is used to analyze the MRE by which the mechanical deformation equations are coupled with electromagnetic equations. A set of partial differential equations are solved using COMSOL. In this case, it is assumed that an external force per unit area F is applied at the top surface of MRE for the linear analysis, by applying Newton's 1st law of motion, the stress distribution within the cylinder in as follow in tensor notation

$$-\nabla.\sigma = F \tag{54}$$

The generalized Hooke's law

$$\sigma = E\varepsilon \tag{55}$$

where σ is linear Cauchy stress tensor, E is the modulus of elasticity. But Hooke's law for springs, the linear stiffness

$$F = k_l y \tag{56}$$

where F is the force, k_l is the linear stiffness and y is the deformation in y-axis. The tensor notation of linear strain displacement

$$\varepsilon = \frac{1}{2}[(\nabla y)^T + \nabla y] \tag{57}$$

Substituting Eqs. (54-56) into Eq. (57), the governing equation becomes

$$k_l y + \nabla.\left[E\left\{\frac{1}{2}\{(\nabla y)^T + \nabla y\}\right\}\right] = 0 \tag{58}$$

Similarly for the torsional analysis, Hooke's law becomes

$$\tau = G\gamma \tag{59}$$

where τ is the torsional stress tensor, G is the shear modulus and γ is the torsional strain. The torsional stiffness of MRE for can be obtained from

$$T = k_t\theta \tag{60}$$

where T is torque applied, k_t is the torsional stiffness, and θ is the rotation. Therefore, the governing equation for the torsional analysis becomes

$$k_t\theta + \nabla.\left[G\left\{\frac{1}{2}\{(\nabla\theta)^T + \nabla\theta\}\right\}\right] = 0 \tag{61}$$

The previous sets of equations solve the solid structure aspect for the magneto-mechanical problem. The following equations solve for the "external magnetic field interface with no current"

$$\nabla.(\mu_0\mu_r H) = 0 \tag{62}$$

$$H = -\nabla V_m + H_b \tag{63}$$

$$H = -\nabla V_m \tag{64}$$

where μ_0 is the relative permeability of the material, $\mu_r = 4\pi \times 10^{-7} N/A^2$ is the permeability of free space, H is the magnetic field, H_b is the background magnetic field and V_m is the magnetic potential vector. For each material; silicon rubber, particles and air, there is a different $B - H$ relationships based on the relative permeability. The general constitutive relation for the magnetic behaviour of air medium is

$$B = \mu_0 \mu_r H \tag{65}$$

where B is the magnetic flux intensity. The general constitutive equation for the iron particles (magnetic material) is given by

$$B = \mu_0 (H + M) \tag{66}$$

where M is the magnetization. The magnetostriction physics equation becomes

$$-\nabla.(\mu_0 \nabla V_m - \mu_0 M) = 0 \tag{67}$$

After that, the frequency domain analysis is done to get the linear amplitude transmissibility (y_2/y_1), the input y_1 is applied as a displacement, to get output displacement response y_2 expressed by

$$y_1 = Y_1 e^{j\omega t} \tag{68}$$

$$y_2 = Y_2 e^{j\omega t} \tag{69}$$

where y_1 is the input harmonic displacement, Y_1 is the amplitude, y_2 is the harmonic displacement response, Y_2 is the response amplitude, i or j is imaginary number, t is the time, ω is the angular frequency [rad/s]. The linear amplitude transmissibility (y_2/y_1) is plotted with respect to the excitation frequencies. Similarly, for the torsional transmissibility (θ_2/θ_1), the equations becomes

$$\theta_1 = \vartheta_1 e^{j\omega t} \tag{70}$$

$$\theta_2 = \vartheta_2 e^{j\omega t} \tag{71}$$

where θ_1 is the input harmonic rotation, ϑ_1 is the rotational input amplitude, θ_2 is the harmonic displacement response, ϑ_2 is the rotational response amplitude. The Eigen frequency study is done in order to obtain the 1st natural frequency of the system which expressed by:-

$$f = -\frac{\lambda}{2\pi i} \tag{72}$$

where λ is the eigenvalue.

3.2.3 COMSOL Multi-physics simulation

This multi-physics simulation is to study the mechanical behavior of the MRE in the presence of a magnetic field. Such analysis is to study the variation in stiffness due to the magnetic field and its effect on transmissibility curve for both linear and torsional vibration. The magneto-elastic coupled interface simulation using Solid structure and magnetic field physics was done. These two physics can be shown in Figure 52.
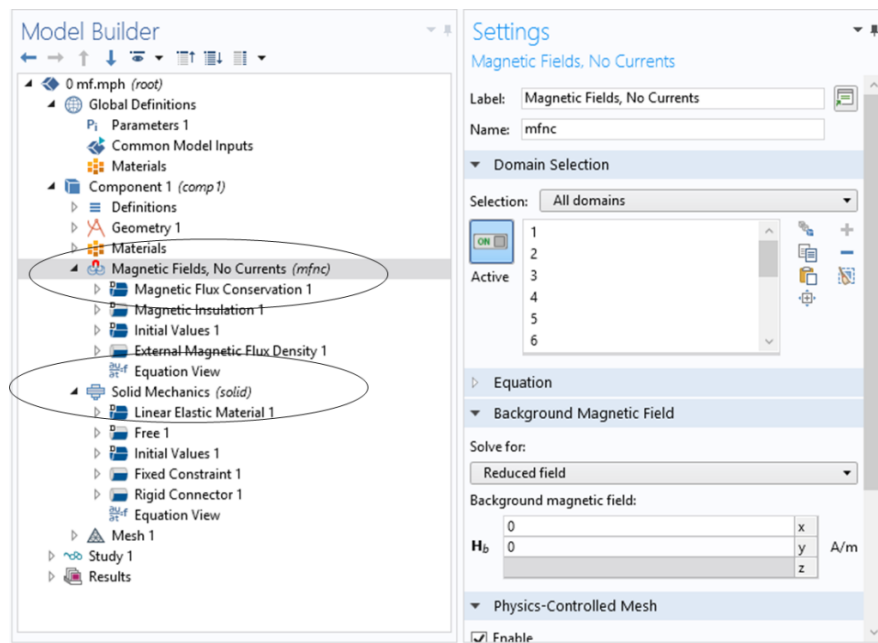
Figure 52. Magneto-mechanical coupled interface on COMSOL.

This study is divided into two parts; the 1st part is to obtain the stiffness of the system in linear and torsional modes, by which a fixed load/torque is applied on the top surface of the MRE, and then obtaining the deformation/rotation of the system under various magnetic fields and then calculating the linear/torsional stiffness using Eqs. (56-60). The 2nd part of the analysis is to obtain the transmissibility curve with respect to the frequency using a harmonic study under different magnetic fields. The resonance frequencies are obtained using the Eigen frequency study, and then the

harmonic study is done for a range of frequency covering the fundamental natural frequency of the system for linear and torsional cases.

3.2.3.1 Methodology and Boundary conditions

3.2.3.1.1 Methodology and boundary conditions for stiffness analysis

In this subsection, the mechanical boundary conditions in 2D and 3D of the system are represented in Figure 53. The upper top surface of the MRE has a boundary load; a force F in the -y-axis as in Figure 53 (a) for the linear analysis and a torque T using a rigid connector (counter clockwise) around + y-axis. On the other hand, the lower bottom surface is fixed. This is done to calculate the stiffness of the system after obtaining the deformation/rotation at different values of magnetic field using Eqs. (56, 60). The values of loads are constant in each iteration. A parametric sweep is done for the magnetic field strength from 0 A/m − 7 A/m with a step of 1 A/m. For each value, the deformation/rotation is noted to be analysed.

(a)　　　　　　(b)
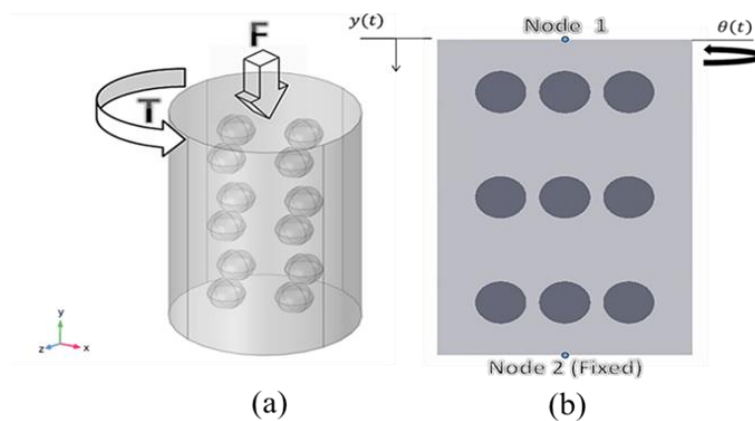
Figure 53. Methodology and boundary conditions representation for 1ˢᵗ part in (a) 3D, and (b) 2D.

Figure 53 (a) represents the boundary loads for both linear and torsional load on the top surface of the MRE in 3D while Figure 53 (b) illustrates the boundary

conditions in 2D. Assuming two nodes in each side of MRE; node 1 and node 2, the boundary conditions for the linear analysis can be represented by the displacement applied in a function of force applied $y_1 = f(F)$ and $y_2 = 0$ where y is the displacement (deflection) in -y-direction and the linear load is $F = -0.005\,N$. Similarly, for torsional analysis the rotation applied as a function of the torque $\theta_1 = f(T)$ and $\theta_2 = 0$ where θ the rotation around y-axis and the torque applied is $T = 0.005\,N.m$. However, the displacement/rotation will depend also on the magnetic field applied B. Therefore, $y_1 = f(F,B)$ and $\theta_1 = f(T,B)$.

The boundary loads (force and torque) are illustrated on COMSOL. The boundary load represents the force applied on the upper surface (node 1) while fixing the lower surface. Similarly, the torque was applied on the upper surface using a rigid connector. These boundary conditions are shown from COMSOL in Figure 54.

(a)

(b)
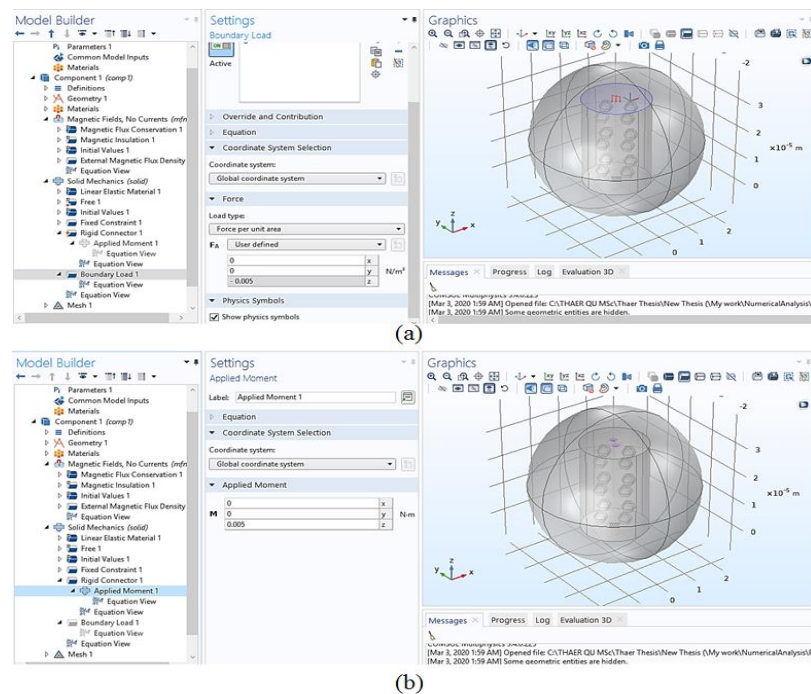
Figure 54. Boundary conditions on COMSOL; (a) linear (axial) load, and (b) torsional load.

3.2.3.1.2 Methodology and boundary conditions for the transmissibility analysis

In this case, the bottom surface (node 2) of the MRE is free end, so that it can displace/rotate. However, the load/torque applied on the top surface are now harmonic loads at certain range of excitation frequencies; Eqs. (68-71) illustrates the methodology followed by COMSOL to solve the analysis. This methodology is shown in Figure 55 (a) in 3D and Figure 55 (b) in 2D. The analysis is mainly to find the transmitted loads on the bottom surface of the MRE (Node 2). These loads are axial load (linear displacement) to study the linear amplitude transmissibility and torsional load (rotation) to study the torsional amplitude transmissibility.

(a)   (b)
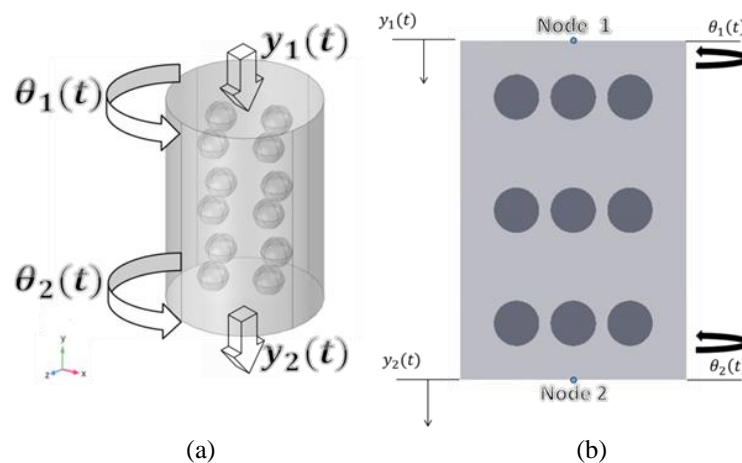
Figure 55. Methodology and boundary conditions representation for the transmissibility analysis in a) 3D and b) 2D.

This approach is similar to the transmissibility of a mass spring damper with base excitation system. The boundary conditions are excitations harmonic loads applied. In case of linear transmissibility, the amplitude $Y_1 = 0.005\ N$ is given as a harmonic input to the system. Similarly, a rotation $\vartheta_1 = 0.35\ rad$. Similar to the previous study, a parametric sweep is done for the magnetic field strength from 0 A/m $-$ 7 A/m with a step of 1 A/m. For each value, the deformation/rotation at node

2 (output) is divided by the input value for the transmissibility curve with respect to the excitation frequencies. The transmissibility obtained in this study is based mainly on the behavior of the stiffness of the MRE as the magnetic field is varied. The frequencies ranges for the harmonic analysis are obtained after conducting an Eigen frequency study by COMSOL using Eq. (72).

3.2.3.2 Meshing

Meshing is done using COMSOL physics-controlled mesh. The element size is set to be extra fine. The total number of elements of the mesh is 349236 elements which is a significant number for a micro-scale model. This can be shown on COMSOL as in Figure 57. 53774 elements are in the iron particles, 118351 elements are in the silicon rubber matrix and 177111 elements are in the air domain sphere. A good mesh quality is identified by some statistical measures. For example, from the mesh statistics, skewness is chosen from the quality measure tab which is defined by the angular measure of the quality of elements, it also illustrates how ideal is a cell or a face [92]. As a rule of thumb, the minimum element value in the skewness statistics is above 0.01 [92]. The value in this mesh is 0.6626. Therefore, it is concluded that the mesh is significant for the study. Meshing for MRE is shown in Figure 56.
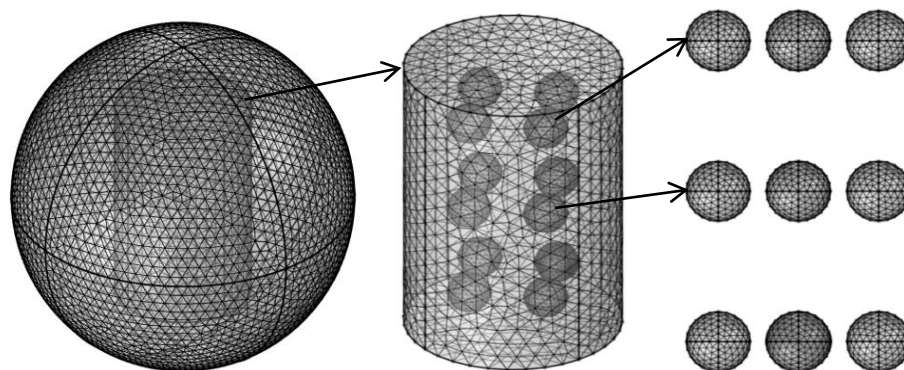
Figure 56. Mesh of the MRE model.
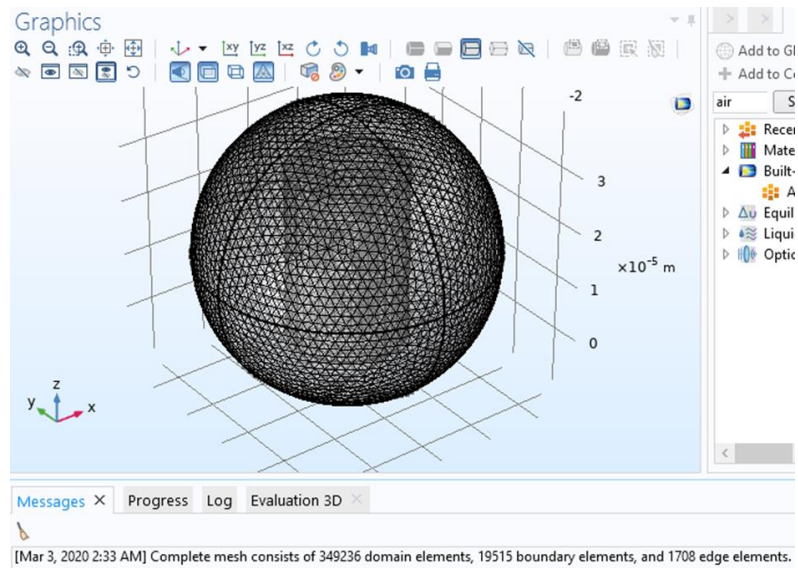
Figure 57. Meshing properties and statistics on COMSOL.

3.2.4 FEA results and discussion

In this analysis, a magneto-mechanical coupling finite element formulation and simulation of MRE is presented using COMSOL. MRE is modeled as cylindrical silicon rubber embedded with 12 spherical magnetic particles (Iron powder vetroferrit), and a sphere around it which considered to be the air domain. Two types of studies are done; the 1st study is to investigate the variation in the linear/torsional stiffness of MRE when an external magnetic field is applied. The 2nd study is to plot the transmissibility curve of both linear and torsional harmonic loads.

Firstly, the magnetic behavior of the particles is identified by a B-H curve which describes the magnetic flux density (B) with respect the magnetic field strength (H). COMSOL identifies the magnetic field strength (H) in A/m and the magnetic flux density (B) in T, the applied magnetic field strength is a sweep from 0 A/m to 7 A/m using "Magnetic fields, no current" physics in COMSOL. However, results are shown in terms of magnetic flux density (B) in mT. This conversion is done using Eqs. (65-67) depending on the materials relative permeability, data are represented in Table 9.

73

Table 9. Magnetic Flux Intensity Calculations.

H[A/m]	0	1	2	3	4	5	6	7
B [mT]	0	0.00125	0.00251	0.00376	0.00502	0.0062	0.00753	0.00879
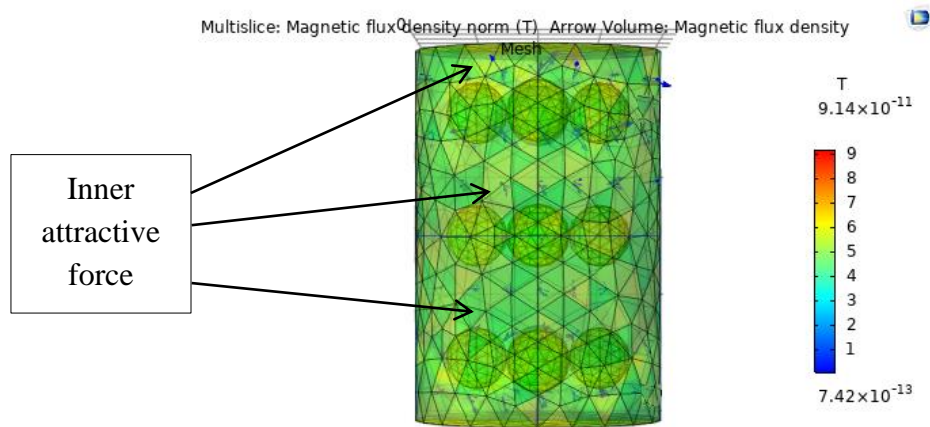
Figure 58. Arrow volume plot showing the inner attractive forces by the magnetic particles.
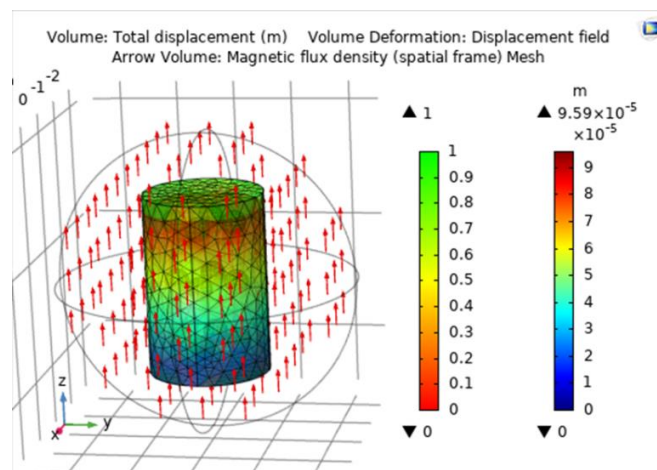
Figure 59. 3D view of the MRE deformation loaded with a force on top with mesh.

Figure 58 shows the internal magnetic forces for the particles as they are trying to attract to each other. Therefore, it can be concluded that particles tend to get closer to each other so that the stiffness properties of the MRE are varied at different magnetic field strength. In addition and prior to the main results, this analysis can be shown in this representation when a load is at the top and the mesh of the MRE is appearing and the magnetic field is applied on it. This can be shown in Figure 59.

The 3D plot of the deformed and undeformed MRE is shown in Figure 60. In Figure 60 (a), the force of 0.005 N is applied on the upper surface (node 1) with 0 mT and the deformation plot of the displacement field and magnetic flux density arrows is shown. The lower surface (node 2) is fixed, from the range of the maximum displacement the value of the deformation 1.4 μm. On the other hand, the same approach is done while an external magnetic field is applied in the + y–axis (B = 0.002512 mT) as in Figure 60 (b). The deformation is 0.678 μm. It can be concluded that the displacement is decreased when the magnetic field is applied. This proves that the stiffness has increases and hence, the displacement decreases.

This analysis is done for different values of the magnetic field; a parametric sweep is done in COMSOL to repeat the simulation at values from 0 mT to 0.008792 mT of magnetic field. The displacement values are obtained and the linear stiffness k_l is calculated using Eq. (56).

(a)   (b)
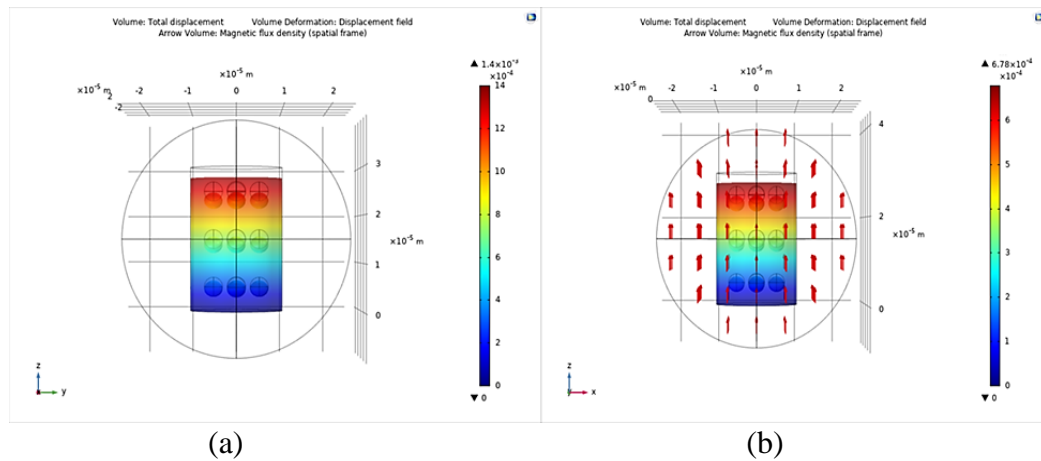
Figure 60. Volume displacement of the MRE for -0.005 N at a magnetic field of a) 0 T and b) 0.002512 T.

Similarly, for the torsional stiffness k_t using Eq. (60), the rigid body rotation as a top view is shown in Figure 61. It can be clearly seen that in the when the

75

magnetic field of 0.002512 mT is applied, the range of the rotation along y-axis indicates that the rotation (angle) has been reduced from 49.2° to 29.5°. The torsional stiffness has a direct proportionality with the magnetic field. This simulation has been repeated for a magnetic field of 0 mT to 0.008792 mT.

The comparison in both linear/torsional deformation with/without the magnetic field is chosen when B = 0.002512 mT, and this due to the proper size of the arrows. The arrows represent the magnitude of the external magnetic field that affects the system. All deformation/rotation plots in each magnetic field value are presented in Appendix B.

(a)   (b)
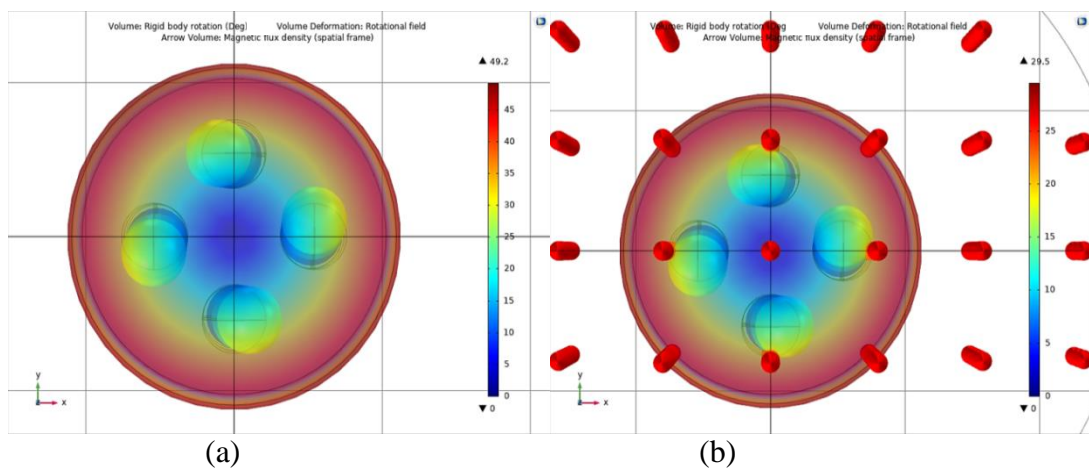
Figure 61. Rigid body rotation of the MRE for 0.005 N.m at a magnetic field of a) 0 T and b) 0.002512 mT.

3.2.4.1 MRE stiffness in linear and torsional modes results

The simulation is done for different values of magnetic fields and the stiffness in both modes are calculated. Figure 62 shows the plot of the linear stiffness and displacement with respect to the magnetic field at constant force applied at node 1, the linear stiffness k_l increases with the magnetic field. The linear stiffness has shown 28.75% increase when the 1st magnetic field is applied (B = 0.001256 mT).

The maximum stiffness reached is 12.9 N/mm (B = 0.008792 mT) while the minimum stiffness is 3.9 N/mm (B = 0 mT). Hence, the displacement is changed when the stiffness of the MRE is also changed. When there is no magnetic field, the displacement at node 1 is 0.00128 mm while it reached 0.000387 mm when the magnetic field is 0.008792 mT. For torsional stiffness k_t, results show similar trend. The torsional stiffness increases when the magnetic field increases while rotation decreases as in Figure 63. The torsional stiffness has shown 20.12% increase when the 1st magnetic field is applied (B = 0.001256 mT). The maximum and minimum stiffness are 0.04629 N.m/rad (B = 0.008792 mT) and 0.00583 N.m/rad (B = 0 mT), respectively. The rotation is measured by the angle on the upper surface of the MRE after applying the constant torque on it (T = 0.005 N.m). The angle is obtained from COMSOL in degrees and is converted to radians, the angle changed from 0.857 rad (B = 0 mT) to 0.108 rad (B = 0.008792 mT). It can be concluded that the stiffness of MRE in linear and torsional modes increases as the magnetic field is higher.
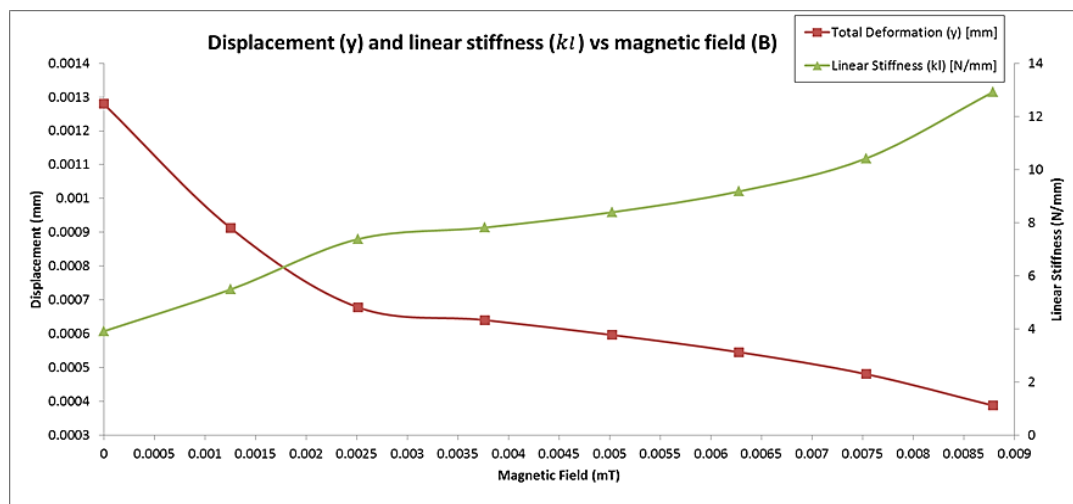
Figure 62. Displacement (along y-axis) and linear stiffness vs. magnetic field plot.
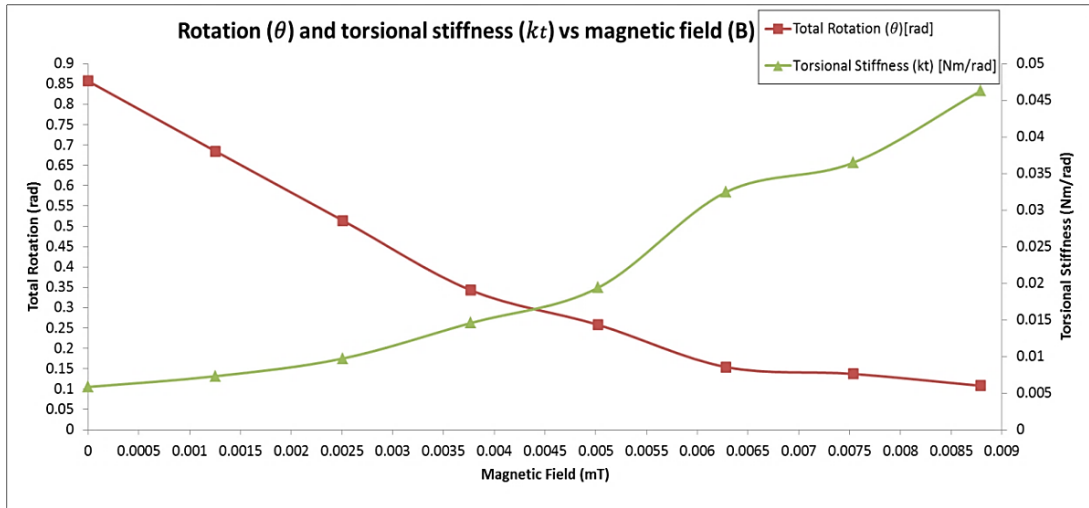
Figure 63. Rotation (about y-axis) and torsional stiffness vs. magnetic field plot.

3.2.4.2 Transmissibility analysis

The second part of the analysis is to find the transmitted load for the MRE when it is excited harmonically. The input harmonic load is applied on the upper surface (node 1) of the MRE and the response on the lower surface is obtained using Eqs. (68-71). The input in both linear and torsional modes is harmonically excited at a range of excitation frequencies. The fundamental frequency obtained by an "eigen frequency" in COMSOL (Eq. (72)) for the linear load is 0.466 MHz while 0.657 MHz for the torsional mode. The values are very large due to the micro scaling of MRE. Therefore, the excitation loads in both modes are applied at a certain range of frequencies which covers the resonance frequency. Figures (64, 65) show the transmissibility curve for the linear and torsional amplitude transmissibility at different magnetic field values. The transmissibility curves are moving to the right and a shift in the natural frequency of the system is observed when the magnetic field increases. The shifting in the natural frequency of the system in both modes indicates that the MRE is becoming stiffer; this stiffening effect on MRE is due to the magnetic field.

78

The values of the natural frequency for both linear and torsional modes with respect to the magnetic field are shown in Figure 66. The natural frequency increases when the magnetic field increases as well. When no magnetic field is applied, the natural frequency of the linear transmissibility is 0.466 MHz, when the magnetic field is applied, the natural frequency increased until it reached 0.483 MHz (B= 0.008792 mT). Similarly, the natural frequency of the torsional mode is 0.657 MHz without magnetic field and it reached 0.661 MHz for the maximum magnetic field (B= 0.008792 mT). The damping ratio of the MRE is almost constant as the peaks of the transmissibility curves are constant because the concern in this model is more focused on the stiffness of the MRE. From Figure 64, when there is no magnetic field applied (B = 0 mT), the 1st natural frequency occurs at 0.466 MHz with a linear transmissibility factor of 13.7. Then, at the same frequency value, with 0.001256 mT applied magnetic field, the transmissibility factor reduces to 2.1. Therefore, as the value of the magnetic field increases, the transmissibility factor decreases, at the same frequency.
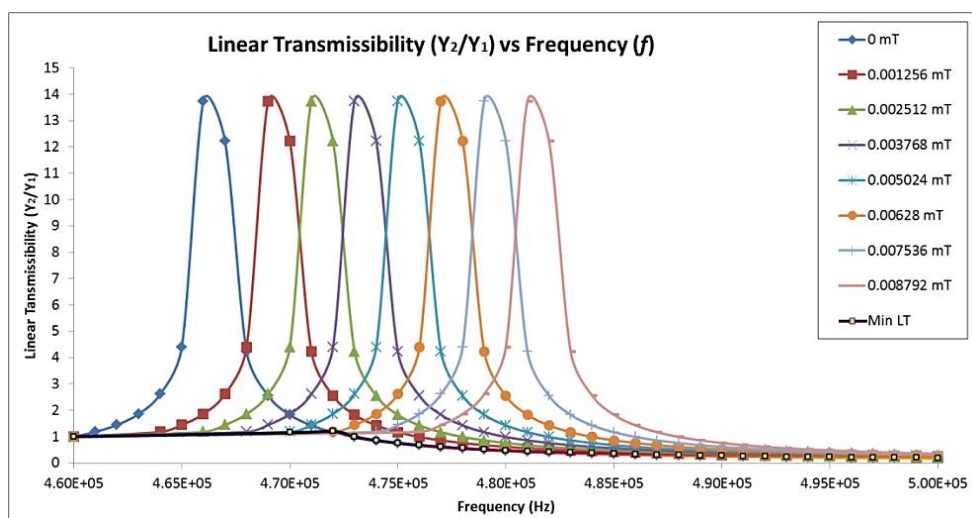
Figure 64. Transmissibility curve for linear amplitude harmonic excitation at different magnetic field strength.

Similarly, for the torsional transmissibility curves, as in Figure 65, as the value of the magnetic field increases, the magnitude decreases. The minimum transmissibility factor that can be achieved is indicated in black dotted lines in both linear transmissibility (Min LT) and torsional transmissibility (Min TT). This indicates that an excitation frequency can be achieved by changing the magnetic field, hence, the stiffness of the MRE. This can be concluded as a minimum value of transmissibility factor can be achieved at a certain excitation frequency by changing the magnetic field which leads to vibration isolation.
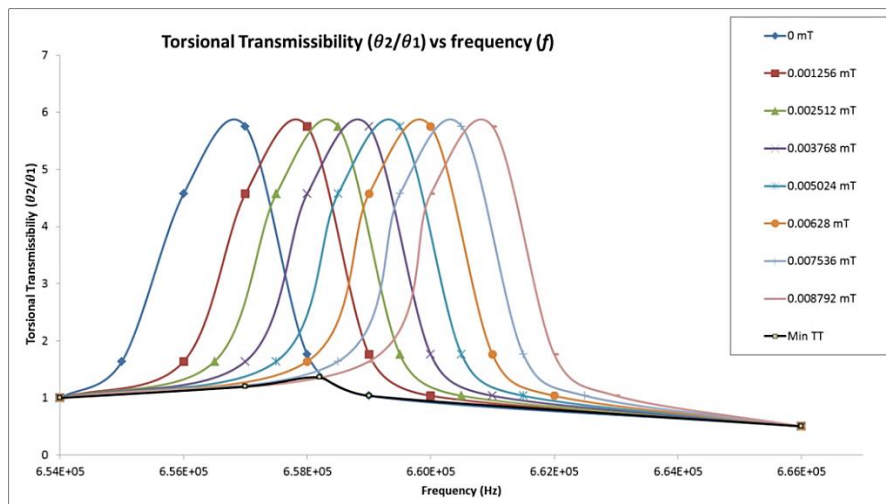
Figure 65. Transmissibility curve for torsional amplitude harmonic excitation at different magnetic field strength.
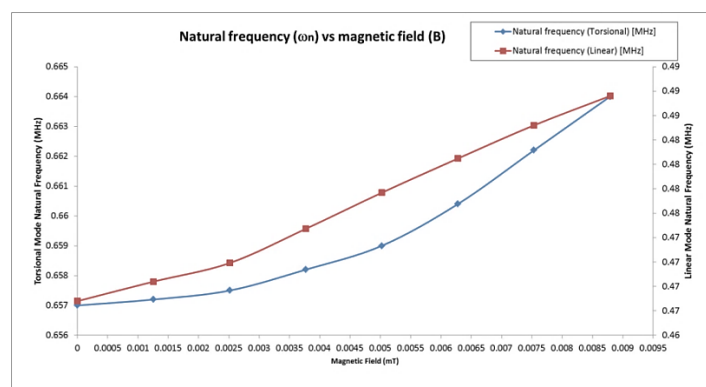
Figure 66. Natural frequency vs magnetic field.

Chapter 4: Experimental Developments and Prototype Setup to Test MRE and Experimental Results

In this chapter, the fabrication of MRE samples, and a prototype of drilling system are presented. In order to test and verify the performance of the MRE, an experimental setup for drilling process is proposed for torsional vibration isolation. This chapter focuses on testing the effect of such MRE on torsional transmissibility through a coupling fitted between to shafts (drill string). Two tests were done in order to study the performance of MRE. All details regarding MRE fabrication, CAD drawings of the proposed drilling application, methodology and experimental setup are discussed. Finally, results and discussion are presented.

4.1 MRE Fabrication

The MRE material used in this work consisted of ELITE DOUBLE 22 silicon rubber mixed at 1:1 base to catalyst ratio, and an iron particles (IP). This type of silicon rubber is chosen based on its strength and flexibility properties. Its high viscosity ensures that the magnetic particles will not precipitate at the bottom of newly made elastomer [93]. Its curing time is just 20 minutes and its simple fabrication as it only requires 1:1 base to catalyst ratio.

Table 10. Properties of Materials for MRE Fabrication.

Materials	Properties	
Silicon rubber	Density $[kg/m^3]$	1.06
	Tear resistance $[N/mm^2]$	5
	Hardness	22
	Settling time [s]	20
	Elastic recovery [%]	99.95
IP	Density $[kg/m^3]$	7.9
	Permeability $[N/mm^2]$	10
	Thermal conductivity [W/m.k]	80.4
	Particle size $[\mu m]$	4

In addition, the versatility of this type of silicon rubber makes it suitable for such dynamic applications. Silicon rubber and IP properties are shown in Table 10. Materials are shown in Appendix C.

Prior to the curing of the silicon rubber (base + catalyst), IP are mixed with the base at a 35% volume fraction (VF). Two cylindrical specimens were manufactured and the fabrication of each specimen used 50 g of silicon rubber (base + catalyst). The volume fraction required for the IP to the silicon rubber is 35%. Therefore, the required amount of IP can be obtained from the following equation

$$m_{IP} = 35\%(50 + m_{IP})$$ (73)

This shows that the required amount of IP is 26.9 g. Knowing that the density of the silicon rubber is 1.06 kg/m^3 and density for IP is 7.9 kg/m^3. The volume fraction can be determined by

$$VF = \frac{V_{IP}}{V_{Total}} = \frac{\frac{m_{IP}}{\rho_{IP}}}{\frac{m_{IP}}{\rho_{IP}} + \frac{m_{Silicon}}{\rho_{Silicon}}}$$ (74)

By applying Eq. (74) , the VF is 6.73% of IP of the total composite. This is the volume fraction between the silicon rubber and IP needed to achieve a 35% IP to silicon rubber ratio.

The fabrication of the mold to cure and cast the MRE is 3D printed using ABS material. The 3D model of this mold is shown in Figure 67. This unique design of the mold consists of three main parts; lower and upper covers, and the middle part. The lower cover was attached to the middle part by a four screws in each corner. Then, the mixed silicon fluid with the IP is poured from the upper part and then the upper cover was attached to middle part in order to keep the MR elastomer inside. The extruded part was made in order to achieve the required design of the MRE that fits the coupling. Dimensions of the mold are found in Appendix C.
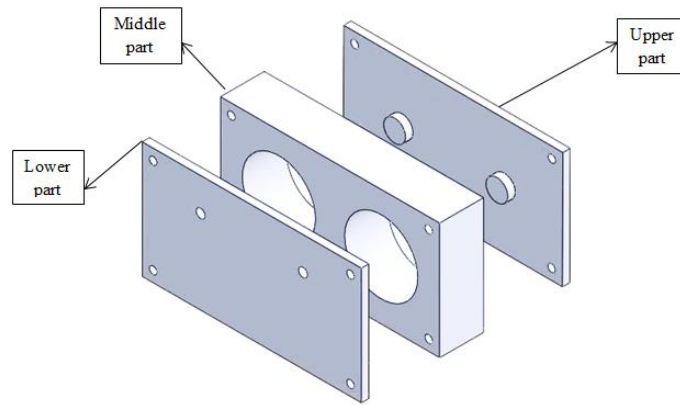
Figure 67. 3D model of the mold for MRE fabrication.

The flexible coupling that will contain the MRE is consisting of three aluminum cylinders. The aluminum cylinders are 50 mm in diameter and 30 mm in height. In addition, these cylinders are extruded in order for the MRE to fit inside it. The extruded part follows a cylindrical shape with a diameter of 15 mm and a height of 5 mm. The MRE dimensions are also similar to the aluminum cylinders with a diameter of 50 mm and a height of 30 mm. On both faces of the MRE, a cylindrical hole is made so that it fits the aluminum cylinders. Figure 68 shows the MRE fitted with coupling. These aluminum cylinders are made using the lathe machine. All 3D drawings and dimensions can be seen in Appendix C.
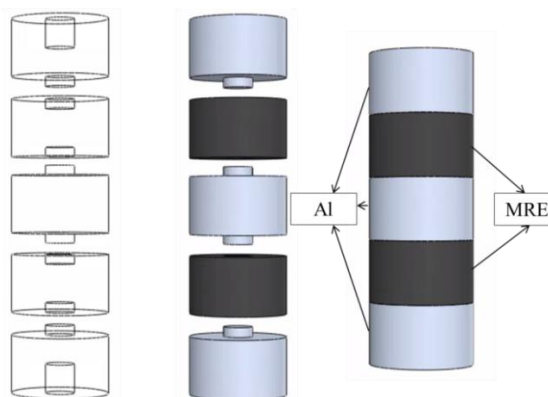
Figure 68. MRE and the coupling 3D design.

The fabrication procedure taken to achieve the desired coupling with MRE fitted in it is as follows:-

1. 3D printed mold: It is modeled using SolidWorks and 3D printed.
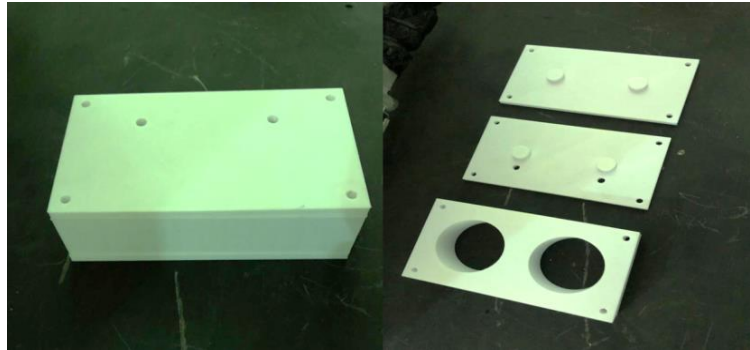
Figure 69. 3D printed mold.

2. MRE composite and mixing: MRE is fabricated using a measuring cup and a digital balance to measure the amount needed for silicon rubber and IP. Firstly, the silicon rubber base is poured to the measuring cup (Figure 70 (a)). Secondly, the IP is added followed by the silicon rubber catalyst (Figure 70 (b, c)). After that, a proper mixing using a mixer is done in order to guarantee that the IP is mixed through the whole composition of the elastomer. Finally, the MRE is poured as a fluid into the mold and was covered for 20 minutes for curing (Figure 70 (d)).

(a)   (b)   (c)   (d)
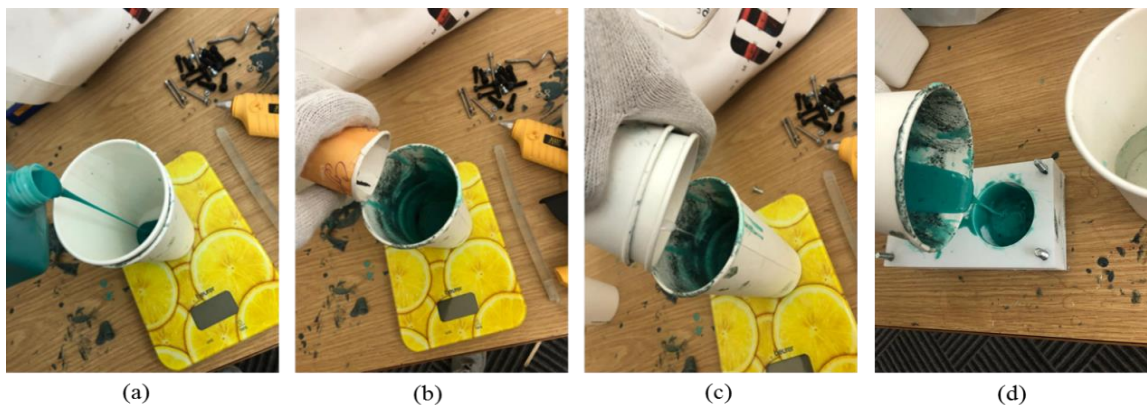
Figure 70. Mixing MRE components.

3. MRE production: After the curing, the MRE samples are ready to be extracted from the mold.

Figure 71. MRE sample after curing.

4. Flexible coupling manufacturing: After getting the MRE ready, the three aluminum cylinders were manufactured using the lathe machine.

Figure 72. Aluminum coupling parts after manufacturing.

5. MRE with the flexible coupling fitting: Finally, the MRE is fitted into the three aluminum cylinders using the extrusions made in their design and by a very powerful epoxy between them. The epoxy makes the MRE samples able to fix between the couplings allowing for the torsional mode of vibration to be studied.

Figure 73. Flexible coupling with MRE.

4.2 Experimental Methodology

This experimental setup in this work is to represent and apply the semi-active torsional vibration isolation in drilling. A test rig was prototyped and developed to apply two different tests (Impact hammer test and continuous rotation test) on it utilizing MRE. The methodology of these experiments can be divided into two parts. The 1st part will be an impact hammer test in order to obtain the angular acceleration/displacement transmissibility when the system is in static. This is in order to apply an excitation input on the system before the MRE coupling existence and get its response afterwards, as a Frequency Response Function (FRF). Secondly, a dynamic test which will investigate the angular displacement transmissibility in a continuous rotation of the shaft (drill string).

4.2.1 3D CAD drawing and mathematical model development

The 3D CAD drawing of the system can be shown in 3D isometric view in Figure 74. The system is vertically oriented as a representation of a drilling process. The system consists of motor to drive torque to the shaft (drill string). Two accelerometers are fitted on two plates (upper and lower) attached to the shaft. In

addition, a slip ring is used in order to transmit the accelerometers readings while rotation. A flexible coupling which contains the MRE. Electromagnetic coil which surrounds the MRE in order to produce the magnetic field. Finally, the disc which attaches the drill bit at the bottom of the drill string. The shaft is 25 mm in diameter and 600 mm in length. The whole length of the system does not exceed 1 m. This short length of the shaft is in order not to create bending or wobbling during rotation and to try as much as possible to keep the system aligned while rotation. All dimensions are in Appendix C.
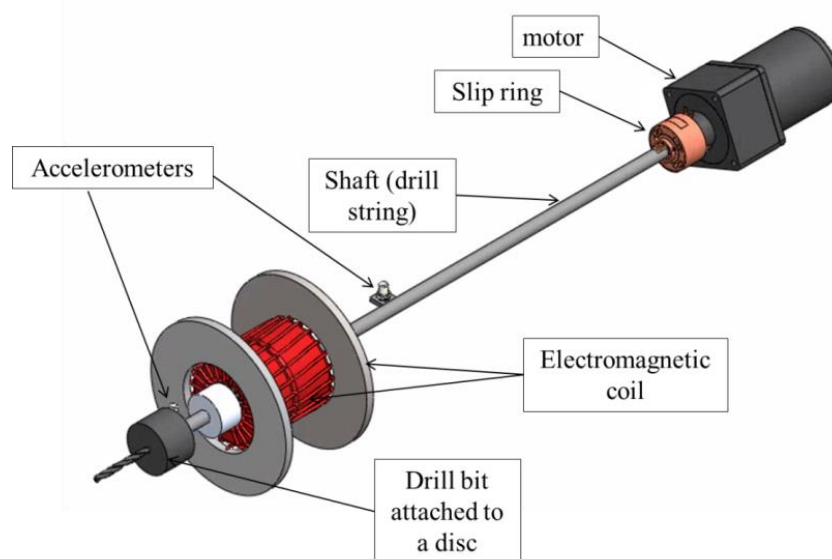
Figure 74. 3D CAD drawing of the proposed drilling system.

In order to obtain the mathematical model of this system, some assumptions are made in order to simplify the model. Figure 75 (a) shows the vertical orientation of the system and a zoomed snap for the MRE coupling as in Figure 75 (b, c). The main concept of this analysis is to obtain the angular displacement transmissibility from the mathematical model in order to isolate the torsional vibration isolation in drilling using MRE.
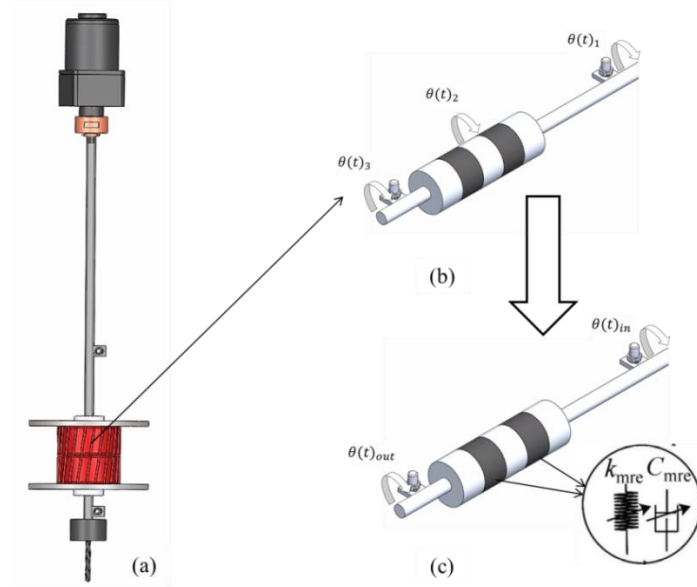
Figure 75. (a) Vertical orientation of the proposed drilling system, (b) Schematic mathematical model derivation, (c) Mathematical model simplification.

The derivation of the mathematical model of this system starts with the displacement transmissibility definition. In mechanical vibration, the concept of the displacement transmissibility is very significant as it is the magnitude of the ratio of how much oscillation is being transmitted to a point from the excitation input of the source. Since the torsional vibration is to be isolated, the angular displacement transmissibility is presented which the ratio of the angular displacement (rotation) transmitted to the excitation torque. In general, the angular (torsional) displacement transmissibility can be presented as follows

$$TT = \frac{output\ angular displacement}{input\ angular\ displacement} \tag{75}$$

As it can be seen from Figure 75 (b), the two MR elastomers are separated by an aluminum cylinder as a part of the coupling. Therefore, three angular displacements are presented; the input angular displacement from the motor to the shaft before the MRE coupling $\theta(t)_1$, the angular displacement of the middle cylinder part $\theta(t)_2$, and the third angular displacement $\theta(t)_3$. The torsional transmissibility of

points 1 and 2 can be expressed by

$$TT_{1,2} = \frac{\theta(t)_2}{\theta(t)_1} \tag{76}$$

Similarly, the torsional transmissibility of points 2 and 3 can be expressed by

$$TT_{2,3} = \frac{\theta(t)_3}{\theta(t)_2} \tag{77}$$

The torsional transmissibility of points 1 and 3 can be expressed by

$$TT_{1,3} = TT_{1,2} \times TT_{2,3} = \frac{\theta(t)_2}{\theta(t)_1} \times \frac{\theta(t)_3}{\theta(t)_2} = \frac{\theta(t)_3}{\theta(t)_1} = \frac{\theta(t)_{\text{out}}}{\theta(t)_{\text{in}}} \tag{78}$$

Therefore, the simplified schematic of the mathematical model based on the angular transmissibility analysis can be seen from Figure 75 (c). The following analysis is similar to what was done in Chapter 3; Section 3.1 for the analytical simulations, but this analysis represents the angular behavior of a system. The mathematical model of the system including the MRE coupling starts with a basic equation of motion of single degree of freedom with input angular displacement $\theta(t)_{\text{in}}$, and output angular displacement $\theta(t)_{\text{out}}$. The equation of motion that describes the system performance and behavior by a set of differential equations is as follows

$$\sum T = J\ddot{\theta} \tag{79}$$

$$J(\ddot{\theta}_{out}) + c_{mre}(\dot{\theta}_{out} - \dot{\theta}_{in}) + K_{mre}(\theta_{out} - \theta_{in}) = 0 \tag{80}$$

where J is the mass moment of inertia, $\dot{\theta}_{out}$ is the output angular velocity, $\dot{\theta}_{in}$ is the input angular velocity, θ_{out} is the angular displacement, θ_{in} is the input angular displacement. K_{mre} and c_{mre} are the stiffness and damping coefficient of MRE which can be expressed in this form

$$J(\ddot{\theta}_{out}) + c_{mre}\dot{\theta}_{out} + K_{mre}\theta_{out} = c_{mre}\dot{\theta}_{in} + K_{mre}\,\theta_{in} \tag{81}$$

The transfer function of this system can be obtained by applying the Laplace transform to differential equation Eq. (81). Applying of $\theta(t) = \Theta(s)$

$$Js^2\theta(s)_{out} + c_{mre}s\theta(s)_{out} + K_{mre}\theta(s)_{out} = c_{mre}s\theta(s)_{in} + K_{mre}\theta(s)_{in} \qquad (82)$$

By taking the common factors

$$[Js^2 + c_{mre} + K_{mre}]\theta(s)_{out} = [c_{mre} + K_{mre}]\,\theta(s)_{in} \qquad (83)$$

The transfer function can be obtained by

$$\frac{\theta(s)_{out}}{\theta(s)_{in}} = \frac{c_{mre}s + K_{mre}}{Js^2 + c_{mre}s + K_{mre}} \qquad (84)$$

The angular displacement transmissibility factor equation can be obtained firstly by converting Eq. (84) from the (s-domain) to the frequency domain (ω-domain) in terms of amplitude and phase. By replacing $s = j\omega$

$$T = \frac{\theta(j\omega)_{out}}{\theta(j\omega)_{in}} = \frac{c_{mre}(j\omega) + K_{mre}}{J(j\omega)^2 + c_{mre}(j\omega) + K_{mre}} = \frac{c_{mre}j\omega + K_{mre}}{-J\omega^2 + c_{mre}j\omega + K_{mre}} \qquad (85)$$

The angular displacement (torsional) transmissibility factor can be obtained by taking the magnitude of Eq. (85)

$$TT = \left|\frac{\theta(\omega)_{out}}{\theta(\omega)_{in}}\right| = \left|\frac{\theta_{out}}{\theta_{in}}\right| = \sqrt{\left[\frac{(c_{mre}\omega)^2 + (K_{mre})^2}{c_{mre}\omega)^2 + (K_{mre} - J\omega^2)^2}\right]} \qquad (86)$$

4.2.2 Impact hammer test methodology

The methodology used in the impact hammer test is a modal analysis. Modal analysis is a very important and effective way to understand the vibration characteristics and behavior of mechanical structures. It converts the vibration signals of excitation and responses into a set of model parameters. In this test, the impact using a hammer was applied on one point in order to get the response on another point in the presence of MRE. The excitation is a force and the response is obtained as an acceleration using an accelerometer. However, the needed output in this test is to obtain the angular acceleration transmissibility factor (TTF). This was done in order to investigate the influence of the MRE under a magnetic field in vibration isolation. Figure 76 shows the method followed in this test.

90
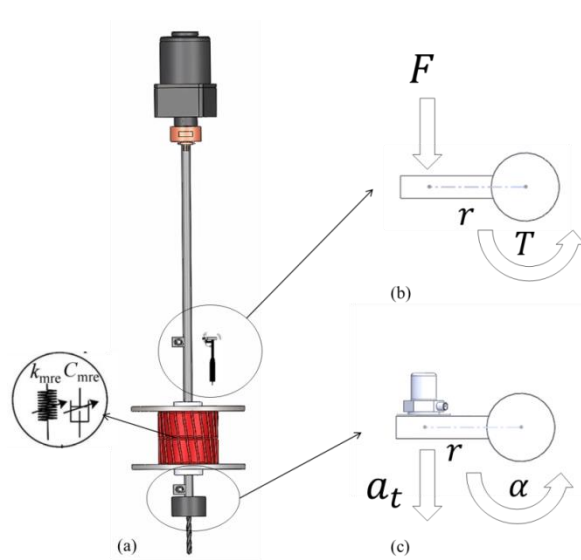
Figure 76. Methodology of the impact hammer test, (a) impact and response locations, (b) input excitation representation, and (c) output response representation.

The impact was done on the upper plate as shown in Figure 76 (b) and the response is obtained using the accelerometer fitted on the lower plate as in Figure 76 (c). This test is done in order get the transmitted load of the shaft before and after the presence of MRE. The response needed in this test is the frequency response function (FRF) which represents the transfer function of the system. The transfer function is the ratio between the output response and the input excitation. The response obtained from this test is the frequency response in terms of the ratio of the excitation force (F) to the output acceleration (a_t). The accelerometer used is a uniaxial, which means it reads the amplitude along its axis; in this case, the orientation of the accelerometer permits it to read the acceleration in the tangential direction. The FRF needed in this experiment must be in angular domain because the application is to obtain the angular (torsional) transfer function FRF. The FRF obtained from the data acquisition system is as follows

$$FRF = \frac{a_t}{F} \tag{87}$$

where a_t is the tangential acceleration and F is the excitation force input. The

91

uniaxial accelerometer is able to read the acceleration along its axis (1D). So, the relationship between the tangential acceleration a_t and angular acceleration α can be given by

$$\alpha = \frac{a_t}{r} \tag{88}$$

where r is the radius of from the shaft center to the accelerometer axis. The torque T can be related to force F as

$$T = Fr \tag{89}$$

By substituting Eqs. (87)-(88) into Eq. (89)

$$FRF = \frac{a_t}{F} = \frac{\alpha r}{\frac{T}{r}} = \frac{\alpha}{T}r^2 = TTF \tag{90}$$

The output angular acceleration to input torque angular torsional transfer function TTF can be obtained by

$$TTF = \frac{FRF}{r^2} = \frac{\alpha}{T} \tag{91}$$

The TTF is converted from the linear ($\frac{a_t}{F}$) to torsional ($\frac{\alpha}{T}$). The torsional transfer function (TTF) can be presented in terms of angular displacement, angular velocity and angular acceleration. The mathematical model obtained for this system as in Eq. (86) shows the torsional transfer function. However, the angular acceleration transfer function equation also represents the idea behind the displacement transfer function as it is a ratio of output to input. Therefore, the representation of this factor by one of the parameters is acceptable. After obtaining the angular (torsional) transfer function with respect to the frequency, half bandwidth theory is applied in order to obtain the damping ratio and the torsional stiffness of the MRE as the magnetic field increases. Half bandwidth theory can be represented in Figure 77.
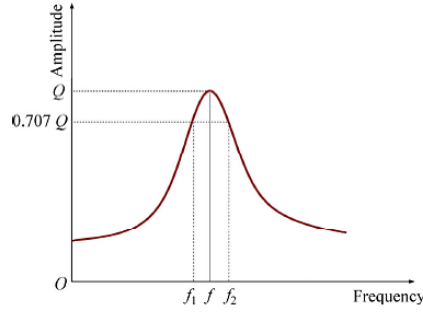
Figure 77. Half bandwidth theory [94].

The damping ratio ζ can be expressed by

$$\zeta = \frac{1}{2Q} \tag{92}$$

where Q is the Q factor which can be expressed by

$$Q = \frac{f}{f_2 - f_1} \tag{93}$$

where f is the resonance frequency, f_1 and f_2 are the frequencies measured -3 dB down from the peak or at $0.707Q$, or at $(\frac{1}{\sqrt{2}}) TF_{maximum}$, where TF is the transmissibility factor [95]. The torsional stiffness of the MRE is obtained from the frequency domain function (FRF). The torsional stiffness k_t of the MRE is obtained from the expression

$$\omega_n = \sqrt{\frac{k_t}{J}} \tag{94}$$

where ω_n is the natural frequency of the system. k_t is the torsional stiffness of MRE and J is the mass moment of inertia of the disc attaching the drill bit. The damping coefficient c, of MRE can be obtained in terms the torsional stiffness k_t, torsional moment of inertia J, and the damping ratio ζ by using the critical damping c_c as follows

$$c_c = \sqrt{4Jk_t} \tag{95}$$

$$c = \zeta\, c_c \tag{96}$$

The schematic representation of the methodology and experimental setup for this test is shown in

Figure 78. This test is done while the system is in static. The impact is done on the upper plate by the hammer in order to get the response on the lower accelerometer. The data acquisition system (DAQ) receives the two generated signal of the excitation torque input and the output angular acceleration response and uses the fast Fourier transform to convert the data from time domain into a frequency domain (FRF). The DC regulated power supply is used to supply the electromagnetic coil by a current which is delivered as a magnetic field. The coil surrounds the MRE in order to get its response to the magnetic field. The current values ranges from 0 A to 3 A. The slip ring is used to deliver the response signal of the lower accelerometer to the DAQ. The gauss/tesla meter is used to measure the magnetic field inside the coil when the current supplied is varied. The disc that attaches the drill bit is used to give a moment of inertia during the test.
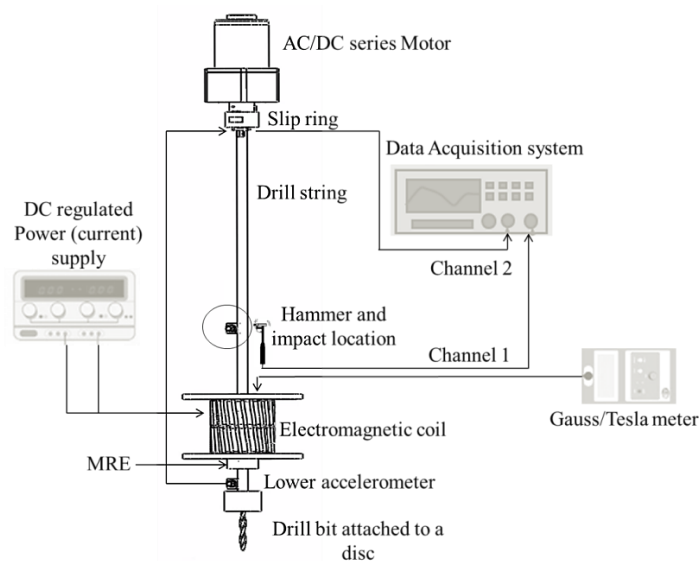
Figure 78. Schematic representation of the impact hammer test methodology and experimental setup to obtain TTF.

4.2.3. Continuous rotation test methodology

The methodology followed in this experiment is to test and investigate the effect of MRE in torsional vibration isolation in drilling process in continuous rotation. It is similar to the previous methodology by which the torsional transmissibility TT is to be obtained. However, this test is done during the continuous motion of the drilling system. The drilling system is rotating at a certain speed (revolutions per minute). Two accelerometers are attached before and after the MRE. The readings (angular acceleration) of the accelerometers are delivered to the DAQ as a time domain (acceleration vs time). These readings can be integrated twice to get the angular displacement. However, since the transmissibility factor is a ratio, no need for the conversion. The method is shown in Figure 79.
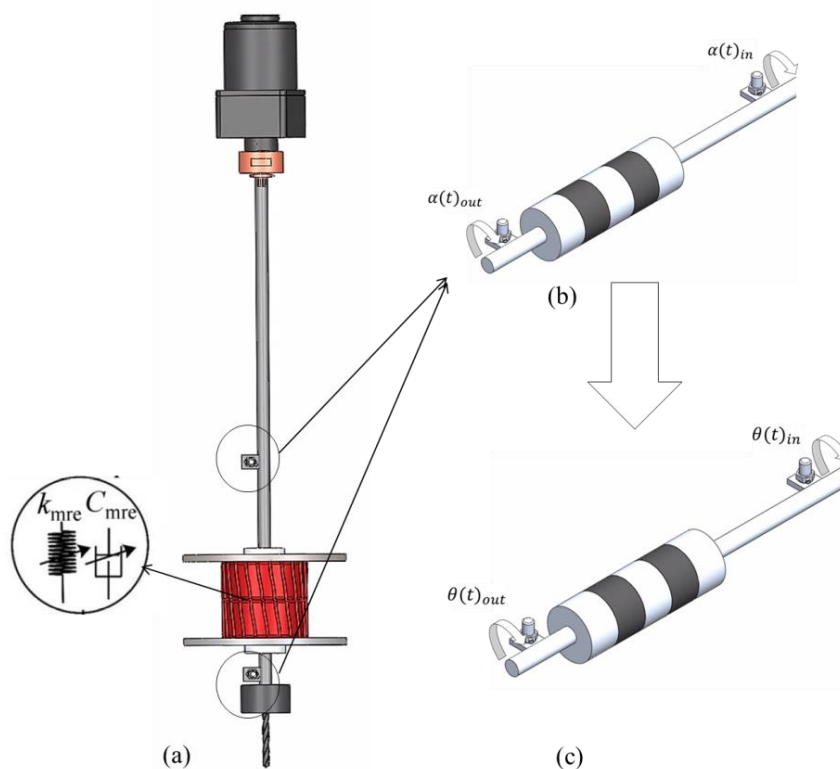
Figure 79. Continuous rotation test methodology, (a) input and output locations, (b) output and input angular acceleration, and (c) output and input angular displacement.

Since the relationship between tangential acceleration and angular acceleration was given as in Eq. (88)

$$a_t = \alpha r$$

where a_t is the tangential acceleration, α is the angular acceleration, and r is the radius of the shaft.

Therefore, since both shafts (drill string) have the same radius r, the angular acceleration (torsional) transmissibility TT can be obtained by

$$TT = \frac{a_{t_{out}}}{a_{t_{in}}} = \frac{\alpha_{out} r}{\alpha_{in} r} = \frac{\alpha_{out}}{\alpha_{in}} \tag{97}$$

where α_{out} is the output angular acceleration and α_{in} is the input angular acceleration. In order to get the angular displacement transmissibility, the input and output angular accelerations can be integrated twice as the following

$$\theta_{in}(t) = \iint_0^t \alpha_{in}(t) \tag{98}$$

$$\theta_{out}(t) = \iint_0^t \alpha_{out}(t) \tag{99}$$

where $\theta_{in}(t)$ and $\theta_{out}(t)$ and are the input and output angular displacement with respect to time t, respectively. Since the transmissibility represents a ratio, therefore, the angular acceleration transmissibility is assumed to be equal to the angular displacement transmissibility as shown in Figure 79 (b, c), the torsional transmissibility factor becomes as follows

$$TT = \frac{\theta_{out}(t)}{\theta_{in}(t)} = \frac{\alpha_{out}}{\alpha_{in}} \tag{100}$$

To summarize, the idea of this test is to investigate the angular displacement transmissibility of the system under continuous rotation. The motor drives the shaft (drill string) at a constant speed (RPM) using the external power supply (voltage). The

voltage range is from 5 V to 7 V with an increment of 0.25 V. The motor starts to rotate at 5V. This is due the load of the system. The speed (rotation) of the shaft (drill string) is measured using a tachometer (in RPM) and then converted to frequency (Hz). This conversion was done using $f(Hz) = N(rpm)/60$, where f is the frequency, and N is the rotational speed in revolutions per minute.

Then, the readings of both accelerometers (acceleration vs time) are delivered to the DAQ. Finally, the ratio between the upper and lower accelerometers readings at that certain frequency is plotted with respect to it. This test was done for a current supply values similar to the impact test (0 A – 3 A). Gauss/Tesla meter is used to measure the magnetic field inside the electromagnetic coil similar to the impact test. The schematic representation of the methodology and experimental setup is shown in Figure 80.
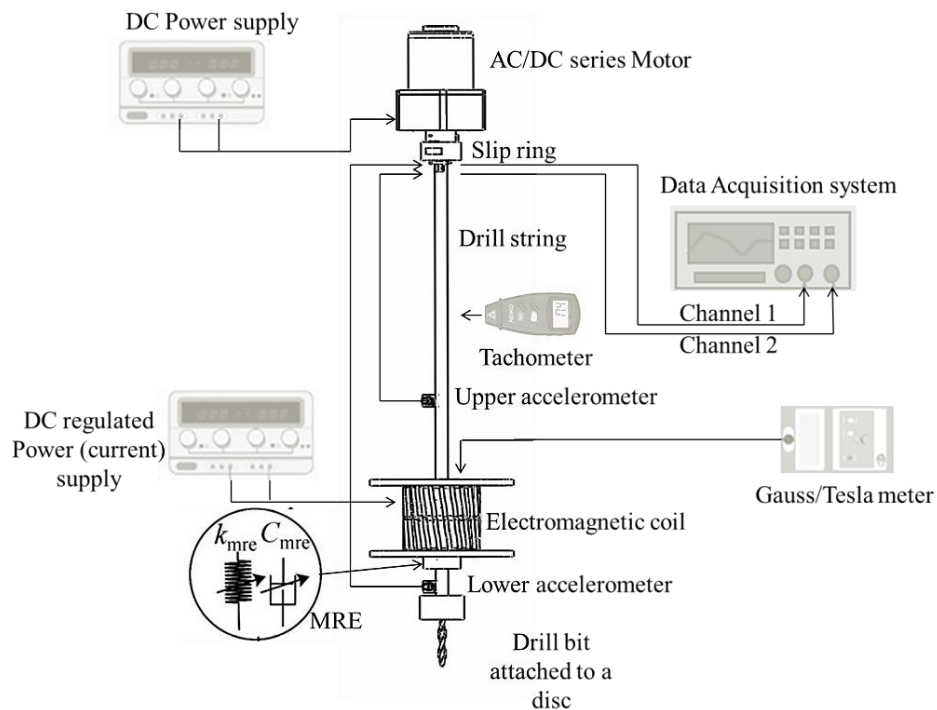
Figure 80. Schmatic representation of the methodology and experimental setup of the continuous rotation test.

4.3 Experimental Setup and Developments

This section will further explain the methodology used in both tests by representing the experimental setup and all other developments related to it. Figure 81 shows the experimental setup used in both tests.
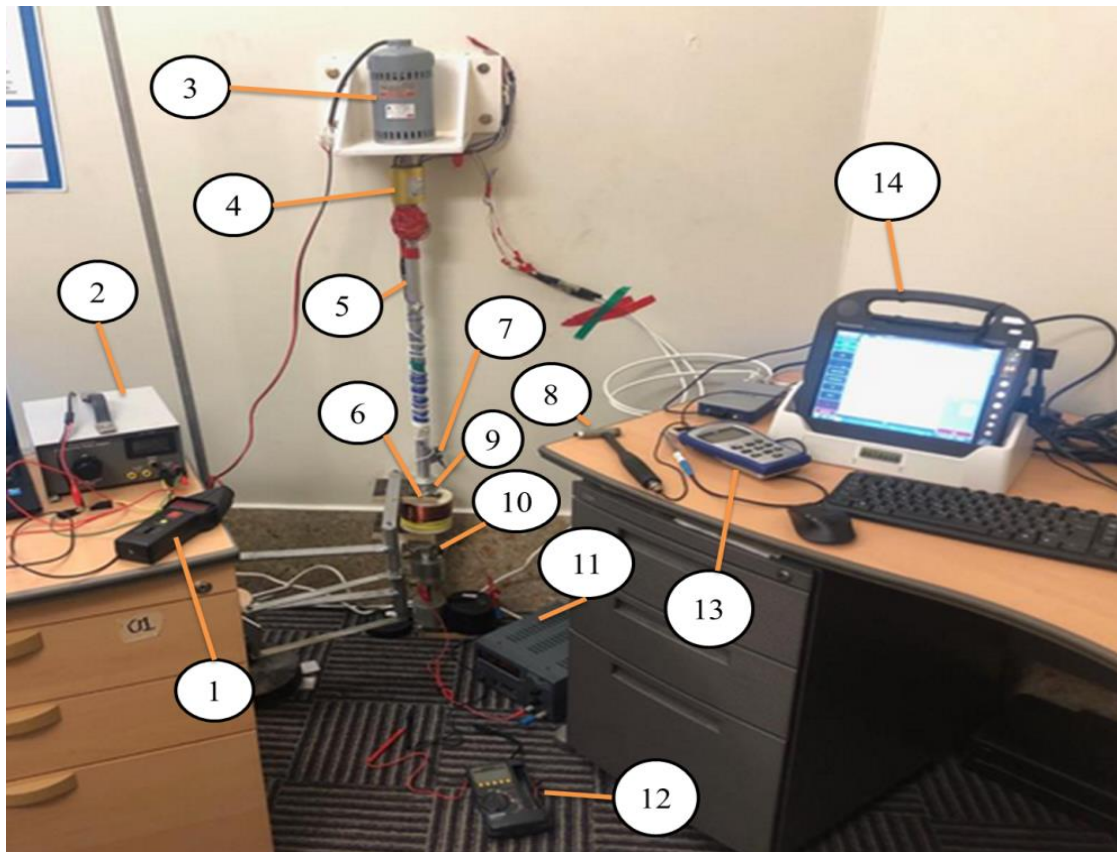
(1) Tachometer, (2) Power supply unit, (3) AC-DC series motor, (4) Slip ring, (5) Shaft (drill string), (6) Electromagnetic coil, (7) Upper accelerometer, (8) Hammer, (9) MRE, (10) Lower accelerometer, (11) DC regulated power supply, (12) Digital Multi meter (DMM), (13) Gauss/Tesla meter, and (14) Data acquisition system (DAQ).

Figure 81. Experimental setup for both tests.

The experimental setup for the impact hammer test consists of an aluminum shaft representing the drill string. An ICP type accelerometer sensor which a sensitivity of 101.2 mv/g which includes a built-in amplifier is fitted after the MRE as in (10) in Figure 81. It is connected to the DAQ (CF-H2 TOUGHBOOK) as an input channel 2. The hammer (PCB) is used to give an excitation signal as torque to the

upper plate. The upper plate fitted the upper accelerometer for the second test. However, using the other side of it, the impact was given. This can be shown in Figure 82. The hammer is connected to the DAQ as an input channel 1. The slip ring (MT01218-0612) is used to deliver the response of the lower accelerometer to the DAQ. The MRE is fitted with its coupling in order to act as a vibration isolator in the system surrounded by the electromagnetic coil with a power supply to provide it with a current in order to produce magnetic field. A disc is inserted with drill bit in order to give a moment of inertia as in Figure 82.
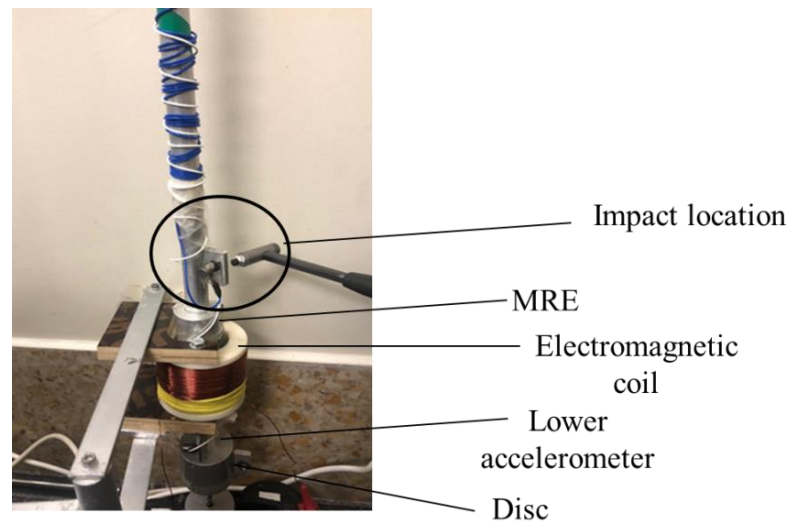
Figure 82. Imapct hammer test experimental representation.

The experimental setup for the continuous rotation test consisted of an aluminum shaft (drill string). An AC-DC series motor (2M191A) to drive the shaft. Power supply unit is used to control the motor by producing voltage. The slip ring is used also to deliver the signals of the upper and lower accelerometers while rotation to the DAQ as input channels 1 and 2, respectively. The two accelerometers are an ICP type with sensitivity of 101.2 mv/g. The tachometer (CT6) is used to measure the rotation of the shaft at a certain voltage input to the motor as shown in Figure 83 (a).
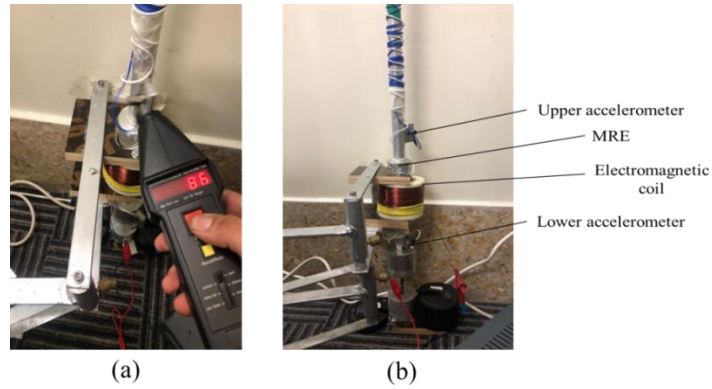
Figure 83. Tachometer for speed measurement and experimental representation of continuous rotation test.

For both tests, the electromagnetic coil is used. It consists of an ABS material core which was 3D printed. In addition, winding was used to roll a copper wire around it. The coil has 624 turns. FW Bell Gauss/Tesla meter is used to measure the magnetic field inside the core which has the MRE in between. The coil is fixed using a stand and a wooden case. Insulated materials are used in order not to absorb any magnetic flux produced from the coil and to insure that the flux is included inside so that the magnetic influence appears only on the MRE. This can be shown in Figure 84. The digital multi meter (DMM) is used to measure the current passed to the coil to verify the power supply (current) output.
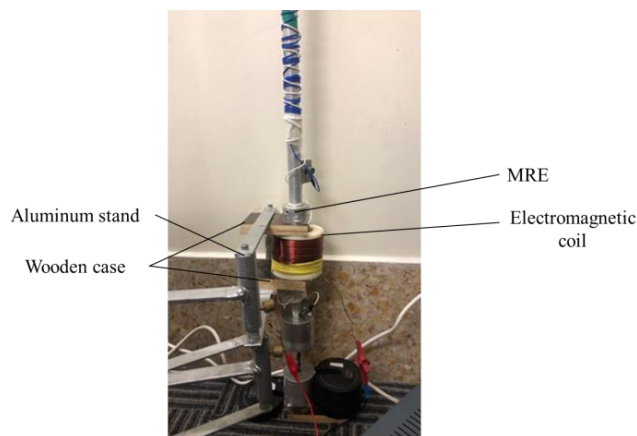
Figure 84. Electromagnetic coil fixation.

4.4 Experimental Results and Discussion

To start with, the common thing which was used in both experiments is the electromagnetic coil. The electromagnetic coil was used to produce a magnetic field to the MRE. The current (0 A – 3 A) was supplied to the coil using a power supply and the magnetic field generated inside the core of the electromagnetic coil is noted as in the data table in Figure 85. It also shows the relationship between the current supplied to the coil and the magnetic field applied. It can be clearly seen that as the current increases, the magnetic within the coil increases as well. Measurement of the magnetic field during the experiment is essential in order to ensure that the MRE is being influenced by magnetic flux intensity.
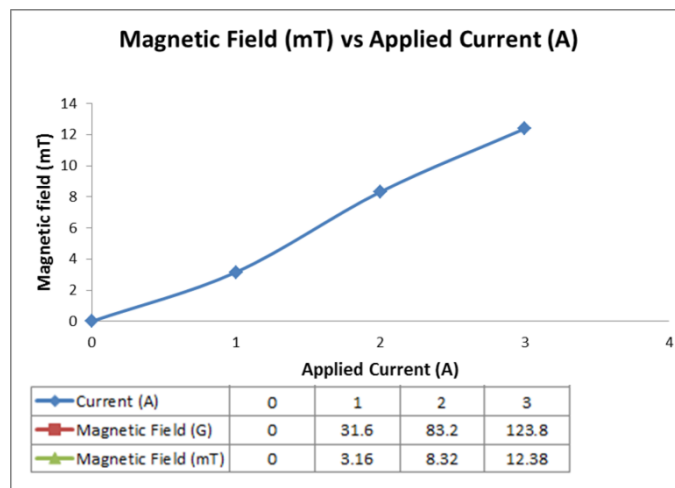
Figure 85. Magnetic field generated vs applied current.

4.4.1 Impact hammer test results

Results of the impact test indicate the TTF torsional transmissibility factor with respect to a range of frequencies given by the impact. The impact test was repeated three times at each value of the magnetic field and then results are averaged. In each time, 5 impacts where taken and averaged by the DAQ. The sampling frequency of this test was 12800 Hz. This test was done in order to reveal MRE

efficiency in torsional vibration isolation in the proposed drilling system. In addition, to investigate the effect of the magnetic field variation on the torsional stiffness and damping properties. FRF (TTF) plot was extracted from the DAQ results were processed as in Eqs. ((88)-(91). The torsional transfer function TTF which includes the excitation torque input and the angular acceleration response for different current values is presented in Figure 86. It is obtained that at different range of frequencies; the values of the TTF are varied as the current values changes. The system starts to vibrate at its maximum in the low frequency range (0 Hz – 50 Hz); this indicates that the resonance frequency occurs at this range. Above 50 Hz, many amplitudes and patterns appear as there is a fluctuation in the TTF. This is due to the rebound effect of the impact test as the DAQ system takes fractions of a second to capture the results. The focus in this research will be given to the low frequency ranges. This range agrees with the fact that vibration problems in most rotary machines occurs at low excitation frequencies, this leads for large amplitudes of vibration during resonance [96]. Therefore, Figure 87 is a zoomed out lot of Figure 86.
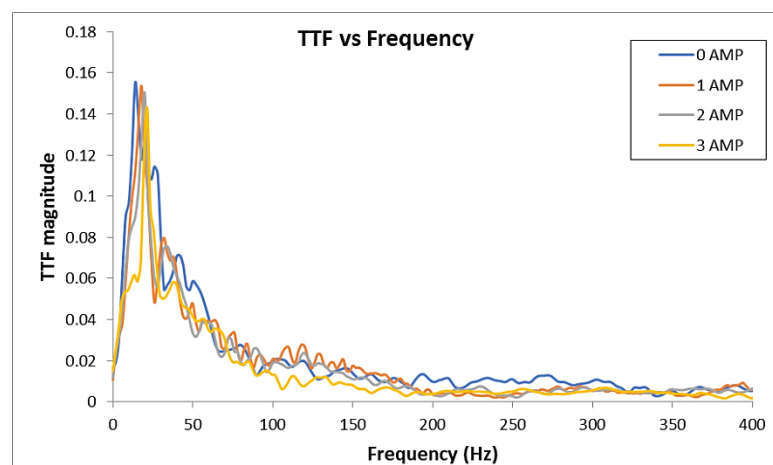
Figure 86. TTF factor vs frequency.

Figure 87 represents the TTF curves plot in the low frequency range (0 Hz –

50 Hz). The 1st natural frequency occurs at 13.9 Hz with TTF magnitude of 0.15522 rad/N.m.s^2. After that, at the same frequency, the drops to 0.1117 rad/N.m.s^2 when the applied current value is 1 A. Therefore, it can be concluded that as the value of applied current increases, the TTF reduces. In contrast, the transmissibility factor increases when the current is decreased, and the frequency increases. This means that a minimum TTF can be achieved at a certain excitation frequency by changing the magnetic field which leads to torsional vibration isolation. When the current value is 1 A, the resonance frequency becomes 17.5 Hz. This indicates that the effect of the MRE under magnetic field shifted the natural frequency of the system from its original natural frequency under the effect of the passive stiffness and damping properties of MRE. When the current is 3 A, the natural frequency of the system reaches 21.45 Hz, beyond the resonance frequency when there is no applied current. The natural frequency of the system increases as the applied current increase as shown in Figure 88; the TTF curve is being shifted to the right. This is due to the stiffening effect of MRE under a magnetic field.
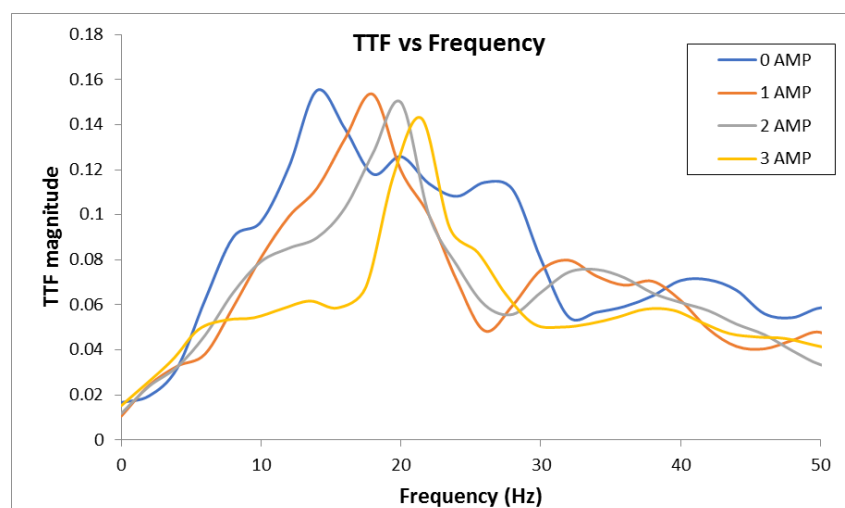
Figure 87. TTF magnitude vs frequency (0 Hz - 50 Hz).
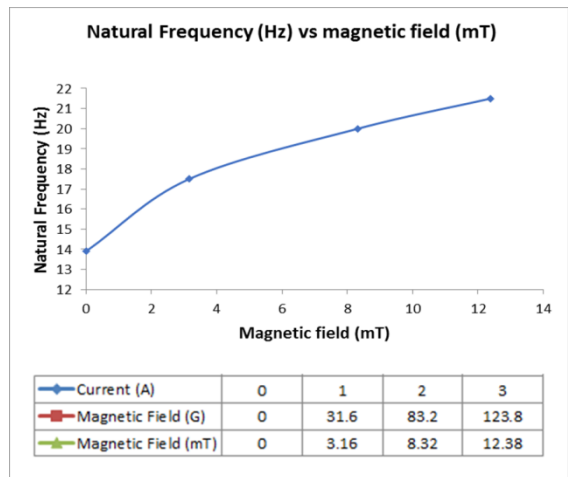
Figure 88. Natural frequency of the system vs magnetic field and applied current.

The values of the torsional stiffness of the MRE for the applied current range are calculated using Eq. (94) where the inertia of the disc is $J = 0.0016\ kg.m^2$. Figure 89 represents the torsional stiffness of MRE with respect to the applied current. It can be clearly seen that as the current increases, the torsional stiffness increases. This illustrates the shifting in the natural frequency of the system. When the 1st value of the magnetic field is applied to the system, an increase of 36.8% in the stiffness is found. The change in the torsional stiffness of MRE is considerable as it increased from 12.2 N.m/rad (No current) to 29.2 N.m/rad when the current reached 3 A (12.38 mT of magnetic field) as it shown in Table 11.
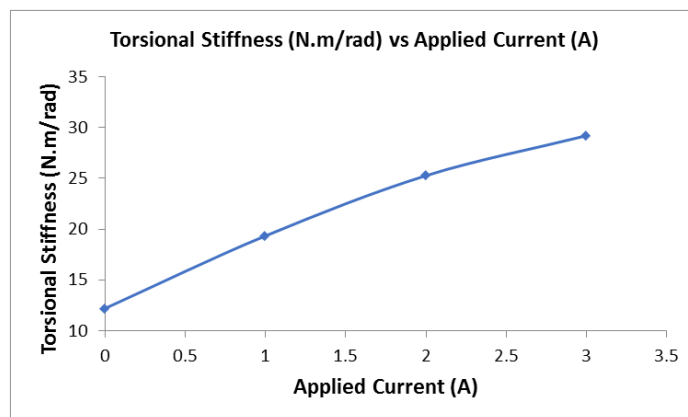
Figure 89. Torsional stiffness of MRE vs applied current.

The values of the damping coefficient are obtained from the TTF curves by using the half power bandwidth method as in Eqs. (92), (93) highlighted in the methodology. Figure 90 shows the values of the MRE torsional damping coefficient with respect to the applied current. It can be clearly seen that the damping coefficient of MRE slightly increases by increasing the applied current. Results shows that the damping characteristics of MRE do not change much with magnetic field as it the damping coefficient changed from 0.079 $kg.m^2/rad.s$ to 0.12 $kg.m^2/rad.s$ when the when the current reached 3 A (12.38 mT of magnetic field). This outcome coincides with the theory that the damping characteristics of MR elastomers do not change much by the influence of magnetic field. A summary of all results in terms of MRE torsional stiffness and damping coefficient is shown in Table 11.
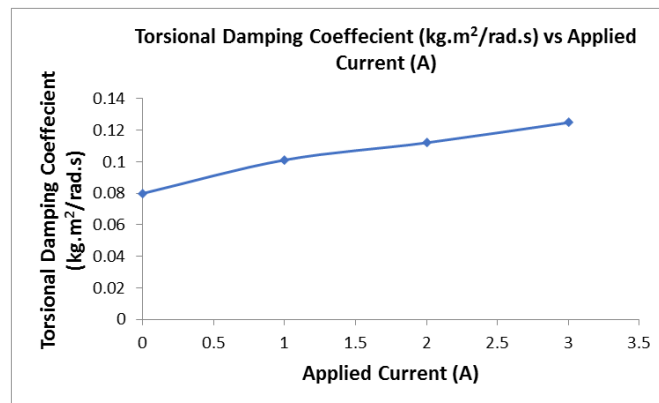
Figure 90. Damping coeffecients of MRE vs applied current.

Table 11. Summary of the Findings for the TTF Curves.

Applied current (A)	f_1 (Hz)	Natural frequency f_n (Hz)	f_2 (Hz)	Damping ratio	Critical damping (kg. m²/ rad. s)	Torsional damping coefficient (kg. m²/ rad. s)	Torsional stiffness (N.m/rad)
0	11.97	13.9	19.92	0.285971	0.279476	0.079922	12.2042
1	13.92	17.5	23.98	0.287429	0.351858	0.101134	19.344425
2	16.16	20	27.31	0.27875	0.402124	0.112092	25.266187
3	17.11	21.5	29.53	0.288837	0.432283	0.124859	29.198238

4.4.2 Continuous rotation test results

This test examined the MRE effect on torsional vibration isolation when the proposed drilling system is working. The methodology of this test was explained in details in Section 4.2.3. The data analysis methodology is illustrated in this section as it is a part of the results. The methodology of this test was to control the motor by the input voltage so that the drill string is rotating at a certain speed (RPM). The motor started to rotate when the voltage value is 5 V. this is due to the load of the system as it consisted of shafts, slip ring, MRE coupling and the disc attaching the drill bit. The increment which was taken in controlling the voltage was 0.25 V. The motor was controlled with a voltage range of 5 V – 7 V. The reason behind this specific range of input voltage is that the motor cannot reach the resonance frequency found in the impact test (13.9 Hz). The tachometer was used to measure the speed of the shaft. At each time, the applied current to the electromagnetic coil was varied too (0 A – 3 A). The relationship between the input voltage and the rotation of the shaft (RPM and frequency) is shown in Figure 91. The trend shows a direct relationship between the input voltage and the rotation of the shaft. The non-linearity relationship can be due to the sensitivity of the tachometer while measuring the RPM.
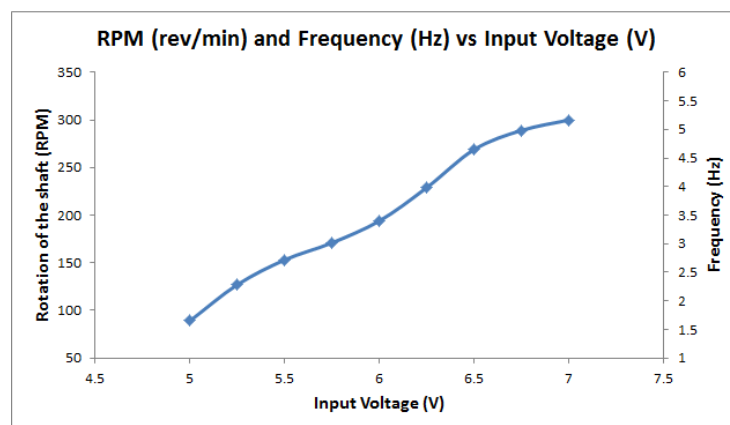
Figure 91. Rotation of the shaft vs input voltage.

After applying the test at each input voltage (fixed RPM), the readings of both accelerometers (acceleration vs time) were delivered to the DAQ and was extracted as a time domain. Using a MATLAB code, it converts the time domain data into a frequency domain using FFT. FFT plots were plotted for each value of the excitation frequency and the amplitude was noted at that certain frequency (frequency of rotation). However, the FFT plot presents the amplitude with respect to a range of frequencies. Finally, the ratio between the upper and lower accelerometers readings at that certain frequency is plotted with respect to it. Figure 92 shows the processing of the data analysis.
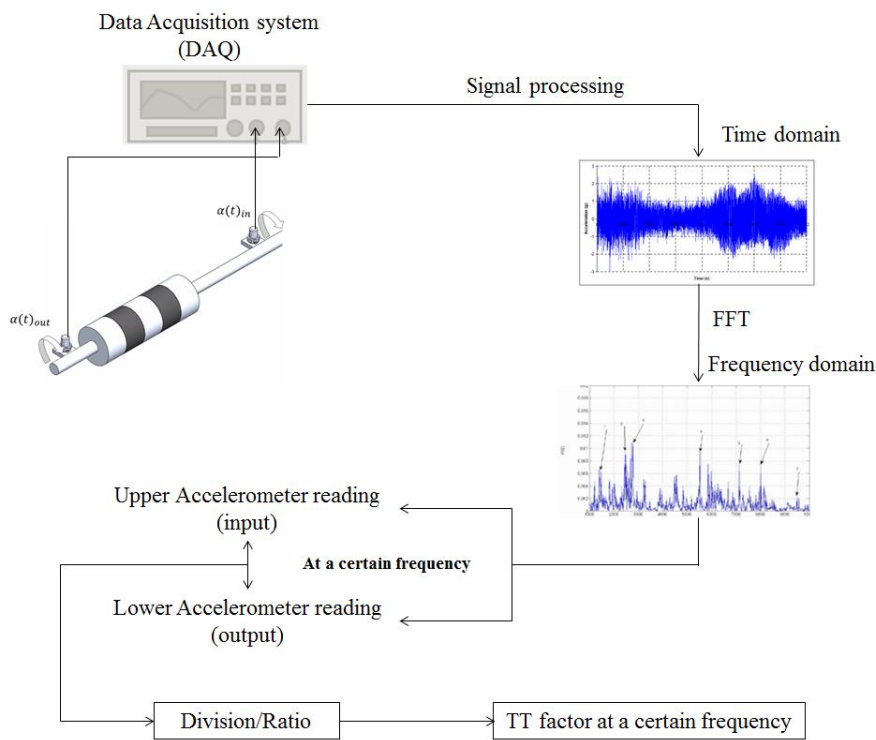
Figure 92. Signal processing and data analysis methodology in the continuous rotation results.

The signal processing of this test took the most of the time, because there were 72 different cases to analyze. This can be explained by the fact that at a certain excitation frequency, 2 readings are to be taken (upper and lower accelerometers).

Since the test was done for an increment of 0.25 V of the voltage supplied to the motor with a range of 5 V – 7 V. It means that 2 readings of the accelerometers are taken for 9 different increments of the input voltage (speed). Hence, 18 different readings were obtained. However, and knowing that there are 4 different values of the applied current (magnetic field), this test consisted of 72 cases to be analyzed.

The analysis started with obtaining the time domain. The amplitude of rotation for both readings initially was plotted against time in order to check the variety of results. Results show that the amplitude in both locations is different. Figure 93 shows the time domain of both accelerometers readings at an input voltage of 5V. These readings are the angular acceleration as explained previously. It is shown that there is a difference in the readings where the red spectrum shows the amplitude of the upper accelerometer amplitude and the blue spectrum represents the lower accelerometer amplitude. It is shown that the red spectrum overweighs the blue spectrum illustrating that the vibration is higher. In addition, the amplitude for the red spectrum is higher than the blue spectrum which can be observed as shown in Figure 93.
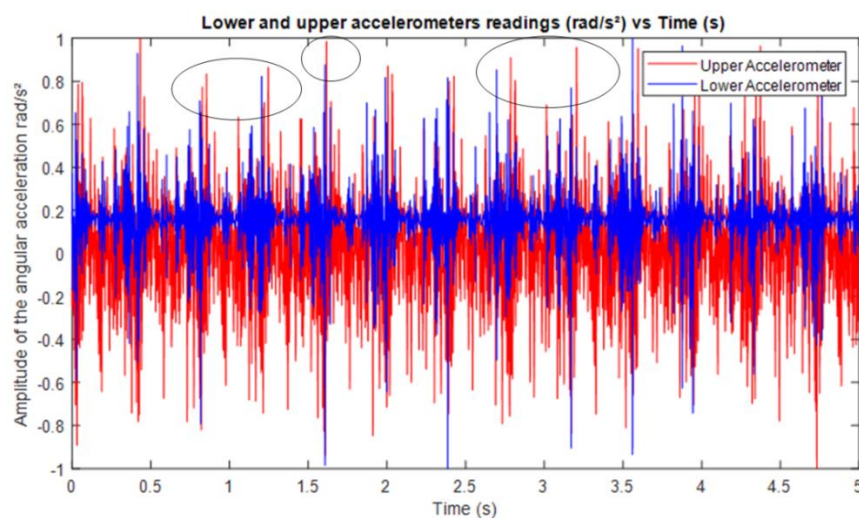
Figure 93. Time domain spectrum for the angular acceleration in upper and lower accelerometers.

After obtaining the time domain for both accelerometers readings for all 72 cases, FFT was used to convert the data from the time domain into the frequency domain. For a random example, for the time domains of both accelerometers for the case of 6.5 V applied voltage to the motor at a 3A applied current. Figure 94 shows the FFT results of the upper and lower accelerometers. The amplitude of the angular acceleration was taken at that certain frequency of rotation (6.5V input voltage results in a frequency of rotation of 4.48 Hz from Figure 94). Therefore, at this frequency, the amplitude is noted and these results for this specific case agree with the grey highlighted results as in Table 15. There is a minor difference between the frequency calculated using the tachometer (4.48 Hz) and the frequency shown in this example (4.30 Hz). This might be due to the uncertainties of the tachometer during measuring the RPM. Also, it can be due to resolution of the measurements.
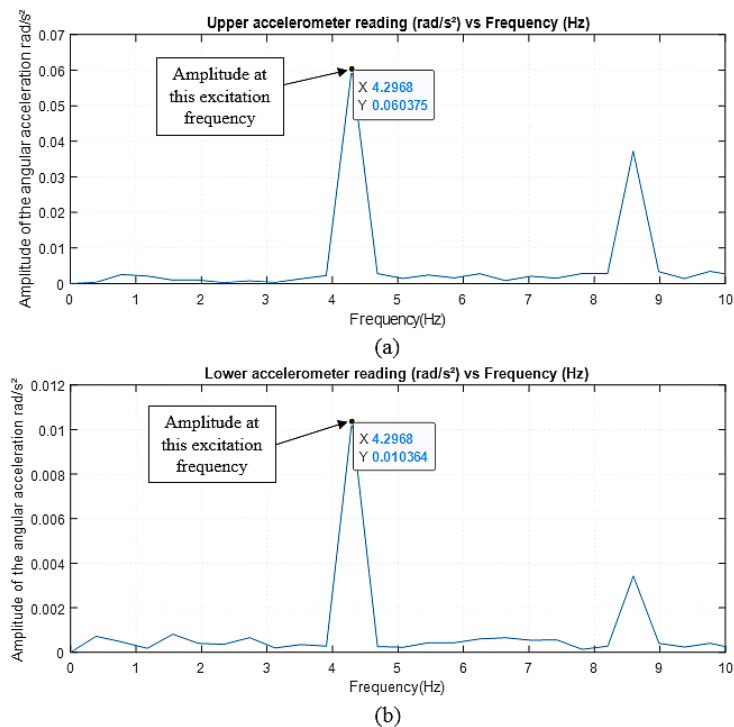
Figure 94. Amplitude of the (a) Upper and (b) lower, accelerometers readings at a rotation frequency 4.30 Hz.

Tables (12-15) show the readings of the upper and lower accelerometers readings at each excitation frequency for all ranges of applied current (0 A – 3 A) as well as the transmissibility factor between them. The speed of the shaft while rotating was converted to a frequency in Hz by dividing by 60. It can be obtained that the angular amplitude values are larger when the shaft is rotating before MRE. On the other hand, the angular amplitude values are lower after the presence of the MRE. This concludes that in the presence of MRE, the amplitude of the rotation is reduced. Therefore, MRE is able to damp and reduce torsional vibration of the drilling system while rotation.

Table 12. Data for Continuous Rotation Test at Applied Current of 0 A.

Voltage (V)	RPM (rev/min)	Frequency (Hz)	Upper accelerometer (rad/s^2)	Lower accelerometer (rad/s^2)	Angular transmissibility factor
5	89	1.483333	0.02518	0.0029308	0.116394
5.25	127	2.116667	0.020265	0.0034974	0.172583
5.5	153	2.55	0.0063735	0.00080949	0.127009
5.75	171	2.85	0.00085088	0.00069196	0.813229
6	194	3.233333	0.0037729	0.00097562	0.258586
6.25	229	3.816667	0.018012	0.0064085	0.355791
6.5	269	4.483333	0.010587	0.0030983	0.292651
6.75	289	4.816667	0.109903	0.027524	0.250439
7	300	5	0.0025829	0.00067834	0.262627

Table 13. Data for Continuous Rotation Test at Applied Current of 1 A.

Voltage (V)	RPM (rev/min)	Frequency (Hz)	Upper accelerometer (rad/s^2)	Lower accelerometer (rad/s^2)	Angular transmissibility factor
5	89	1.483333	0.034918	0.0027699	0.079326
5.25	127	2.116667	0.0065023	0.0010571	0.162573
5.5	153	2.55	0.00774	0.0013326	0.172171
5.75	171	2.85	0.0092163	0.00018067	0.019603
6	194	3.233333	0.050783	0.0038897	0.076595
6.25	229	3.816667	0.0034598	0.0026579	0.768224
6.5	269	4.483333	0.014929	0.0016495	0.11049
6.75	289	4.816667	0.0092847	0.0021741	0.234159
7	300	5	0.01504	0.0027437	0.182427

Table 14. Data for Continuous Rotation test at Applied Current of 2 A.

Voltage (V)	RPM (rev/min)	Frequency (Hz)	Upper accelerometer (rad/s^2)	Lower accelerometer (rad/s^2)	Angular transmissibility factor
5	89	1.483333	0.018535	0.0026409	0.169458
5.25	127	2.116667	0.017308	0.002442	0.141091
5.5	153	2.55	0.050283	0.0081796	0.162671
5.75	171	2.85	0.042952	0.0026609	0.061951
6	194	3.233333	0.0051019	0.00023316	0.045701
6.25	229	3.816667	0.036021	0.012729	0.353377
6.5	269	4.483333	0.0159511	0.011827	0.741454
6.75	289	4.816667	0.0088795	0.0021691	0.244282
7	300	5	0.055414	0.012566	0.226766

Table 15. Data for Continuous Rotation Test at Applied Current of 3 A.

Voltage (V)	RPM (rev/min)	Frequency (Hz)	Upper accelerometer (rad/s^2)	Lower accelerometer (rad/s^2)	Angular transmissibility factor
5	89	1.483333	0.054976	0.0023247	0.172231
5.25	127	2.116667	0.016091	0.0060893	0.108561
5.5	153	2.55	0.031937	0.012544	0.082561
5.75	171	2.85	0.036214	0.0084989	0.028692
6	194	3.233333	0.063721	0.034575	0.075237
6.25	229	3.816667	0.071684	0.035165	0.088331
6.5	269	4.483333	0.060375	0.010364	0.721526
6.75	289	4.816667	0.060375	0.015674	0.259611
7	300	5	0.064986	0.013543	0.208399

Table 12 represents the obtained data for the experiment when no magnetic field is applied. It is shown that the amplitude before and after the presence of the MRE is changing. For example, the amplitude of rotation (angular acceleration) for the upper accelerometer is $0.02518\ rad/s^2$ when frequency of rotation is 1.48 Hz. On the other hand, the amplitude reduces to $0.0029308\ rad/s^2$ after the presence of the MRE. It can be clearly seen that the amplitude of vibration before and after the MRE is different and hence, the vibration is reduced due to the stiffening effect of MRE.

Another conclusion is obtained which is the fact that MRE affects the whole system. The effect of the MRE is presented when the load is transmitted from the motor to the drill bit. In this case, the assumption made is that the drill string is rigid

which means that the upper accelerometer reading is the same as the output of the motor. From Tables (12-15), the angular acceleration values for the lower accelerometer at a frequency of rotation of 1.48 Hz for an applied current values of 0 A, 1 A, 2 A, and 3 A are $0.0029308\ rad/s^2$, $0.0027699\ rad/s^2$, $0.0026409\ rad/s^2$, and $0.0023247\ rad/s^2$, respectively. This illustrates that the MRE is able to reduce the amplitude of rotation at each time the magnetic field increases. It also means that MRE responded well to the magnetic field and it could reduce torsional vibration while rotation.

The readings of the upper and lower accelerometers are plotted against the range of frequencies in order to observe the effect of the MRE in vibration isolation. Figure 95 represents the angular acceleration for both accelerometers plotted against the range of the frequencies for different applied current supplied to the electromagnetic coil. It is found that the amplitude of rotation before the presence of MRE is higher than the amplitude of rotation after it. It is concluded that vibration (using the transmissibility analysis) in torsional mode is reduced by using the MRE in the proposed drilling system.

Similar trends are observed in Figure 95 for the readings of upper and lower accelerometers at a certain current applied. The amplitude of the upper accelerometer is higher than the amplitude of the lower accelerometer which shows that the rotation is more convenient and calm. This is due to the effect of the MRE on the shaft (drill string) while rotating which adjust the shaft in order not to rotate in a way creating vibration. It is concluded that utilizing MRE in torsional vibration is efficient and the amplitude of rotation is attenuated due to the increases of the stiffness of the MRE, hence, utilizing MRE in the proposed drilling application is sufficient to act as a semi-active vibration isolator.
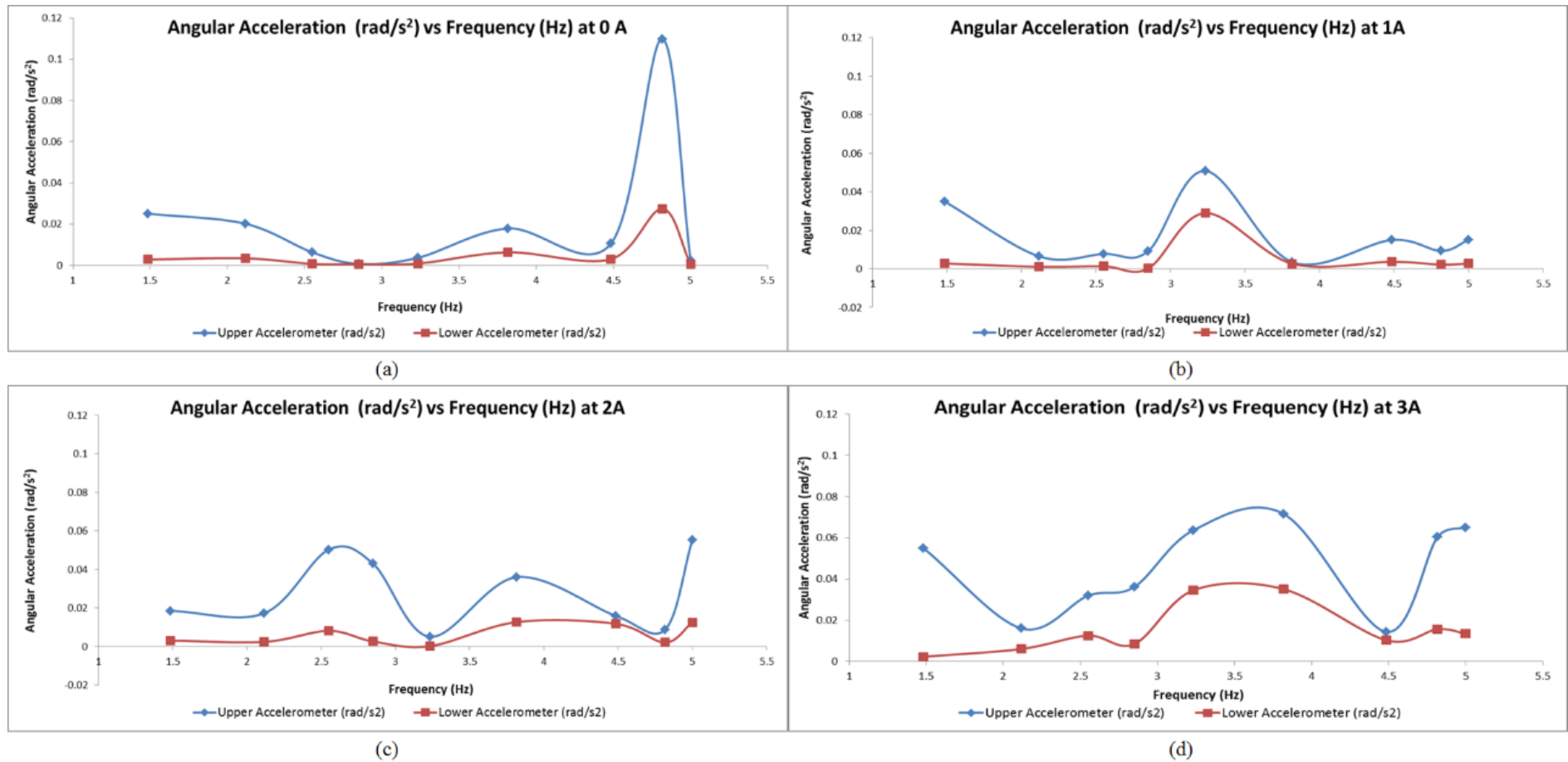
Figure 95. Angular acceleration for upper and lower accelerometers (before and after MRE) for applied current of (a) 0 A, (b) 1 A, (c) 2 A, and (d) 3 A.

Finally, the torsional transmissibility factor is plotted with respect to the frequency for all cases as in Figure 96. It is observed that the curves are being shifted to the right. This is due to the stiffening of the MRE when the applied current increases. The peak frequency in this case does not represent the resonance frequency because it was obtained from the impact test which was about 13.9 Hz. The peak in this case represents one of the frequencies during the rotation of the motor. The power supply unit used in this test has its maximum voltage output of 12 V; therefore, the resonance frequency of the system was not achieved. This test consisted of 72 different scenarios to analyze where in each case; data acquisition and processing were required. However, the shifting of the torsional transmissibility curves which is the core of this study shows that the MRE is being stiffer and torsional vibration isolation is possible. The peaks indicate that MRE damping properties changes slightly which agrees the literature and the impact test done previously.
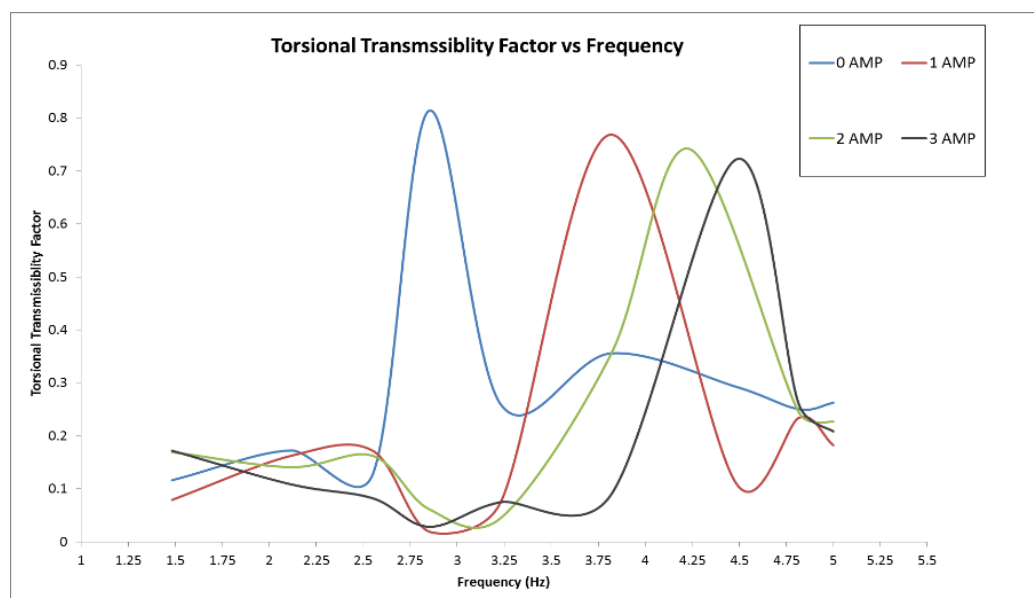
Figure 96. Torsional Transmissibility factor vs excitation frequency for the continuous rotation test.

Chapter 5: Conclusions and Future Works

Magnetorheological elastomers (MREs) are an evolving field. MRE is considered as a type of smart materials where its stiffness changes under a magnetic field. This study has introduced a semi-active vibration isolator utilizing MRE. The ideas highlighted in this work were divided mainly into two parts (computational and experimental). Firstly, two different computational studies were done on MRE in order to understand and investigate its rheological properties when exposed to a magnetic field. These studies aimed to test and verify the semi-active vibration isolation of MRE where its properties (mainly stiffness) can be controlled. Results of this work can contribute to develop a new way in vibration isolation using smart Martials (MRE). The experimental work can be improved to a larger scale so that drilling efficiency can be enhanced.

The first study was an analytical simulation of different MRE models on a base motion isolation (base excitation) system. Secondly, a numerical modeling and simulation was done on MRE in order to understand its characteristics by the influence of a magnetic field. Thirdly, the experimental developments started with MRE fabrication in order to be tested and studied. The experimental setup which was chosen in this study is drilling since drilling is being exposed to vibrations extensively. Conclusions are presented as follows:-

1. Analytical simulations of different MRE models:

The mathematical model was derived for base isolation system and was combined with the mathematical models of five different MREs for step and sinusoidal excitation inputs. It can be concluded from the analytical simulation study that different MRE models were able to reduce vibration in base isolation system. Bingham, Bouc-Wen, Modified Bouc-Wen, Dahl, and Hysteresis were modeled using

Simulink and MATLAB. Field-dependent parameters were identified by mathematical expressions. The stiffness and damping coefficients were approximated from the second order underdamped systems obtained from the step response. It can be clearly deduced that the change in the stiffness for these models are way more than the change in the damping properties. The change in the stiffness was found to be approximately 2 times higher than the change in the damping coefficient which confirms the literature survey. The transmissibility factor was calculated and plotted against a range of frequencies; results showed that there is a shift in the natural frequency of the system for all five models which is due to the change in the stiffness as the applied current is increased.

2. Numerical modeling of MRE:

MRE was modeled numerically using COMSOL Multiphysics software which was a cylindrical silicon rubber embedded with 12 iron particles. The 3D micro-scale FEA studied the field-stiffening properties of MRE in both linear and torsional modes. It was found that as the magnetic field increases, the deformation of the MRE decreases and reversely the stiffness increases. Similarly, the angular deformation (rotation) decreases as the magnetic field generated increases and this due to the increase of the torsional stiffness of MRE. When the 1st value of magnetic field applied, an increase of 28.75% and 20.12% of both linear and torsional stiffness was found, respectively. After that, the transmissibility analysis was performed in order to investigate the response of the MRE when it is excited by a linear/torsional load. It was observed that the transmissibility curve is shifted to the right as the magnetic field increases in both modes. In addition, the natural frequency of the system is increased. This concludes the fact that MRE is becoming stiffer. Finally, the minimum transmissibility factor in both modes is achieved which leads to vibration isolation.

3. Experimental developments:

Finally in this work, MRE samples were fabricated and cured in order to test it in vibration isolation. Drilling test rig was prototyped in order to utilize MRE as a semi-active vibration isolator in drilling for torsional mode of vibration. The mathematical model of the system was derived and the angular displacement transmissibility equation was obtained. Two tests were implemented on this system. The efficiency of the MRE was tested statically and dynamically and results revealed that MRE is able to isolate vibration in the torsional mode and it can be used in torsional vibration isolation in drilling process as proposed in this thesis. Impact hammer test was conducted in order to obtain the torsional transfer function (TTF) factor. It was found that the resonance frequency happens at a low range of frequencies which agrees with the literature that most rotary machines vibrate aggressively in low frequencies. The natural frequency of the system is shifted from 13.9 Hz to 17.5 Hz when the 1st magnetic field is generated. The change in the torsional stiffness of MRE was considerable as it increased from 12.2 N.m/rad (No current) to 29.2 N.m/rad when the current reached 3 A (12.38 mT of magnetic field). Results showed that the damping characteristics of MRE do not change much with magnetic field as it the damping coefficient changed from 0.079 $kg.m^2/rad.s$ to 0.12 $kg.m^2/rad.s$ when the when the current reached 3 A (12.38 mT of magnetic field).

The continuous rotation (dynamic test) was performed on the system at different frequencies. Results showed that there is a change in the angular acceleration amplitude before and after the presence of MRE. From time domain, it was shown that there is a difference in the readings and then using FFT, the frequency domain was obtained in order to catch the amplitudes at certain excitation frequencies. Results

showed that there is a vibration reduction by plotting the upper and lower accelerometers amplitudes while rotating at the same speed for each value of current applied. The transmissibility curves of these data were plotted and a shift in the curve was observed meaning that the stiffness of the MRE was increased by the influence of the magnetic field.

To sum up, the utilization of MRE as a torsional vibration isolator in drilling is possible and achieved. MRE efficiency was tested and results showed that its stiffness properties variation allow it to act as a vibration isolator in torsional mode. The novelty of this experimental work is using MRE in vibration isolation in drilling process as it can be beneficial for Oil and Gas industry by which the extraction of the natural resources from the ground can be developed as the lifetime of the drilling machines can be improved.

In future works and to support the conclusions stated in this work, the following can be done:-

- To study the MRE efficiency of MRE in axial and transverse modes of vibration during drilling which can support the obtained results.

- MRE can be tested on the same system while rotation using a motor which can provide more power to reach the resonance frequency.

- This work can be enhanced and improved by studying the efficiency of the MRE at higher applied current supplied to the electromagnetic coil.

- This experiment can be applied on a real drilling machine. In this research, the reason behind not apply it on a drilling machine is that there is no control on the input speed; therefore, the usage of the motor enabled the controlling of the input voltage. In addition, this can be practical by developing an electromagnetic coil within the coupling so that the magnetic field along the MRE can be enhanced as

well as it can be attached to the drill string while processing. For safety reasons, insulated materials should be used to avoid any sparks which can lead to explosions. Also, the accelerometers can be substituted with sensors to give response instead of using wires around the drill string.

- MRE can be modelled on a FEA software and a parametric analysis can be done by changing the particles size (PZ) and the volume fraction (VF). In addition, the number of the particles inside the MR elastomer can be varied in order to investigate the change in the MRE stiffness.

- The experimental setup can be improved in order to apply a load on the drill bit as a real drilling process and consider the friction torque on the mathematical model.

- To apply different data analysis method for the continuous rotation test along with the method used in this work (FFT) such as wavelet and fuzzy data analysis methods.

REFERENCES

[1]   "Demand for Smart Materials is Increasing, but so are Production Costs -
        Technavio." [Online]. Available: https://blog.technavio.com/blog/demand-for-
        smart-materials-is-increasing-but-so-are-production-costs. [Accessed: 05-Feb-
        2020].

[2]   M. R. Jolly, J. D. Carlson, B. C. Muñoz, and T. A. Bullions, "The
        Magnetoviscoelastic Response of Elastomer Composites Consisting of Ferrous
        Particles Embedded in a Polymer Matrix," *J. Intell. Mater. Syst. Struct.*, vol. 7,
        no. 6, pp. 613–622, Nov. 1996, doi: 10.1177/1045389X9600700601.

[3]   L. Chen, X. L. Gong, W. Q. Jiang, J. J. Yao, H. X. Deng, and W. H. Li,
        "Investigation on magnetorheological elastomers based on natural rubber," *J.
        Mater. Sci.*, vol. 42, no. 14, pp. 5483–5489, Jul. 2007, doi: 10.1007/s10853-
        006-0975-x.

[4]   A. K. Bastola and L. Li, "A new type of vibration isolator based on
        magnetorheological elastomer," *Mater. Des.*, vol. 157, pp. 431–436, Nov.
        2018, doi: 10.1016/j.matdes.2018.08.009.

[5]   S. B. Kumbhar, S. P. Chavan, and S. S. Gawade, "Adaptive tuned vibration
        absorber based on magnetorheological elastomer-shape memory alloy
        composite," *Mech. Syst. Signal Process.*, vol. 100, pp. 208–223, Feb. 2018, doi:
        10.1016/j.ymssp.2017.07.027.

[6]   I. Bica, "Magnetoresistor sensor with magnetorheological elastomers," *J. Ind.
        Eng. Chem.*, vol. 17, no. 1, pp. 83–89, Jan. 2011, doi:
        10.1016/j.jiec.2010.12.001.

[7]   Z. Xu, Q. Wang, K. Zhu, S. Jiang, H. Wu, and L. Yi, "Preparation and
        characterization of magnetorheological elastic polishing composites," *J. Intell.*

Mater. Syst. Struct., vol. 30, no. 10, pp. 1481–1492, Jun. 2019, doi: 10.1177/1045389X19835960.

[8] T. Liu and Y. Xu, "Magnetorheological Elastomers: Materials and Applications," in *Smart and Functional Soft Materials*, IntechOpen, 2019.

[9] A. Boczkowska and S. Awietj, "Microstructure and Properties of Magnetorheological Elastomers," in *Advanced Elastomers - Technology, Properties and Applications*, InTech, 2012.

[10] K. Danas, S. V. Kankanala, and N. Triantafyllidis, "Experiments and modeling of iron-particle-filled magnetorheological elastomers," *J. Mech. Phys. Solids*, vol. 60, no. 1, pp. 120–138, Jan. 2012, doi: 10.1016/j.jmps.2011.09.006.

[11] W. H. Li and M. Nakano, "Fabrication and characterization of PDMS based magnetorheological elastomers," *Smart Mater. Struct.*, vol. 22, no. 5, May 2013, doi: 10.1088/0964-1726/22/5/055035.

[12] M. Balasoiu, S. V. Kozhevnikov, Y. V. Nikitenko, G. E. Iacobescu, M. Bunoiu, and I. Bica, "Silicone rubber based magnetorheological elastomer: Magnetic structure tested by means of neutron depolarization and magnetic force microscopy methods," in *Journal of Physics: Conference Series*, 2017, vol. 848, no. 1, doi: 10.1088/1742-6596/848/1/012016.

[13] R. K. Shuib, K. L. Pickering, and B. R. Mace, "Dynamic properties of magnetorheological elastomers based on iron sand and natural rubber," *J. Appl. Polym. Sci.*, vol. 132, no. 8, p. n/a-n/a, Feb. 2015, doi: 10.1002/app.41506.

[14] J. E. Japka, "Microstructure and Properties of Carbonyl Iron Powder," *JOM*, vol. 40, no. 8, pp. 18–21, Aug. 1988, doi: 10.1007/BF03258115.

[15] D. Ghorbany and Daruish, "MR damper hysteresis characterization for the semi-active suspension system," *65*, pp. 1–65, 2011.

[16] "A REVIEW ON OPTIMIZATION OF CUTTING PARAMETERS IN DRILLING PROCESS," *Int. J. Adv. Eng. Res. Dev.*, vol. 4, no. 04, Apr. 2017, doi: 10.21090/ijaerd.51157.

[17] Y. Alsaffar, S. Sassi, and A. Baz, "Band gap characteristics of periodic gyroscopic systems," *J. Sound Vib.*, vol. 435, pp. 301–322, Nov. 2018, doi: 10.1016/j.jsv.2018.07.015.

[18] P. D. Spanos, A. K. Sengupta, R. A. Cunningham, and P. R. Paslay, "Modeling of roller cone bit liftoff dynamics in rotary drilling," *J. Energy Resour. Technol. Trans. ASME*, vol. 117, no. 3, pp. 197–207, 1995, doi: 10.1115/1.2835341.

[19] "Rao, Mechanical Vibrations in SI Units | Pearson." [Online]. Available: https://www.pearson.com/uk/educators/higher-education-educators/product/Rao-Mechanical-Vibrations-in-SI-Units-5th-Edition/9789810687120.html. [Accessed: 05-Feb-2020].

[20] "ACTIVE VIBRATION CONTROL Professor Mike Brennan Institute of Sound and Vibration Research University of Southampton, UK. - ppt video online download." [Online]. Available: https://slideplayer.com/slide/1498484/. [Accessed: 05-Feb-2020].

[21] S. Segla, "Modelling and Optimization of Passive and Semi-active Suspension of a 3 DOF Seat Platform," in *Mechanisms and Machine Science*, vol. 73, Springer Netherlands, 2019, pp. 4075–4084.

[22] N. Alujević, D. Čakmak, H. Wolf, and M. Jokić, "Passive and active vibration isolation systems using inerter," *J. Sound Vib.*, vol. 418, pp. 163–183, Mar. 2018, doi: 10.1016/j.jsv.2017.12.031.

[23] H. P. Mei, H. Y. Tian, and S. Huang, "Recent study on the passive and active

vibration isolators," in *Applied Mechanics and Materials*, 2014, vol. 494–495, pp. 491–496, doi: 10.4028/www.scientific.net/AMM.494-495.491.

[24] A. L. Morales, A. J. Nieto, J. M. Chicharro, and P. Pintado, "A semi-active vehicle suspension based on pneumatic springs and magnetorheological dampers," *J. Vib. Control*, vol. 24, no. 4, pp. 808–821, Feb. 2018, doi: 10.1177/1077546316653004.

[25] H. Wen, J. Guo, Y. Li, Y. Liu, and K. Zhang, "The transmissibility of a vibration isolation system with ball-screw inerter based on complex mass," *J. Low Freq. Noise, Vib. Act. Control*, vol. 37, no. 4, pp. 1097–1108, Dec. 2018, doi: 10.1177/1461348418769650.

[26] C. de Silva, "Vibration Fundamentals and Practice, Second Edition," in *Vibration*, CRC Press, 2006, pp. 301–384.

[27] R. A. Ibrahim, "Recent advances in nonlinear passive vibration isolators," *Journal of Sound and Vibration*, vol. 314, no. 3–5. pp. 371–452, 22-Jul-2008, doi: 10.1016/j.jsv.2008.01.014.

[28] B. Yang, "Vibration Isolation - an overview | ScienceDirect Topics," 2005. [Online].Available:https://www.sciencedirect.com/topics/engineering/vibration -isolation. [Accessed: 06-Feb-2020].

[29] Y. E. Lage, M. M. Neves, N. M. M. Maia, and D. Tcherniak, "Force transmissibility versus displacement transmissibility," *J. Sound Vib.*, vol. 333, no. 22, pp. 5708–5722, Oct. 2014, doi: 10.1016/j.jsv.2014.05.038.

[30] J. Rabinow, "The Magnetic Fluid Clutch," *Trans. Am. Inst. Electr. Eng.*, vol. 67, pp. 1308–1315, 1948, doi: 10.1109/T-AIEE.1948.5059821.

[31] M. Lokander and B. Stenberg, "Performance of isotropic magnetorheological rubber materials," *Polym. Test.*, vol. 22, no. 3, pp. 245–251, May 2003, doi:

10.1016/S0142-9418(02)00043-0.

[32] M. Kallio, "The elastic and damping properties of magnetorheological elastomers," 2005.

[33] "nn Schubert, G., and Harrison, P. (2015) Large-strain behaviour of Magneto-Rheological Elastomers tested under uniaxial compression and tension, and pure shear deformations.Polymer Testing, 42. pp. 122-134."

[34] "Magnetorheological Dampers," in *Semi-active Suspension Control*, Springer London, 2008, pp. 165–217.

[35] C. Ruddy, E. Ahearne, and G. Byrne, "A review of Magnetorheological Elastomers: Properties and Applications," 2012.

[36] "Usman, M., & Jung, H.-J. . Recent developments of magneto-rheologicalelastomers for civil engineering applications, 2015."

[37] M. R. Jolly, J. D. Carlson, and B. C. Muñoz, "A model of the behaviour of magnetorheological materials," *Smart Mater. Struct.*, vol. 5, no. 5, pp. 607–614, Oct. 1996, doi: 10.1088/0964-1726/5/5/009.

[38] L. Chen and X. L. Gong, "Damping of magnetorheological elastomers," *J. Cent. South Univ. Technol. (English Ed.*, vol. 15, no. 1 SUPPL., pp. 271–274, Jan. 2008, doi: 10.1007/s11771-008-0361-8.

[39] T. L. Sun, X. L. Gong, W. Q. Jiang, J. F. Li, Z. B. Xu, and W. H. Li, "Study on the damping properties of magnetorheological elastomers based on cis-polybutadiene rubber," *Polym. Test.*, vol. 27, no. 4, pp. 520–526, Jun. 2008, doi: 10.1016/j.polymertesting.2008.02.008.

[40] Z. Varga, G. Filipcsei, and M. Zrínyi, "Smart composites with controlled anisotropy," *Polymer (Guildf).*, vol. 46, no. 18, pp. 7779–7787, Aug. 2005, doi: 10.1016/j.polymer.2005.03.102.

[41] J. Winger, M. Schümann, A. Kupka, and S. Odenbach, "Influence of the particle size on the magnetorheological effect of magnetorheological elastomers," *J. Magn. Magn. Mater.*, vol. 481, no. December 2018, pp. 176–182, 2019, doi: 10.1016/j.jmmm.2019.03.027.

[42] M. Kukla, J. Górecki, I. Malujda, K. Talaśka, and P. Tarkowski, "The Determination of Mechanical Properties of Magnetorheological Elastomers (MREs)," in *Procedia Engineering*, 2017, vol. 177, pp. 324–330, doi: 10.1016/j.proeng.2017.02.233.

[43] Y. Han, W. Hong, and L. E. Faidley, "Field-stiffening effect of magneto-rheological elastomers," *Int. J. Solids Struct.*, vol. 50, no. 14–15, pp. 2281–2288, Jul. 2013, doi: 10.1016/j.ijsolstr.2013.03.030.

[44] N. F. Alias, A. G. A. Muthalif, K. A. M. Arpan, and N. H. D. Nordin, "Experimental investigation of static properties of magnetorheological elastomer," *Iran. J. Sci. Technol. - Trans. Mech. Eng.*, vol. 42, no. 2, pp. 185–197, 2018, doi: 10.1007/s40997-017-0081-5.

[45] D. Gorman, S. Jerrams, R. Ekins, and N. Murphy, "Magnetic Field Design Reliable Data for Magnetic Field Design in Magnetorheological Elastomer Damping Applications is Essential for Accurate and Cost- …," pp. 20–22, 2012.

[46] G. M. Kamath and N. M. Wereley, "A nonlinear viscoelastic-plastic model for electrorheological fluids," *Smart Mater. Struct.*, vol. 6, no. 3, pp. 351–359, 1997, doi: 10.1088/0964-1726/6/3/012.

[47] S. Soltane, S. Montassar, O. Ben Mekki, and R. El Fatmi, "A hysteretic bingham model for MR dampers to control cable vibrations," *J. Mech. Mater. Struct.*, vol. 10, no. 2, pp. 195–206, 2015, doi: 10.2140/jomms.2015.10.195.

[48]   N. Roussel, C. Lanos, and Z. Toutou, "Identification of Bingham fluid flow parameters using a simple squeeze test," *J. Nonnewton. Fluid Mech.*, vol. 135, no. 1, pp. 1–7, Apr. 2006, doi: 10.1016/j.jnnfm.2005.12.001.

[49]   B. F. Spencer, S. J. Dyke, M. K. Sain, and J. D. Carlson, "Phenomenological Model for Magnetorheological Dampers," *J. Eng. Mech.*, vol. 123, no. 3, pp. 230–238, Mar. 1997, doi: 10.1061/(ASCE)0733-9399(1997)123:3(230).

[50]   P. Krauze and J. Kasprzyk, "Vibration control in quarter-car model with magnetorheological dampers using FxLMS algorithm with preview," in *2014 European Control Conference, ECC 2014*, 2014, pp. 1005–1010, doi: 10.1109/ECC.2014.6862553.

[51]   X. Zhu and X. Lu, "Parametric identification of Bouc-Wen model and its application in mild steel damper modeling," in *Procedia Engineering*, 2011, vol. 14, pp. 318–324, doi: 10.1016/j.proeng.2011.07.039.

[52]   M. K. M. Razali, A. G. A. Muthalif, and N. H. D. Nordin, "Estimation of Parameter for Different Magnetorheological Fluids Model for Varying Current," *Int. J. Comput. Electr. Eng.*, vol. 10, no. 2, pp. 127–134, 2018, doi: 10.17706/ijcee.2018.10.2.127-134.

[53]   P. K. R. Dasari *et al.*, "Adaptation of the modified Bouc-Wen model to compensate for hysteresis in respiratory motion for the list-mode binning of cardiac SPECT and PET acquisitions: Testing using MRI," *Med. Phys.*, vol. 41, no. 11, Nov. 2014, doi: 10.1118/1.4895845.

[54]   P. R. Dahl, "Solid friction damping of mechanical vibrations," *AIAA J.*, vol. 14, no. 12, pp. 1675–1682, 1976, doi: 10.2514/3.61511.

[55]   D. H. Wang and W. H. Liao, "Magnetorheological fluid dampers: A review of parametric modelling," *Smart Materials and Structures*, vol. 20, no. 2. Feb-

2011, doi: 10.1088/0964-1726/20/2/023001.

[56] K. Augustynek and A. Urbaś, "Comparison of bristles' friction models in dynamics analysis of spatial linkages," *Mech. Res. Commun.*, Apr. 2016, doi: 10.1016/j.mechrescom.2017.01.003.

[57] A. Urbaś, "Application of the Dahl friction model in the dynamics analysis of grab cranes," in *MATEC Web of Conferences*, 2016, vol. 83, doi: 10.1051/matecconf/20168303008.

[58] J. Li, Y. Li, W. Li, and B. Samali, "Development of adaptive seismic isolators for ultimate seismic protection of civil structures," in *Sensors and Smart Structures Technologies for Civil, Mechanical, and Aerospace Systems*, 2013, vol. 8692, pp. 1-12, doi: 10.1117/12.2009626.

[59] Y. Yu, Y. Li, and J. Li, "Parameter identification of a novel strain stiffening model for magnetorheological elastomer base isolator utilizing enhanced particle swarm optimization," *J. Intell. Mater. Syst. Struct.*, vol. 26, no. 18, pp. 2446–2462, Dec. 2015, doi: 10.1177/1045389X14556166.

[60] Y. Yu, Y. Li, and J. Li, "A new hysteretic model for magnetorheological elastomer base isolator and parameter identification based on modified artificial fish swarm algorithm," *31st Int. Symp. Autom. Robot. Constr. Mining, ISARC 2014 - Proc.*, no. Isarc, pp. 176–183, 2014, doi: 10.22260/isarc2014/0024.

[61] Y. Yu, Y. Li, and J. Li, "Parameter identification and sensitivity analysis of an improved LuGre friction model for magnetorheological elastomer base isolator," *Meccanica*, vol. 50, no. 11, pp. 2691–2707, Nov. 2015, doi: 10.1007/s11012-015-0179-z.

[62] D. Y. Meng, G. L. Tao, H. Liu, and J. F. Chen, "Analysis of friction

characteristics of pneumatic cylinders based on LuGre model," *Zhejiang Daxue Xuebao (Gongxue Ban)/Journal Zhejiang Univ. (Engineering Sci.*, vol. 46, no. 6, pp. 1027–1033, Jun. 2012, doi: 10.3785/j.issn.1008-973X.2012.06.011.

[63]   S. Eshkabilov, "Modeling and simulation of non-linear and hysteresis behavior of magneto-rheological dampers in the example of quarter-car model," *Inernational Journal of Theoretical and Applied Mathematics ., vol. 2, no. 2, pp. 170-189,* 2016, doi:

10.11648/j.ijtam.20160202.32.

[64]   R. Stanway, J. L. Sproston, and N. G. Stevens, "Non-linear modelling of an electro-rheological vibration damper," *J. Electrostat.*, vol. 20, no. 2, pp. 167–184, 1987, doi: 10.1016/0304-3886(87)90056-8.

[65]   X. Gu, Y. Yu, J. Li, and Y. Li, "Semi-active control of magnetorheological elastomer base isolation system utilising learning-based inverse model," *J. Sound Vib.*, vol. 406, pp. 346–362, Oct. 2017, doi: 10.1016/j.jsv.2017.06.023.

[66]   F. C. L. Almeida, M. J. Brennan, A. T. Paschoalini, V. M. Santos, F. S. Bellucci, and A. E. Job, "An analytical investigation into the use of magneto-rheological elastomers to suppress flexural waves in beams," in *Procedia Engineering*,   2017,   vol.   199,   pp.   1338–1343,   doi: 10.1016/j.proeng.2017.09.342.

[67]   M. Behrooz, X. Wang, and F. Gordaninejad, "Performance of a new magnetorheological elastomer isolation system," *Smart Mater. Struct.*, vol. 23, no. 4, 2014, doi: 10.1088/0964-1726/23/4/045014.

[68]   F. Bolat and S. Sivrioglu, "Active Control of a Small-Scale Wind Turbine Blade Containing Magnetorheological Fluid," *Micromachines*, vol. 9, no. 2, p. 80, Feb. 2018, doi: 10.3390/mi9020080.

[69] J. M. Ginder, M. E. Nichols, L. D. Elie, and S. M. Clark, "Controllable-stiffness components based on magnetorheological elastomers," 2000, p. 418, doi: 10.1117/12.388844.

[70] G. J. Liao, X.-L. Gong, S. H. Xuan, C. J. Kang, and L. H. Zong, "Development of a real-time tunable stiffness and damping vibration isolator based on magnetorheological elastomer," *J. Intell. Mater. Syst. Struct.*, vol. 23, no. 1, pp. 25–33, Jan. 2012, doi: 10.1177/1045389X11429853.

[71] H. Du, W. Li, and N. Zhang, "Semi-active variable stiffness vibration control of vehicle seat suspension using an MR elastomer isolator," *Smart Mater. Struct.*, vol. 20, no. 10, Oct. 2011, doi: 10.1088/0964-1726/20/10/105003.

[72] W. Li, X. Zhang, and H. Du, "Development and simulation evaluation of a magnetorheological elastomer isolator for seat vibration control," *J. Intell. Mater. Syst. Struct.*, vol. 23, no. 9, pp. 1041–1048, Jun. 2012, doi: 10.1177/1045389X11435431.

[73] M. Behrooz, X. Wang, and F. Gordaninejad, "Modeling of a new semi-active/passive magnetorheological elastomer isolator," *Smart Mater. Struct.*, vol. 23, no. 4, 2014, doi: 10.1088/0964-1726/23/4/045013.

[74] W. M. R. W. Marzuki, A. G. A. Muthalif, and N. H. D. Nordin, "Semi-active torsional vibration isolation utilizing magnetorheological elastomer," *Vib. Phys. Syst.*, vol. 29, pp. 2–9, 2018.

[75] H. A. Hashi, A. G. A. Muthalif, and N. H. Diyana Nordin, "Dynamic tuning of torsional transmissibility using magnetorheological elastomer: Modelling and experimental verification," *Iran. J. Sci. Technol. - Trans. Mech. Eng.*, vol. 40, no. 3, pp. 181–187, 2016, doi: 10.1007/s40997-016-0024-6.

[76] B. Zhu, *The Finite Element Method: Fundamentals and Applications in Civil,*

Hydraulic, Mechanical and Aeronautical Engineering. Singapore: wiley, 2017.

[77] Y. Li and J. Li, "Finite element design and analysis of adaptive base isolator utilizing laminated multiple magnetorheological elastomer layers," in *Journal of Intelligent Material Systems and Structures*, 2015, vol. 26, no. 14, pp. 1861–1870, doi: 10.1177/1045389X15580654.

[78] S. Sun, X. Peng, and Z. Guo, "Study on macroscopic and microscopic mechanical behavior of magnetorheological elastomers by representative volume element approach," *Adv. Condens. Matter Phys.*, vol. 2014, 2014, doi: 10.1155/2014/232510.

[79] G. Schubert and P. Harrison, "Large-strain behaviour of Magneto-Rheological Elastomers tested under uniaxial compression and tension, and pure shear deformations," *Polym. Test.*, vol. 42, pp. 122–134, 2015, doi: 10.1016/j.polymertesting.2015.01.008.

[80] J. Roche, P. von Lockette, and S. Lofland, "Study of Hard-and Soft-Magnetorheological Elastomers (MRE ' s) Actuation Capabilities," *COMSOL Conf. Bost.*, vol. 05, p. 7, 2011.

[81] K. Haldar, B. Kiefer, and A. Menzel, "Finite element simulation of rate-dependent magneto-active polymer response," *Smart Mater. Struct.*, vol. 25, no. 10, Sep. 2016, doi: 10.1088/0964-1726/25/10/104003.

[82] Y. Li and J. Li, "Finite element design and analysis of adaptive base isolator utilizing laminated multiple magnetorheological elastomer layers," in *Journal of Intelligent Material Systems and Structures*, 2015, vol. 26, no. 14, pp. 1861–1870, doi: 10.1177/1045389X15580654.

[83] S. B. Kumbhar and S. S. Gawade, "Lateral vibration control of a drill by using MR elastomer," *Int. J. Eng. Res. Technol.*, vol. 1, no. 5, pp. 1–5, 2012.

[84] Y. Alsaffar, S. Sassi, and A. Baz, "Band Gap Characteristics of Nonrotating Passive Periodic Drill String," *J. Vib. Acoust.*, vol. 140, no. 2, Apr. 2018, doi: 10.1115/1.4037851.

[85] F. A. Majeed, M. Karkoub, H. Karki, and Y. L. A. Magid, "Drill Bit Whirl Mitigation Analysis – An Under Actuated System Perspective," *Int. J. Sustain. Energy Dev.*, vol. 1, no. 2, pp. 36–40, 2012, doi: 10.20533/ijsed.2046.3707.2012.0006.

[86] J. J. Rajnauth and T. Jagai, "Reduce Torsional Vibration and Improve Drilling Operations," *Proc. SPE Lat. Am. Caribb. Pet. Eng. Conf.*, no. January, pp. 1036–1047, 2003, doi: 10.2523/81174-ms.

[87] M. Oliveira and D. Vran, "Underdamped Second-Order Systems Overshoot Control," no. 3, 2012.

[88] A. Dargahi, R. Sedaghati, and S. Rakheja, "On the properties of magnetorheological elastomers in shear mode: Design, fabrication and characterization," *Compos. Part B Eng.*, vol. 159, pp. 269–283, Feb. 2019, doi: 10.1016/j.compositesb.2018.09.080.

[89] W. H. Li, Y. Zhou, and T. F. Tian, "Viscoelastic properties of MR elastomers under harmonic loading," *Rheol Acta*, vol. 49, pp. 733–740, 2010, doi: 10.1007/s00397-010-0446-9.

[90] "COMSOL Multiphysics® v. 5.4. www.comsol.com. COMSOL AB, Stockholm, Sweden." .

[91] L. C. Davis, "Model of magnetorheological elastomers," *J. Appl. Phys.*, vol. 85, no. 6, pp. 3348–3351, Mar. 1999, doi: 10.1063/1.369682.

[92] "How to Inspect Your Mesh in COMSOL Multiphysics® | COMSOL Blog." [Online]. Available: https://www.comsol.com/blogs/how-to-inspect-your-

mesh-in-comsol-multiphysics/. [Accessed: 15-Jan-2020].

[93] R. A. Shanks and I. Kong, "General Purpose Elastomers: Structure, Chemistry, Physics and Performance," 2013, pp. 11–45.

[94] S. K. Praveen, S. A. R. Kuchibhatla, A. K. Singh, and K. V. Gangadharan, "Performance of magnetorheological elastomer based torsional vibration isolation system for dynamic loading conditions," *J. Cent. South Univ.*, vol. 27, no. 1, pp. 144–154, Jan. 2020, doi: 10.1007/s11771-020-4284-3.

[95] G. W. Kim and S. C. Shin, "Research on the torque transmissibility of the passive torsional vibration isolator in an automotive clutch damper," *Proc. Inst. Mech. Eng. Part D J. Automob. Eng.*, vol. 229, no. 13, pp. 1840–1847, 2015, doi: 10.1177/0954407015579296.

[96] J. Laury, L. Abrahamsson, and M. Bollen, "Impact of reduced share of rotary frequency converters in a low frequency synchronous railway grid: A transient stability study," in *2019 Joint Rail Conference, JRC 2019*, 2019, doi: 10.1115/JRC2019-1238.

Appendix A: Analytical Simulations

MATLAB codes for calculating MRE models parameters and to simulate SIMULINK block diagram models in order to obtain stiffness, damping coefficients values and displacement transmissibility curves

- Bingham Model

```
%Current iterations
i = 0:1:4;

%Bingham model parameters
%Field-dependent Equations
[co]=147.5*i+13.52 %[N.s/m]
[fc]=-394.8*i+38.14 %[N]
[fo]=663.56*i+52.19 %[N]

%Opening and simulating the slx files 'Simulink models'
open('Bingham.slx')
open('BinghamK.slx')
sim('Bingham.slx')
sim('BinghamK.slx')

%Getting Tp and %PO
open('PO_Bingham');
open('tp_Bingham');

PO= PO_Bingham;
tp= tp_Bingham;

%Loop to calculate all parameters
for s = 1:1:5
    zzeta (s) =
(abs(log(PO(s)/100)))/(sqrt((pi^2)+(log(PO(s)/100))^2))
    Wn (s) = pi./(tp(s)*sqrt(1-zzeta(s)^2));
    kmre (s) = Wn(s)^2.*m;
    cc(s)=sqrt(4*kmre(s)*m)
    cmre (ss) = zzeta(ss)*cc(ss));
end

%Transmissibility curves for different currents
w= 0:1:100;

for i=1:length(kmre)
    for j=1:length(w)

        num(i,j)= ((kmre(i))^2 +(((cmre(i))^2)*(w(j)^2)));
        den(i,j)= (((cmre(i))^2)*(w(j)^2))+(((kmre(i))+((-
m)*(w(j)^2)))^2);
        T(i,j)= (sqrt((num(i,j)/den(i,j))));

    end
end
```

```matlab
plot(w,T,'Linewidth',2)
xlabel('Frequency (rad/s)')
ylabel('Displacement Transmissiblity (X/Y)')
legend('I = 0','I = 1','I = 2','I = 3','I = 4')
title('Displacement Transmissiblity (X/Y) vs Frequency (?) for
Bingham model')
```

- BW Model

```matlab
%Current iterations
i = 0:1:4;

% BW model parameters
%Constants
A = 301
B = 3630000 %[m^-2]
gamma = 190 %[s^-1]
n = 2
k_oa=469 %[N/m]
k_ob=323.2 %[N/m.A]
c_oa=2100 %[N.s/m]
c_ob=350 %[N.s/m.A]
alpha_oa=14000 %[N/m]
alpha_ob=69500 %[N/m.A]

%Field-dependent Equations
[ko]=k_oa+k_ob*i %[N/m]
[co]=c_oa+c_ob*i %[N.s/m]
[alpha]=alpha_oa+alpha_ob*i %[N/m]

%Opening and simulating the slx files 'Simulink models'
open('BW.slx')
open('BWK.slx')
sim('BW.slx')
sim('BWK.slx')

%Getting Tp and %PO
open('PO_BW');
open('tp_BW');

PO= PO_BW;
tp= tp_BW;

%Loop to calculate all parameters
for s = 1:1:5
    zzeta (s) =
(abs(log(PO(s)/100)))/(sqrt((pi^2)+(log(PO(s)/100))^2))
    Wn (s) = pi./(tp(s)*sqrt(1-zzeta(s)^2));
    kmre (s) = Wn(s)^2.*m;
    cc(s)=sqrt(4*kmre(s)*m)
    cmre (ss) = zzeta(ss)*cc(ss));
end

%Transmissibility curves for different currents
w= 0:1:100;

for i=1:length(kmre)
    for j=1:length(w)
```

```
        num(i,j)= ((kmre(i))^2 +(((cmre(i))^2)*(w(j)^2)));
        den(i,j)= (((cmre(i))^2)*(w(j)^2))+(((kmre(i))+((-
m)*(w(j)^2)))^2);
        T(i,j)= (sqrt((num(i,j)/den(i,j))));

    end
end

plot(w,T,'Linewidth',2)
xlabel('Frequency (rad/s)')
ylabel('Displacement Transmissiblity (X/Y)')
legend('I = 0','I = 1','I = 2','I = 3','I = 4')
title('Displacement Transmissiblity (X/Y) vs Frequency (?) for BW
model')
```

- MBW Model

```
%Current iterations
i = 0:1:4;

%MBW model parameters
%Constants
A = 301
B = 3630000 %[m^-2]
gamma = 190 %[s^-1]
n = 2
k_oa=500 %[N/m]
k_ob=15.9 %[N/m.A]
k_1a=469 %[N/m]
k_1b=323.2 %[N/m.A]
c_oa=2100 %[N.s/m]
c_ob=350 %[N.s/m.A]
c_1a=28300 %[N.s/m]
c_1b=295 %[N.s/m.A]
alpha_oa=14000 %[N/m]
alpha_ob=69500 %[N/m.A]

%Field-dependent Equations
[ko]=k_oa+k_ob*i %[N/m]
[k1]=k_1a+k_1b*i %[N/m]
[co]=c_oa+c_ob*i %[N.s/m]
[c1]=c_1a+c_1b*i %[N.s/m]
[alpha]=alpha_oa+alpha_ob*i %[N/m]


%Opening and simulating the slx files 'Simulink models'
open('MBW.slx')
open('MBWK.slx')
sim('MBW.slx')
sim('MBWK.slx')

%Getting Tp and %PO
open('PO_MBW');
open('tp_MBW');

PO= PO_MBW;
tp= tp_MBW;
```

```matlab
%Loop to calculate all parameters
for s = 1:1:5
    zzeta (s) =
(abs(log(PO(s)/100)))/(sqrt((pi^2)+(log(PO(s)/100))^2))
    Wn (s) = pi./(tp(s)*sqrt(1-zzeta(s)^2));
    kmre (s) = Wn(s)^2.*m;
    cc(s)=sqrt(4*kmre(s)*m)
    cmre (ss) = zzeta(ss)*cc(ss));
end

%Transmissibility curves for different currents
w= 0:1:100;

for i=1:length(kmre)
    for j=1:length(w)

        num(i,j)= ((kmre(i))^2 +(((cmre(i))^2)*(w(j)^2)));
        den(i,j)= (((cmre(i))^2)*(w(j)^2))+(((kmre(i))+((-
m)*(w(j)^2)))^2);
        T(i,j)= (sqrt((num(i,j)/den(i,j))));

    end
end

plot(w,T,'Linewidth',2)
xlabel('Frequency (rad/s)')
ylabel('Displacement Transmissiblity (X/Y)')
legend('I = 0','I = 1','I = 2','I = 3','I = 4')
title('Displacement Transmissiblity (X/Y) vs Frequency (?) for MBW
model')
```

- Dahl Model

```matlab
%Current iterations
i = 0:1:4;

% Dahl model parameters
%Constants
roh =25 %[kg/m^3]
k_oa=800 %[N/m]
k_ob=2520 %[N/m.A]
c_oa=24.64 %[N.s/m]
c_ob=40.41 %[N.s/m.A]
sigma_oa=0.031
sigma_ob=1.12

%Field-dependent Equations
[ko]=k_oa+k_ob*i %[N/m]
[co]=c_oa+c_ob*i %[N.s/m]
[sigma]=sigma_oa+sigma_ob*i

%Opening and simulating the slx files 'Simulink models'
open('Dahl.slx')
open('DahlK.slx')
sim('Dahl.slx')
sim('DahlK.slx')

%Getting Tp and %PO
open('PO_Dahl');
```

```matlab
open('tp_Dahl');

PO= PO_Dahl;
tp= tp_Dahl;

%Loop to calculate all parameters
for s = 1:1:5
    zzeta (s) =
(abs(log(PO(s)/100)))/(sqrt((pi^2)+(log(PO(s)/100))^2))
    Wn (s) = pi./(tp(s)*sqrt(1-zzeta(s)^2));
    kmre (s) = Wn(s)^2.*m;
    cc(s)=sqrt(4*kmre(s)*m)
    cmre (ss) = zzeta(ss)*cc(ss));
end

%Transmissibility curves for different currents
w= 0:1:100;

for i=1:length(kmre)
    for j=1:length(w)

        num(i,j)= ((kmre(i))^2 +(((cmre(i))^2)*(w(j)^2)));
        den(i,j)= (((cmre(i))^2)*(w(j)^2))+(((kmre(i))+((-
m)*(w(j)^2)))^2);
        T(i,j)= (sqrt((num(i,j)/den(i,j))));

    end
end

plot(w,T,'Linewidth',2)
xlabel('Frequency (rad/s)')
ylabel('Displacement Transmissiblity (X/Y)')
legend('I = 0','I = 1','I = 2','I = 3','I = 4')
title('Displacement Transmissiblity (X/Y) vs Frequency (?) for Dahl
model')
```

- Hysteresis Model

```matlab
%Current iterations
i = 0:1:4;

% Hysteresis model parameters
%Constants
k_oa=246.7 %[N/m]
k_ob=31.2 %[N/m.A]
c_oa=315.9 %[N.s/m]
c_ob=31.2 %[N.s/m.A]
alpha_oa=17653 %[N/m]
alpha_ob=1.553 %[N/m.A]

%Field-dependent Equations
[ko]=k_oa+k_ob*i %[N/m]
[co]=c_oa+c_ob*i %[N.s/m]
[alpha]=alpha_oa+alpha_ob*i %[N/m]

%Opening and simulating the slx files 'Simulink models'
open('Hysteresis.slx')
open('HysteresisK.slx')
```

```matlab
sim('Hysteresis.slx')
sim('HysteresisK.slx')

%Getting Tp and %PO
open('PO_Hysteresis');
open('tp_Hysteresis');


PO= PO_Hysteresis;
tp= PO_Hysteresis;

%Loop to calculate all parameters
for s = 1:1:5
    zzeta (s) =
(abs(log(PO(s)/100)))/(sqrt((pi^2)+(log(PO(s)/100))^2))
    Wn (s) = pi./(tp(s)*sqrt(1-zzeta(s)^2));
    kmre (s) = Wn(s)^2.*m;
    cc(s)=sqrt(4*kmre(s)*m)
    cmre (ss) = zzeta(ss)*cc(ss));
end

%Transmissibility curves for different currents
w= 0:1:100;

for i=1:length(kmre)
    for j=1:length(w)

        num(i,j)= ((kmre(i))^2 +(((cmre(i))^2)*(w(j)^2)));
        den(i,j)= (((cmre(i))^2)*(w(j)^2))+(((kmre(i))+((-
m)*(w(j)^2)))^2);
        T(i,j)= (sqrt((num(i,j)/den(i,j))));

    end
end

plot(w,T,'Linewidth',2)
xlabel('Frequency (rad/s)')
ylabel('Displacement Transmissiblity (X/Y)')
legend('I = 0','I = 1','I = 2','I = 3','I = 4')
title('Displacement Transmissiblity (X/Y) vs Frequency (?) for
Hysteresis model')
```

MATLAB codes for plotting stiffness and damping coefficients vs applied current

```matlab
%Applied current
i=[0 1 2 3 4];
%Stiffness and damping coefficients values of all models.
%Bingham model
kBg = [150 200 240 299 324]';
cBg = [13.52 17.945 22.37 26.795 31.22]';
%BW model
kBW = [119.54 239.08 358.62 478.16 597.7]';
cBW = [47 67 73 79 82]';
%MBW model
kMBW = [212.32 559.52 841.32 1000.3 1322.46]';
cMBW = [14.32 17.11 18.29 20.02 21.32]';
%Dahl model
kD = [346 692 1038 1384 1730]';
cD = [59.1477 84.7645 105.2315 123.1605 139.5484]';
%Hysteresis model
kH = [252.9 505.7 758.6 1011.4 1264.3]';
cH = [50.5907 72.4822 89.9756 105.3007 119.3089]';


%Plotting all models stiffness vs applied current using subplot
property
figure
plot(i,kBg)
subplot(2,3,1);plot(i,kBg); xlabel('Applied current
(A)','FontSize',12)...
    ;ylabel('Stiffness (N/m)','FontSize',12) ; title('k for Bingham
model');
subplot(2,3,2);plot(i,kBW); xlabel('Applied current
(A)','FontSize',12)...
    ;ylabel('Stiffness (N/m)','FontSize',12) ; title('k for BW
model');
subplot(2,3,3);plot(i,kMBW); xlabel('Applied current
(A)','FontSize',12)...
    ;ylabel('Stiffness (N/m)','FontSize',12) ; title('k for MBW
model');
subplot(2,3,4);plot(i,kD); xlabel('Applied current
(A)','FontSize',12);...
    ylabel('Stiffness (N/m)','FontSize',12) ; title('k for Dahl
model');
subplot(2,3,[5 6]);plot(i,kH); xlabel('Applied current
(A)','FontSize',12)...
    ;ylabel('Stiffness (N/m)','FontSize',12) ; title('k for
Hysteresis model');


%Plotting all models damping coefficient vs applied current using
subpolt property
figure
plot(i,cBg)
subplot(2,3,1);plot(i,cBg); xlabel('Applied current
(A)','FontSize',12)...
    ;ylabel('Damping coeffecient (N.m/s)','FontSize',12) ; title('c
for Bingham model');
subplot(2,3,2);plot(i,cBW); xlabel('Applied current
(A)','FontSize',12)...
    ;ylabel('Damping coeffecient (N.m/s)','FontSize',12) ; title('c
for BW model');
subplot(2,3,3);plot(i,cMBW); xlabel('Applied current
```

```matlab
(A)','FontSize',12)...
    ;ylabel('Damping coeffecient (N.m/s)','FontSize',12) ; title('c
for MBW model');
subplot(2,3,4);plot(i,cD); xlabel('Applied current
(A)','FontSize',12);...
    ylabel('Damping coeffecient (N.m/s)','FontSize',12) ; title('c
for Dahl model');
subplot(2,3,[5 6]);plot(i,cH); xlabel('Applied current
(A)','FontSize',12)...
    ;ylabel('Damping coeffecient (N.m/s)','FontSize',12) ; title('c
for Hysteresis model');
```

Appendix B: FEA Simulations

Deformation (Linear Displacement) (0 A/m – 3 A/m)
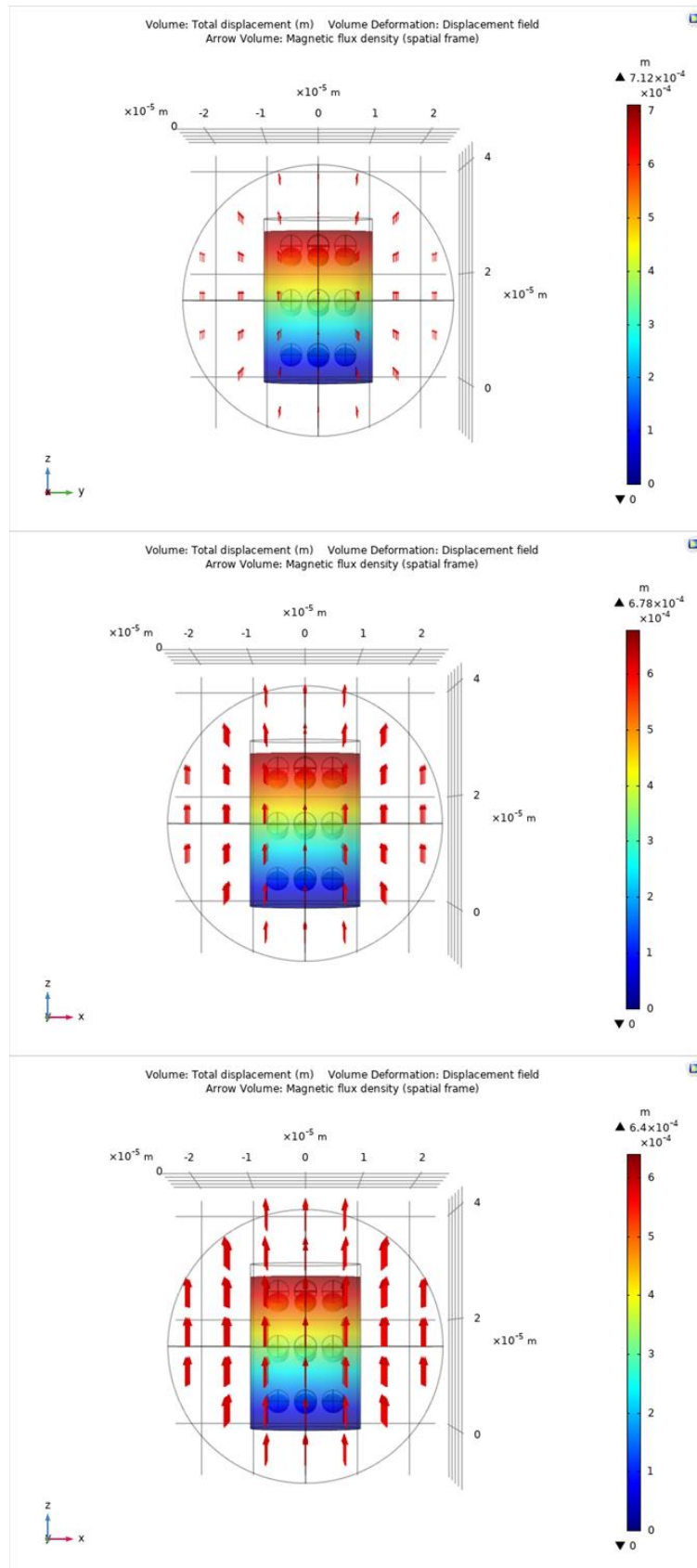
Deformation (Linear Displacement) (4 A/m – 6 A/m)
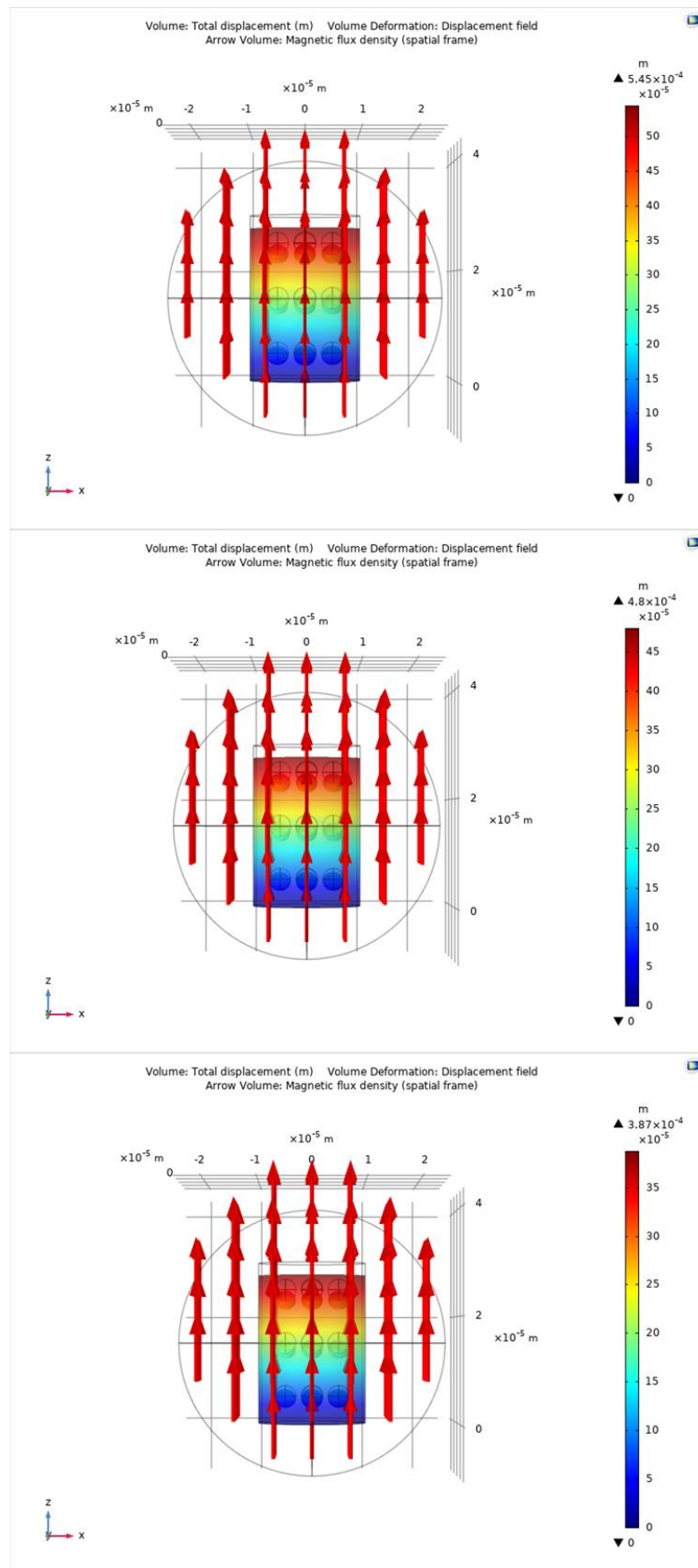
Deformation (Linear Displacement) (7 A/m)
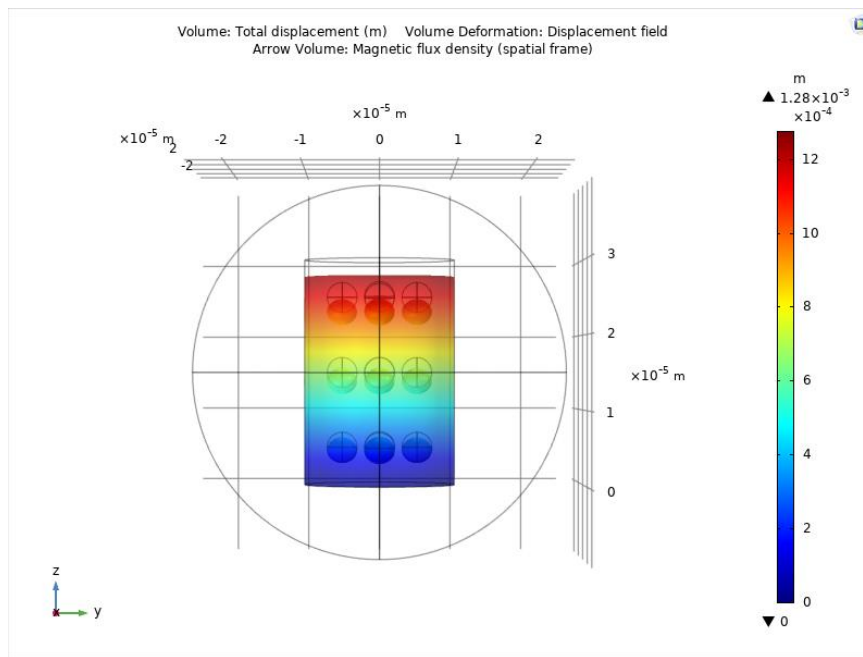
Deformation (Angular Displacement) (0 A/m – 1 A/m)
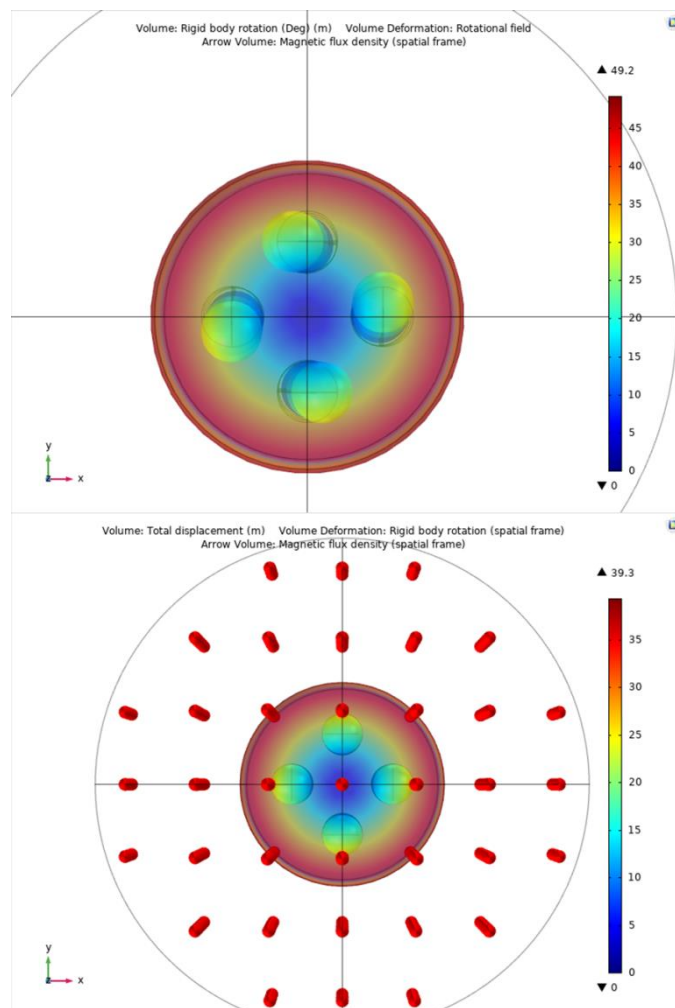
Deformation (Angular Displacement) (2 A/m – 4 A/m)
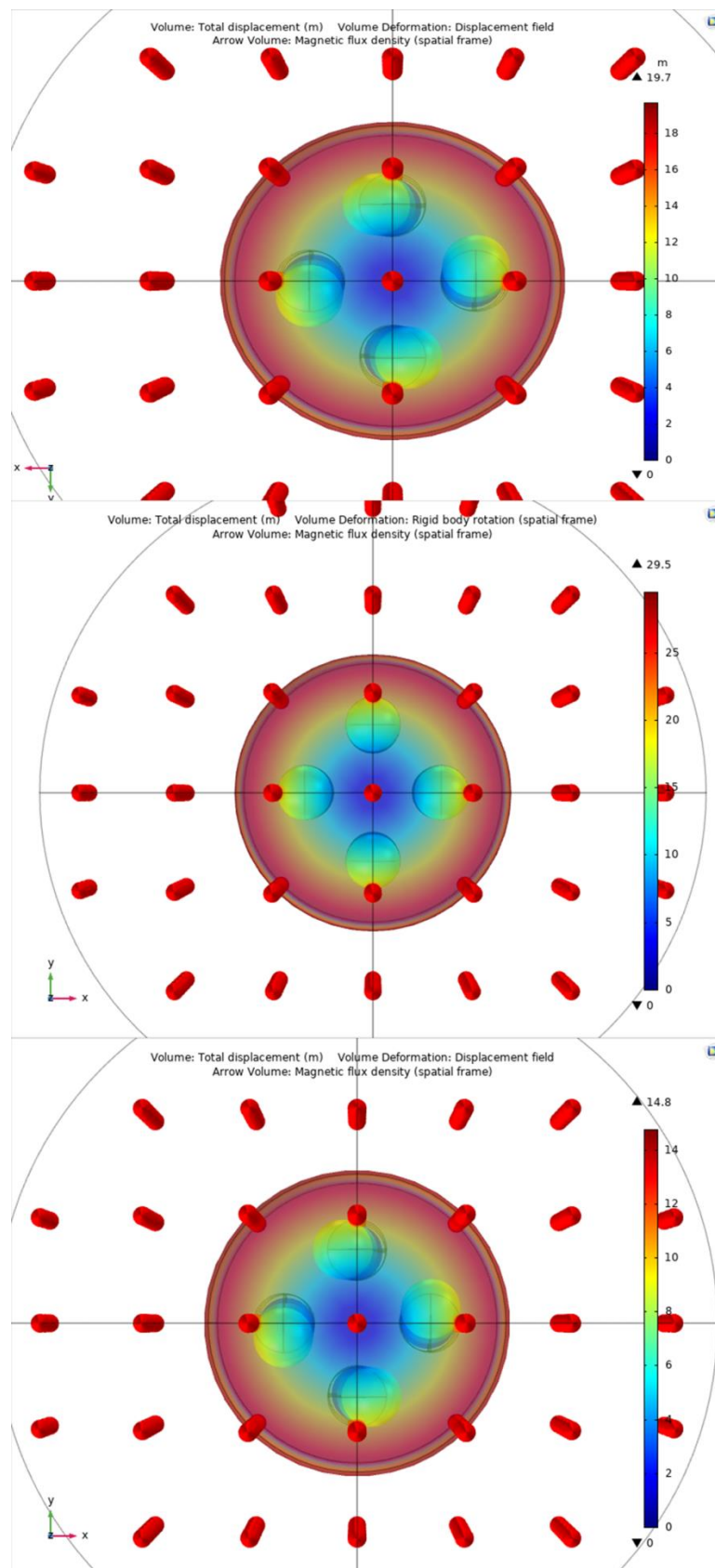
Deformation (Angular Displacement) (5 A/m – 7 A/m)
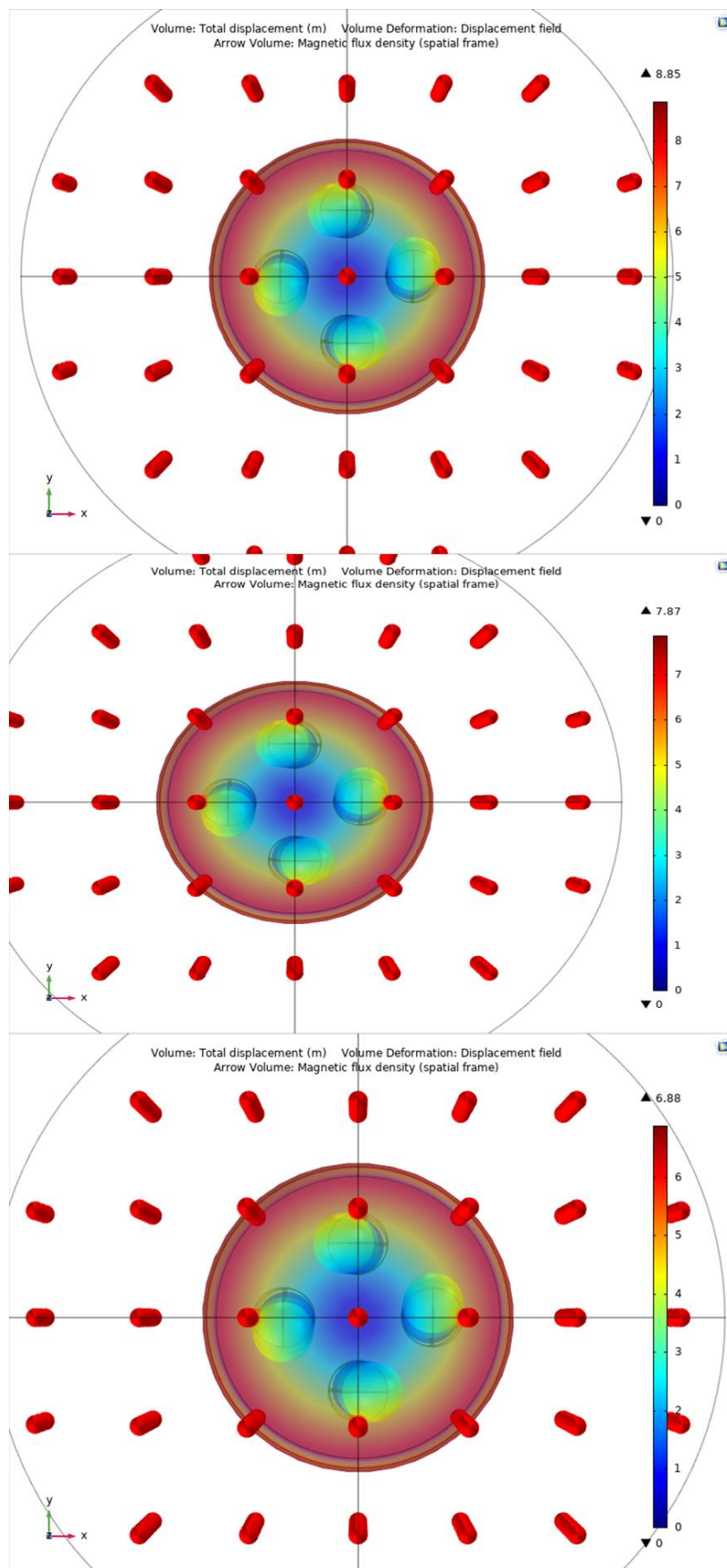
Appendix C: Experimental Developments

<u>Silicon rubber</u>

<u>Iron powder</u>

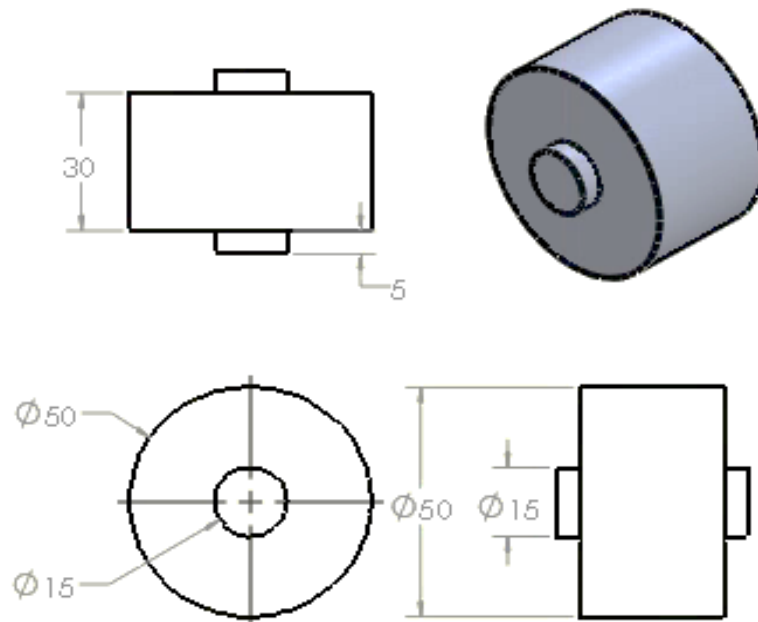Mold parts dimensions (mm)

Upper cover

Lower cover

Middle part

150
40
70
Ø5
Ø50.80
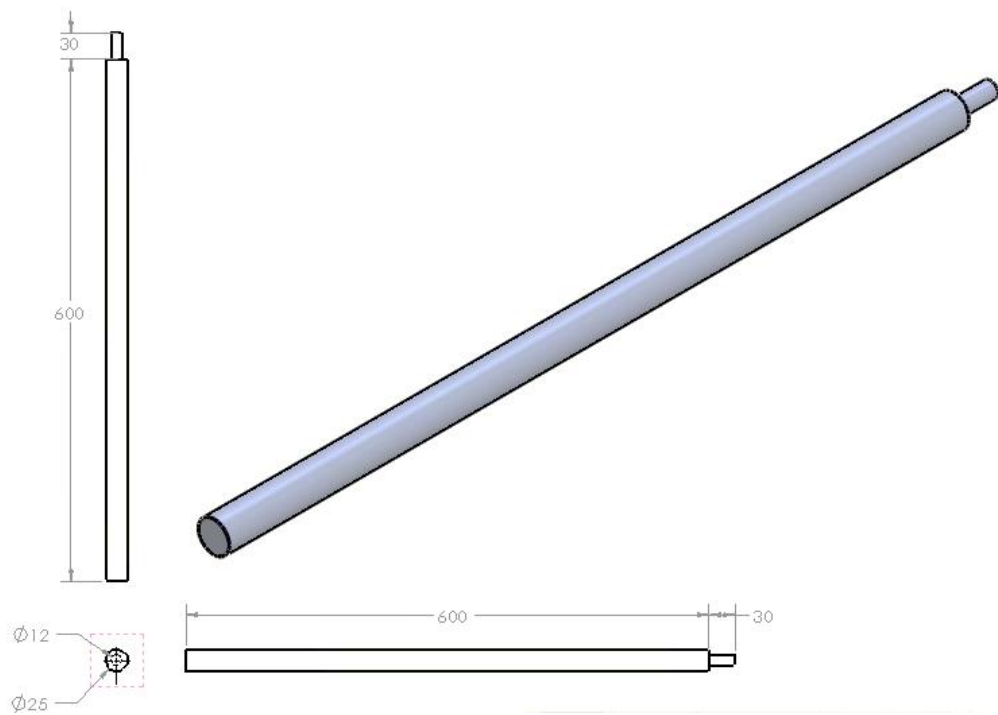Ø50.80
80
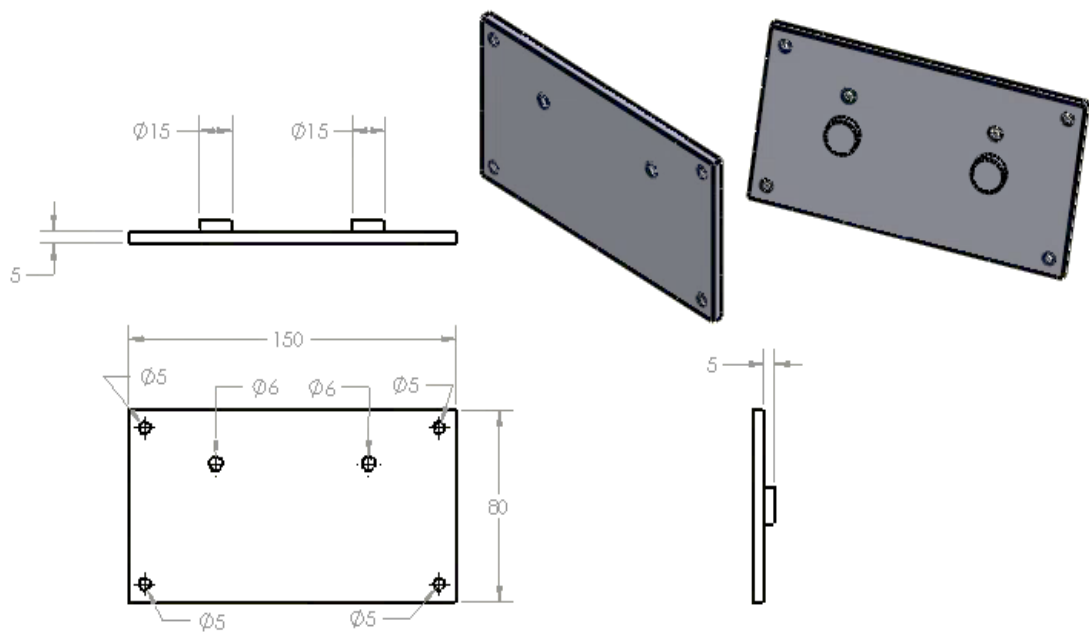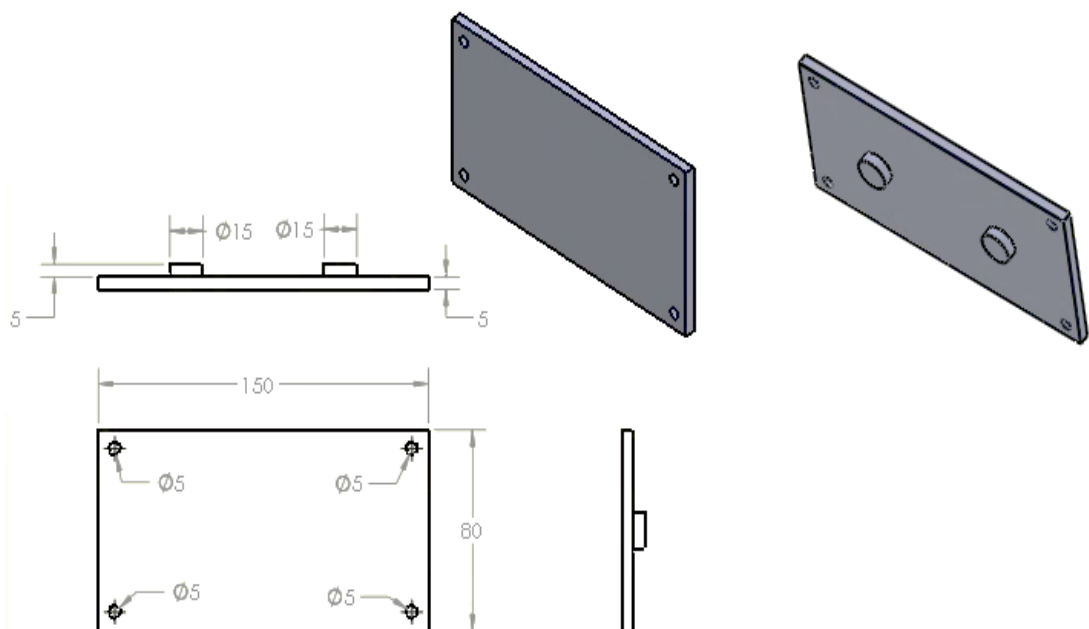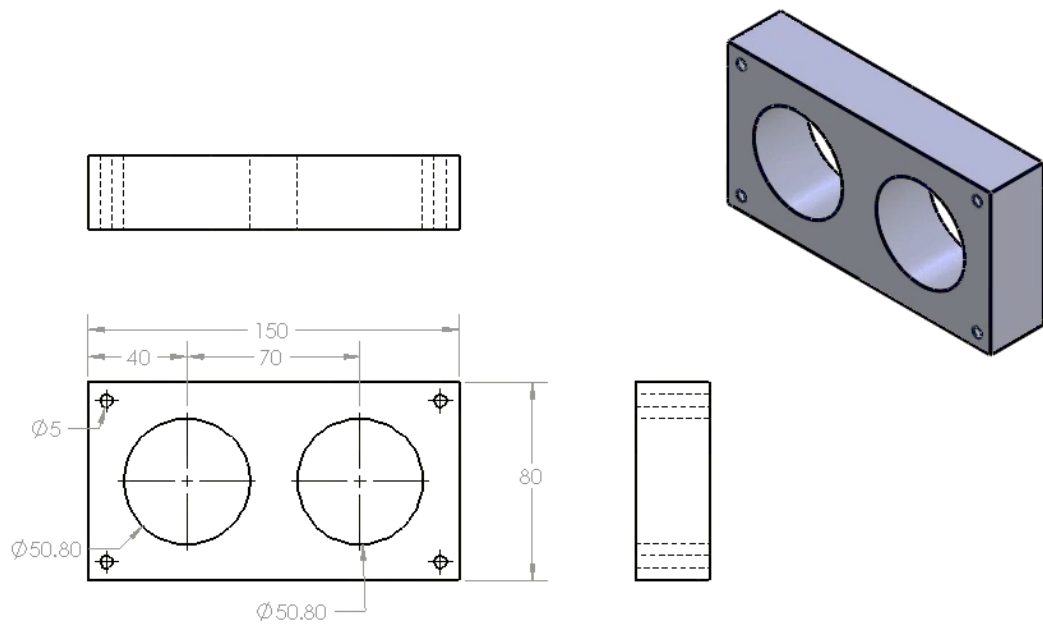
Mold
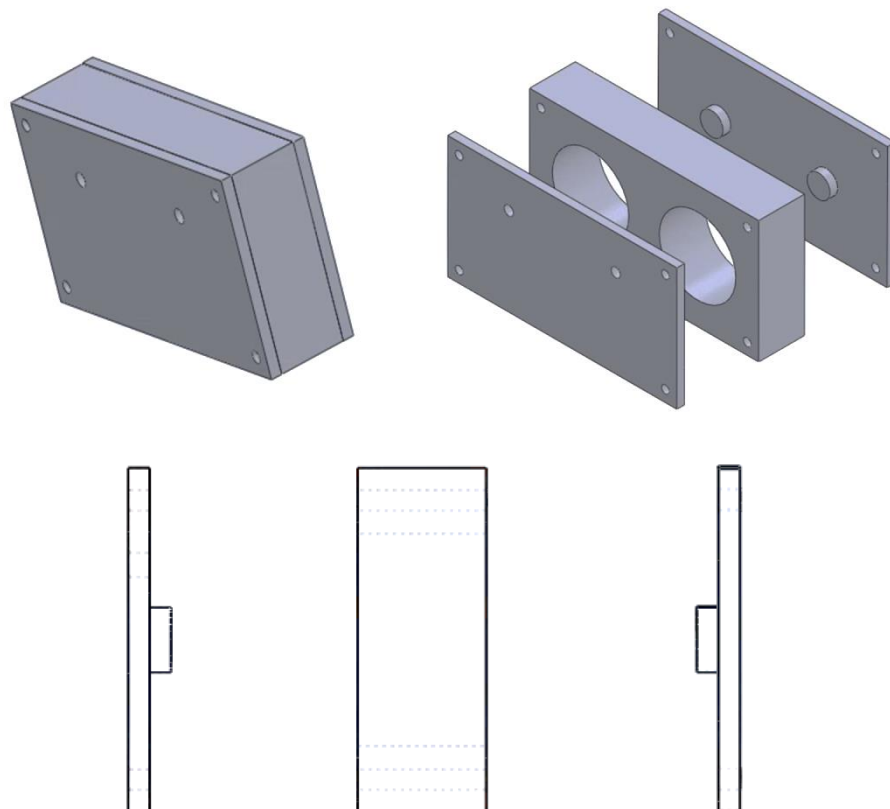
Coupling dimensions

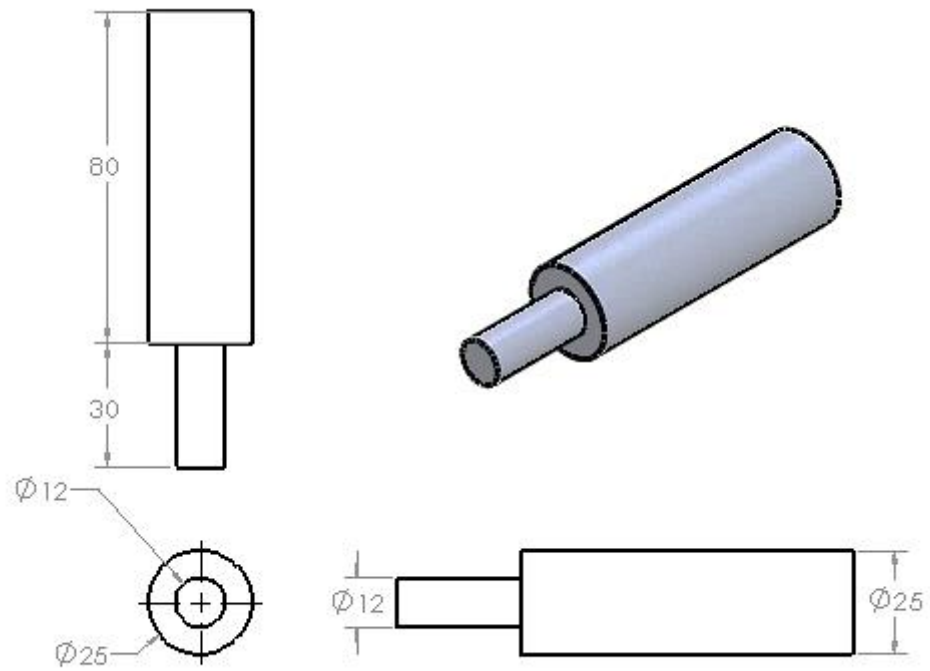*Upper and lower parts*
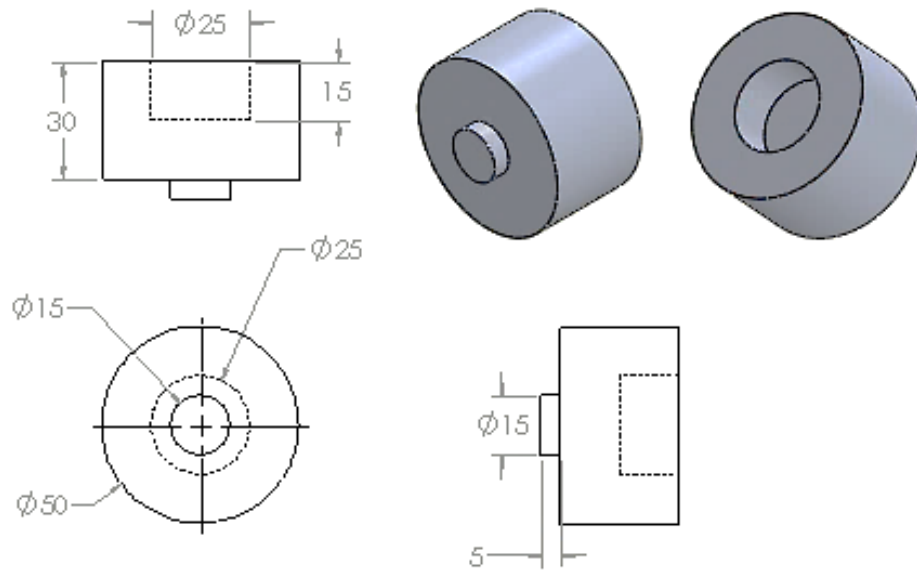
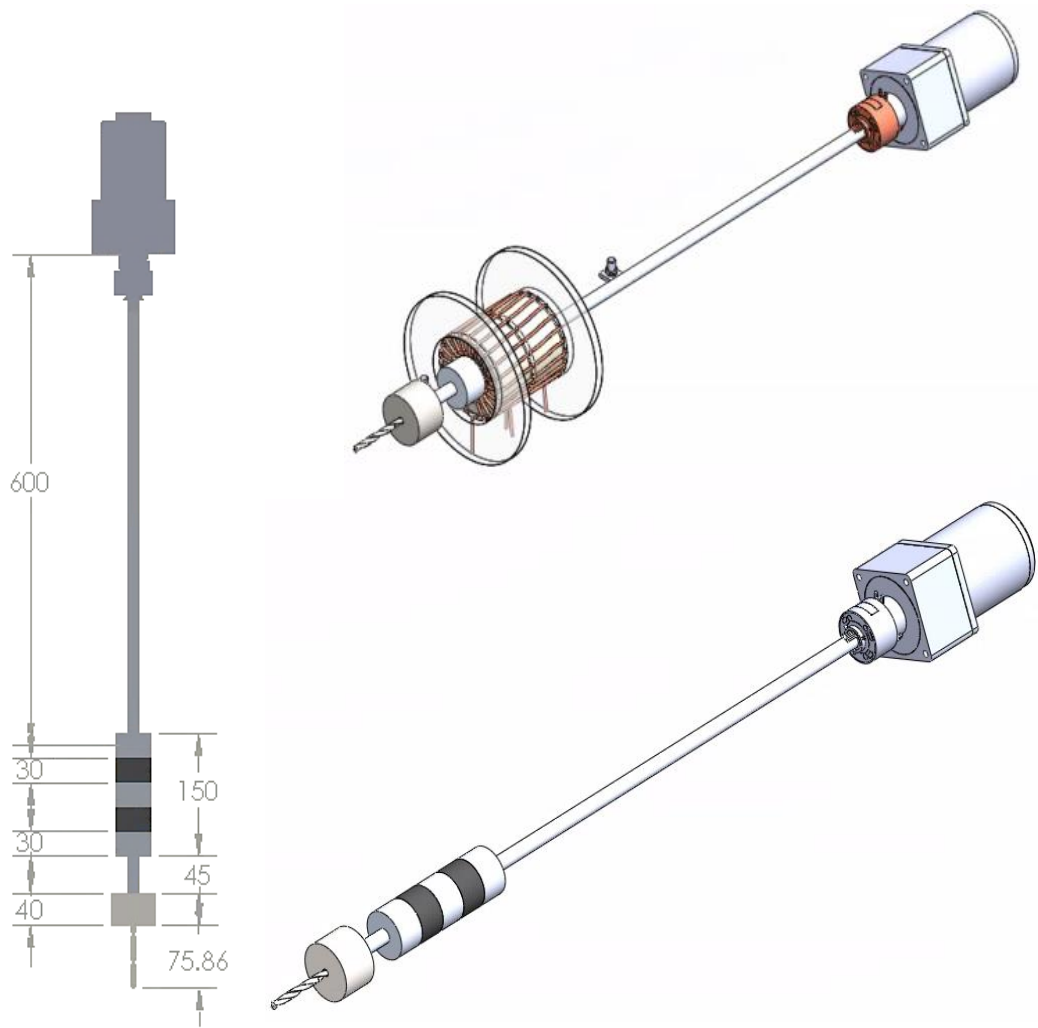*Middle part*

Coupling with MRE
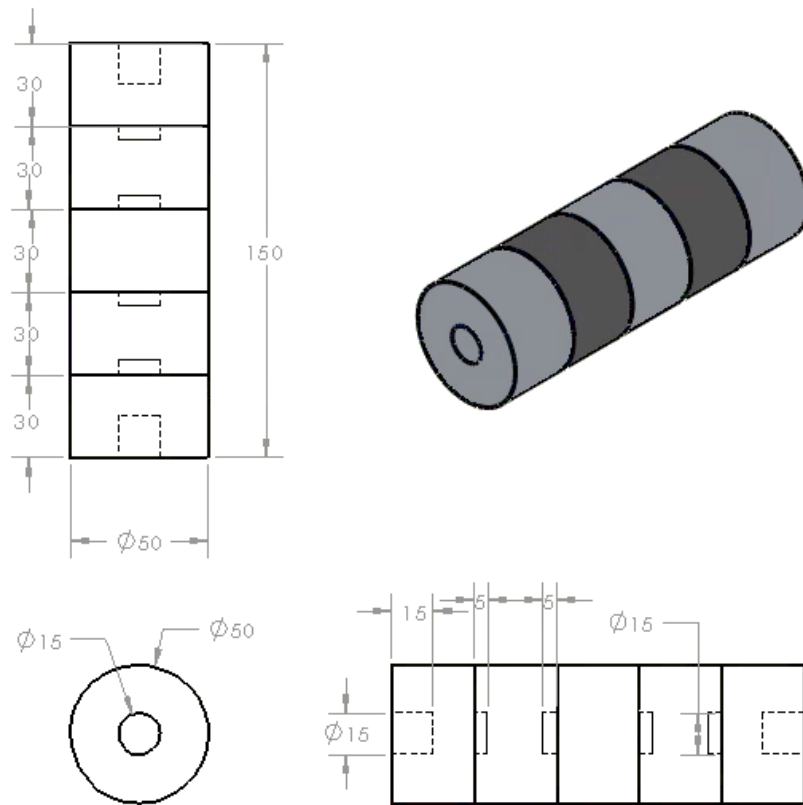
The whole system dimensions

Long shaft

Short shaft

80

30

Ø12

Ø25

Ø12

Ø25

Plates to fit the accelerometers on

25

20

25

5

5

600

30

150

30

45

40

75.86

The whole system with the electromagnetic coil

The whole system with the electromagnetic coil